A neutron scattering study of triblock copolymer micelles

Gerstenberg, Michael Christian

Publication date:
1997

Document Version
Publisher's PDF, also known as Version of record

RISØ

Risø-R-986(EN)

A Neutron Scattering Study of Triblock Copolymer Micelles

Michael C. Gerstenberg

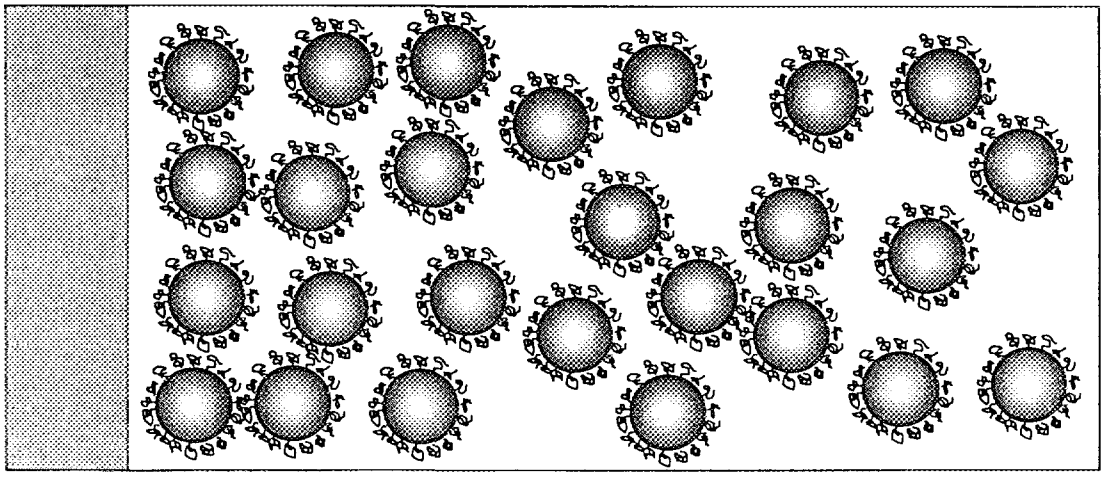

Risø National Laboratory, Roskilde, Denmark
November 1997

Risø-R-986(EN)

A Neutron Scattering Study of Triblock Copolymer Micelles

Michael C. Gerstenberg

Risø National Laboratory, Roskilde, Denmark
November 1997

Abstract The thesis describes the neutron scattering experiments performed on poly(ethylene oxide)/poly(propylene oxide)/poly(ethylene oxide) triblock copolymer micelles in aqueous solution. The studies concern the non-ionic triblock copolymer P85 which consists of two outer segments of 25 monomers of ethylene oxide attached to a central part of 40 monomers of propylene oxide. The amphiphilic character of P85 leads to formation of various structures in aqueous solution such as spherical micelles, rod-like structures, and a BCC liquid-crystal mesophase of spherical micelles.

The present investigations are centered around the micellar structures. In the first part of this thesis a model for the micelle is developed for which an analytical scattering form factor can be calculated. The micelle is modeled as a solid sphere with tethered Gaussian chains. Good agreement was found between small-angle neutron scattering experiments and the form factor of the spherical P85 micelles. Above 60°C some discrepancies were found between the model and the data which is possibly due to an elongation of the micelles.

The second part focuses on the surface-induced ordering of the various micellar aggregates in the P85 concentration-temperature phase diagram. In the spherical micellar phase, neutron reflection measurements indicated a micellar ordering at the hydrophilic surface of quartz. Extensive modeling was performed based on a hard sphere description of the micellar interaction. By convolution of the distribution of hard spheres at a hard wall, obtained from Monte Carlo simulations, and the projected scattering length density of the micelle, a numerical expression was obtained which made it possible to fit the data. The hard-sphere-hard-wall model gave an excellent agreement in the bulk micellar phase. However, for higher concentrations (25 wt % P85) close to the transition from the micellar liquid into a micellar cubic phase, a discrepancy was found between the model and the reflection data. Free-form analysis hinted towards a precrystallization of the micelles at the surface at this concentration.

For temperatures above 60°C a 5 wt % solution showed a high degree of surface association. The neutron reflection experiments indicated that the surface ordering of the triblock copolymers changed from spherical micelles to a lamellar phase with increasing temperature. Presumably, an intermediate region occurs with surface ordered rod-like micelles. It was not possible to further increase the surface ordering by applying a shear field to the solution.

In the bulk micellar cubic phase, the surface ordering could not be determined unambiguously. However, the neutron reflection data is consistent with a periodic ordering of slightly anisotropic micelles.

This report is submitted in partial fulfilment of the requirements for a Ph.D. degree at the University of Copenhagen. The work has been carried out at Risø National Laboratory, Condensed Matter Physics and Chemistry Department (formerly Department of Solid State Physics). Supervisors have been Jan Skov Pedersen from Risø National Laboratory and Stig Steenstrup from the University of Copenhagen.

ISBN 87-550-2306-1
ISSN 0106-2840

Information Service Department · Risø · 1997

Dansk Resumé Denne rapport beskriver undersøgelser af poly(ethylen oxid)/-poly(propylen oxid)/poly(ethylen oxid) triblock copolymer miceller i vandig opløsning vha. neutronspredning. Arbejdet har koncentreret sig om den ikke-ioniske triblok copolymer P85, som består af to ydre blokke bestående af 25 monomerer af ethylen oxid påsat en central del af 40 monomerer af propylen oxid. P85s amphifile natur medfører, at der dannes forskellige aggregater i vandig opløsning som en funktion af koncentration og temperatur f.eks. sfæriske og stavformede miceller samt en rumcentreret kubisk micelle struktur.

Studiet er centreret omkring micelle strukturernes opførsel i væskefasen og ved en overflade. Første del af rapporten beskriver en udarbejdet strukturel model for micellen, hvori micellen er modelleret som en fyldt kugle med påsatte Gaussiske kæder. I denne model kan en spredningsformfaktor beregnes analytisk og små-vinkel spredningsdata af sfæriske miceller af P85 i vandig opløsning er i glimrende overensstemmelse med modellen. Dog optræder en større uoverenstemmelse mellem modellen og spredningsdata for temperaturer over 60°C.

I anden del af rapporten er der lagt vægt på micellernes struktur på en hydrofil kvarts overflade. Modelfri analyse af neutron reflektivitetsmålinger viste, at micellerne ordner i en næsten periodisk lagdeling på overfladen. Inspireret heraf blev det antaget, at micellerne opfører sig som hårde kugler på en hård væg. Fra Monte Carlo simuleringer af hård-kugle systemet var det muligt at bestemme et udtryk for kuglernes tæthed på overfladen. Ved at folde denne tæthed med den projicerede tæthed af den modellerede micelle kan et udtryk opskrives som kan beskrive de fundne reflektionsmålinger. Modellen stemmer glimrende overens med reflektivitets målingerne i den sfæriske micelle fase. Overensstemmelsen ophører overraskende tæt på 25 vægt % polymer i opløsning, hvor micellerne krystalliserer i en kubisk struktur. Udfra en modelfri analyse er det plausibelt at antage, at micellerne først krystalliserer på overfladen og derefter i den dybereliggende væske.

Anisotrope miceller er ligeledes blevet undersøgt. En 5 vægt % opløsning viste en kraftig overfladeassociering over 60°C. Modelfri analyse af reflektivitetsdata indikerede, at der sandsynligvis sker en transformation fra sfæriske miceller til en lamel fase for stigende temperaturer, måske med en mellemliggende fase af anisotrope miceller. Det er ikke muligt at forøge overfladeordenen ved at påtvinge opløsningen et forskydningsfelt.

I den kubiske fase optrådte klarer Bragg-lignende reflektioner, som indikerer en meget velordnet overfladestruktur. Dog kunne strukturen ikke entydigt bestemmes, men data er konsistent med en periodisk ordning af begrænset anisotrope miceller.

The work presented is partly based on the following articles:

- *Scattering Form Factor of Block Copolymer Micelles*. J.S. Pedersen and M.C. Gerstenberg, Macromolecules, **29**, 1363-1365 (1996),.
- *Neutron Reflectometry from Solid-Solid and Solid-Liquid Interfaces at the TAS8 Spectrometer at Risø*, M.C. Gerstenberg, J.S. Pedersen, K.N. Clausen, Neutron News, **7**, 25-31 (1996).
- *The Surface Induced Ordering of Block Copolymer Micelles at the Solid-Liquid Interface*, M.C. Gerstenberg, J.S. Pedersen, G.S. Smith, submitted for publication.
- *The Surface Induced Ordering of Block Copolymer Micelles at a Solid-Liquid Interface: Experimental Results*, M.C. Gerstenberg, J.S. Pedersen, G.S. Smith, in preparation.
- *The Surface Induced Ordering of Block Copolymer Micelles at a Solid-Liquid Interface: Modeling Aspects*, M.C. Gerstenberg, J.S. Pedersen, G.S. Smith, in preparation.

Furthermore, the work in the following articles have not been included in this work:

- *Neutron Reflection Studies of Poly(Phenol) Films*, S.J. Roser, D.J. Caruana, M.C. Gerstenberg, J. Electroanal. Chem., **411**, 153-160 (1996).
- *Structure of Phospholipid Monolayers Containing Poly(Ethylene Glycol) Lipids at the Air-Water Interface*, J. Majewski, T.L. Kuhl, M.C. Gerstenberg, J.N. Israelachvili, G.S. Smith, J. Phys. Chem. B, **101**, 3122-3129 (1997).
- *Temperature and Time Dependent Investigations of Cd- and Uranyl-Stearates Multilayers by Means of Neutron Reflectivity Measurements*, A. Bolm, U. Englisch, F. Penacorada, M.C. Gerstenberg, U. Pietsch, accepted for publication in Supramolecular Science.
- *Time Dependent Neutron Reflection Studies of Silicon/Poly(Phenol) films*, S.J. Roser, D.J. Caruana, M.C. Gerstenberg, in preparation.
- *X-ray Synchrotron Studies of Polymer-Modified Lipid Monolayers on Water*, J. Majewski, T.L. Kuhl, K. Kjær, M.C. Gerstenberg, J. Als-Nielsen, J.N. Israelachvili, G.S. Smith, in preparation.

Contents

1 Introduction

Block Copolymers

Block copolymers are composed of sequences (i.e. blocks) of chemically distinct repeat units. Usually, the block copolymer is comprised of only two repeat units, A and B, in an $A-B$ diblock copolymer or an $A-B-A$ triblock copolymer conformation. Among the many materials utilized for repeat units are poly(styrene) (PS), poly(isoprene) (PI), poly(ethylene) (PE), poly(ethylene propylene) (PEP), and poly(ethylene butylene) (PEB). The ability to control the molecular architecture by altering the block sizes and composition gives an unprecedented possibility to investigate the phase behaviour and novel physical properties of these morphologically diverse materials.

Amphiphilic Block Copolymers

When block copolymers are dissolved in a selective solvent, i.e. where one of the blocks is insoluble due to unfavourable interactions with the solvent, they can self-associate into a large diversity of structures such as spherical or rod-like micelles, bulk micellar crystals, or lamellae (see Figure 1). In aqueous solution the amphiphilic block copolymers, containing both a hydrophilic (solvent-attracting) and hydrophobic (solvent-repelling) part, typically self-associate and also assemble at interfaces in an attempt to sequester their non-polar regions from contact with the aqueous phase. This ability is analogous to the self-assembly of surfactants (surface-active agents) e.g. at the oil-water interface in microemulsions. Surfactants are typically comprised of a hydrophilic head group and a hydrophobic tail group of hydrocarbon segments. In fact, the amphiphilic block copolymers are considered to be macromolecular non-ionic counterparts of the ordinary surfactants such as soaps and lipids.

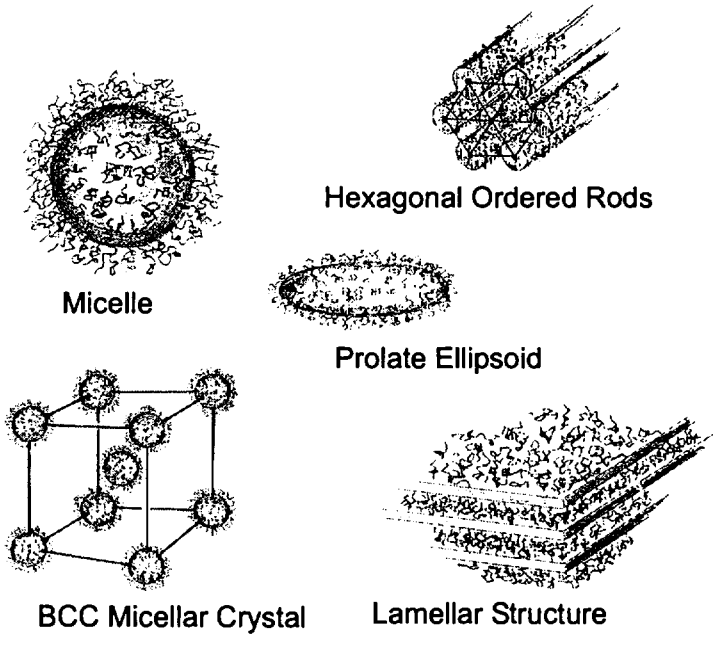

Figure 1. The different phase structures arising from self-association of triblock copolymers.

Pluronics

Examples of amphiphilic block copolymers are the *Pluronics*, which are comprised of sequences of ethylene oxide (EO) and propylene oxide (PO). They have been extensively studied due to their novel physical properties and commercial utility in e.g. steric stabilization, emulsification, lubrication, pharmaceuticals, drug solubilization and delivery, and bioprocessing (see e.g. ref.'s [4, 67, 70] and ref.'s

therein). Consensus has been reached on the structural and thermodynamic properties and several extensive reviews have been published recently [6, 4, 23, 89].

An overview of the family of triblock copolymers $EO_mPO_nEO_m$ is depicted in Figure 2. These block copolymers, the Pluronics, have a common name convention consisting of first a letter for the pristine appearance, either P (paste), F (flake), or L (liquid), secondly a number related to the total molecular weight in the series of equal weight fractions of poly(ethylene oxide) (PEO), and thirdly the weight fraction of poly(ethylene oxide) in tens of percent. Hence, F127 and P85 appear as flakes and paste, have a molar mass of 4000 and 2250, and contain 70 and 50 % ethylene oxide, respectively.

$EO_mPO_nEO_m$

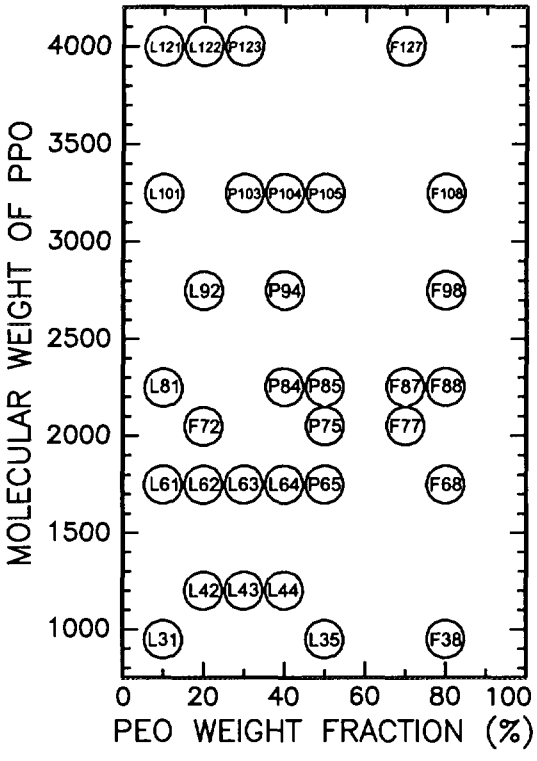

Figure 2. The name convention for the Pluronics, $EO_nPO_mEO_n$.

Dissolved amphiphilic triblock copolymers are an ideal model system in two aspects: The self-associated aggregates can be viewed as a dense core with polymers attached to the surface and thus enables one to look at the polymer conformation at a curved interface. Furthermore, the ordering of the aggregates themselves is a field of current interest and related to e.g. surface-induced ordering of liquid crystals. Both these issues will be addressed in the work of this thesis.

Purpose of the Investigations

The main purpose of the present study is to investigate the surface-induced structures of a single representative member of the Pluronic family, P85, in aqueous solution at the hydrophilic surface of single-crystalline quartz. The bulk structures have already been well understood as a function of temperature and concentration [44, 94]. As we shall see below P85 is ideal for this study because of the richness of structures that appears and thus enables us to look at the influence e.g. hydrophobicity and geometrical constraints have on the surface induced ordering on the structures of the triblock copolymer. The investigations will focus on the higher concentrations (c>5 wt % P85), where the aggregation behaviour is predominant. Consequently, the work is an extension of the previous studies [74, 79, 135] which have been centered around low concentration solutions and

monolayer adsorption. In the following paragraphs the obtained results from bulk analysis and adsorption investigations will be briefly reviewed.

1.1 P85

The non-ionic triblock copolymer P85 consists of two outer segments of 25 monomers of ethylene oxide (EO) attached to the central part of 40 monomers of propylene oxide (PO). The chemical formula can be written as

Chemical Formula

$$H[OCH_2CH_2]_{25} - [OCH_2CH(CH_3)]_{40} - [OCH_2CH_2]_{25}H, \quad (1)$$

or in short form as $EO_{25}PO_{40}EO_{25}$. Propylene oxide is hydrophobic for temperatures above approximately 15°C, whereas ethylene oxide remains hydrophilic at least up to 70°C. The amphiphilic character leads to formation of various aggregates in aqueous solution such as a spherical and rod-like micelles and a BCC micellar crystal mesophase (see Figure 1).

Phase Diagram

Bulk Structures

The bulk structures in aqueous solution have been determined as a function of temperature, concentration, and pressure with a variety of complementary techniques (small angle neutron and x-ray scattering, dynamic and static light scattering, ultrasonic speed measurements, differential scanning calorimetry, rheology, low-shear viscosity, and light transmission measurements [21, 44, 94]). The temperature versus polymer concentration phase diagram [89] is depicted in Figure 3. In the following the different phases will be discussed.

The temperature Versus Polymer Concentration

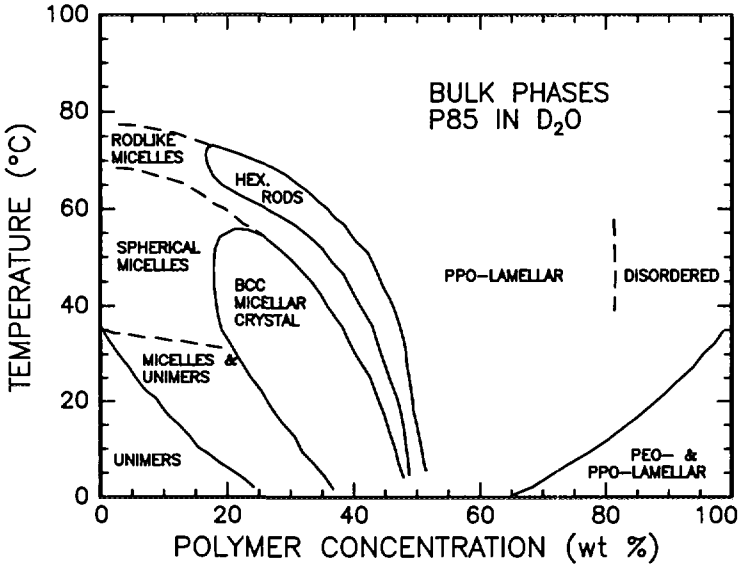

Figure 3. The temperature versus concentration phase diagram. Adapted from Mortensen [89].

Unimers. For low temperatures and concentrations the triblock copolymer is totally dissolved. The radius of gyration R_g was determined by small-angle neutron scattering (SANS) measurements [94] to 17 Å. This value is slightly less than would

be expected from a Gaussian chain statistic[1] $R_g^2 = bL/6$, where L is the contour length and b the statistical segment length (Kuhn length), suggesting that the less soluble poly(propylene oxide) (PPO) is more compact than would be expected from a Gaussian chain [89].

Compact Unimers

Unimer and Micelle Coexistence region. As the temperature is increased above the critical micelle temperature (CMT) or the concentration above the critical micelle concentration (CMC), the unimers start to aggregate into micelles. The transition is generally very broad and the reported values are dependent on which technique has been used. A large compilation of CMT and CMC for Pluronic triblock copolymers using the dye stabilization method has been reported by *Alexandridis et al.* [5].

CMT and CMC

The aggregation is mainly driven by entropy and can be explained by *the hydrophobic effect* introduced by *Tanford* [132]. When only unimers of the copolymer are present the water molecules form a solvent cage around the hydrocarbon chains of the unimer. Although the micelle formation is enthalpic, and entropic unfavourable due to the localization of the PO in the micellar core, the increase in entropy caused by the restoring of the hydrogen bonding structure in water makes it favourable for the copolymer to aggregate. These considerations are supported by the measurements of *Alexandridis et al.* [4], who determined the standard Gibb's free energy $\Delta G°$, enthalpy $\Delta H°$ and entropy $\Delta S°$ of micellization[2] from a dye stabilization method to -25.5 kJ mol^{-1}, 229 kJ mol^{-1}, and 0.842 kJ $mol^{-1}K^{-1}$, respectively, in 1 % (w/v) aqueous solution at the critical micelle temperature (CMT). The negative free energy signifies the spontaneous formation of the micelles from unimers.

The Hydrophobic Effect

Mortensen & Pedersen [94] modeled the micelles as monodisperse spheres with hard-sphere interaction. For this model it is possible to obtain an analytical expression for the structure factor in the Percus-Yevick approximation. By fitting SANS data of P85 the micellar volume fraction, η, was found to increase linearly with temperature at a given concentration in this region. At the border of the spherical micellar region, the unimers were found to be associated in spherical micelles with a concentration of free unimers equal to CMC.

Hard-Sphere Model

Spherical Micelles. The block copolymer P85 forms micelles in solution in the region between 0 and 25 wt % and 30 and 70°C. The micellar structure is not static, however. As field gradient NMR measurements of P85 below 10 wt % have shown, each copolymer has a lifetime in the micelle between 1 μs and 1 ms [36]. At temperatures close to ambient EO has 2-5 water molecules associated with each monomer, but as the temperature is risen more entropy is introduced into the system and less water molecules are associated with each monomer. Thus, the solubility of EO is reduced with increasing temperature, the repulsion among the PEO chains is reduced and the chains contract resulting in an increase in the aggregation number of the micelles. From the earlier mentioned SANS studies of P85 by *Mortensen & Pedersen* [94] it has been shown that the size of the spherical micelle is solely dependent on temperature and not concentration. Furthermore, the radius of the core, R, is found to obey [91]

Copolymer Lifetime in a Micelle

Size of the Micelle

$$R \propto (T - T_{cm1})^{0.2}, \tag{2}$$

[1]The Gaussian model of the polymer chains assumes "random walks" and thus the distance r_{ij} between two points on the chain follows a Gaussian distribution for all its intersegmental distances given by $p(r_{ij}) = (3/(2\pi < r_{ij}^2 >))^{3/2} 4\pi r_{ij}^2 \exp(-3r_{ij}^2/(2 < r_{ij}^2 >))$, where $< r_{ij}^2 >$ is the mean square intersegmental distance. For a contour length between i and j, L_{ij} tending to infinity, $< r_{ij}^2 >= bL_{ij}$. b is called the statistical segment length (Kuhn length) and reflects the short range interactions between adjacent polymer segments along the chain [43].

[2]Standard energy, entropy, or enthalpy is defined as the change for transfer of 1 mol of amphiphile in solution to the micellar phase

where R is the core radius of the micelle and T_{cm1} is the critical micellization temperature.

The volume fraction, η, is found to increase with concentration at constant temperature, until a critical volume fraction $\eta_c = 0.53$ is reached close to 25 wt %, where the micellar liquid crystallizes [92].

Prolate Ellipsoids and Rod-like Structures. Drastic changes occur in the bulk phase when a low concentration ($c < 15$ wt %) aqueous solution of P85 is heated above approximately 70 °C. In the structure analysis based on SANS measurements by *Mortensen & Pedersen* [94], the scattering function was observed to change drastically above approximately 70 °C in the low-concentration regime; the characteristic correlation peak, seen for the spherical micelles, totally disappeared. The pair-correlation function was found to be reminiscent of prolate ellipsoids with an increasing major axis with increasing temperature. It was observed that an increase in temperature or concentration caused a more elongated structure of the aggregates. *Mortensen & Pedersen* [94] suggested a transformation from spherical to rod-like micelles with an intermediate prolate ellipsoidal structure. At 70°C the radius of the core approaches 50 Å giving 2.5 Å per monomer of PPO for the chains crossing the center of the micelle. These PPO chains are thus highly stretched, a very entropically costly configuration. Another possibility is that EO and PO are mixed in the center of the micelle as indicated by lattice model calculations of *Noolandi et al.* [100].

SANS Measurements

In the more dilute region, aqueous solutions of P85 have been shown to transform into a soft gel at higher temperatures strengthening the sphere-to-rod transition hypothesis. Capillary viscosity measurements [122] ($c < 1$ wt %) showed a large increase in the viscosity as the temperature exceeded 70°C. The effect became more pronounced with increasing concentration. These findings were in agreement with low-shear viscosity measurements [44], which showed a similar temperature dependence of the viscosity up to about 15 wt %.

Soft Gel

Linse et al. [74] has provided a unification of the lattice theory for polymer solutions in heterogeneous systems by Scheutjens and Fleer and the polymer model initially proposed by *Karlström* [60]. In the latter model EO has a nonpolar conformation with low energy, a low statistical weight and a less polar conformation with higher energy and higher statistical weight. These conformations are consistent with ^{13}C-NMR chemical shift measurements. At low temperatures the former conformation is more populated, and since water prefers a polar solute, the effective polymer-solvent interaction is favourable, whereas a higher temperature the latter conformation is more populated making the polymer-solvent interaction less favourable. Hence, EO becomes less hydrophilic with temperature. The mean field lattice model is able to reproduce the occurring phases in the temperature-concentration phase diagram, although not quantitatively, but supports the transformation of the spherical micelles into the elongated shape of prolate ellipsoids.

Theoretical Model Calculations

BCC Cubic Crystal. For concentrations larger than 25 wt % , the micelles undergo a first-order transition and form a highly viscous BCC liquid-crystalline phase when the micellar volume fraction saturates at the value of $\eta_c = 0.53$, *a thermoreversible gelation.* In a limited range between $\eta = 0.47$ and η_c=0.53 the liquid and crystalline domains coexist and the viscosity increases dramatically in this range.

Hard-Sphere Crystallization

Shear Behaviour

Traditionally, shear cells in Couette geometry have been used to measure the response of solutions to shear. The Couette shear cell consists of two concentric

cylinders, where the solution is contained in the narrow gap between the cylinders. The shear is applied to the solution by rotation of the outer cylinder, typically [90]. At low concentrations above approximately 70°C (rod-like micelles), shear applied in a Couette cell gave only a small effect for 1 wt %, whereas a transition to a nematic phase was observed for 10 wt % at 76°C [89]. In the cubic phase, where the triblock copolymer forms a highly viscous solution, the polycrystalline material can be transformed into a single crystal by application of shear. From SANS measurements of 25 wt % P85 shear-oriented in a Couette geometry shear cell, *Mortensen* [88] identified a perfectly ordered BCC micellar liquid crystal with a lattice constant of 170 Å. True long-range order in the "bond-angle" correlation length was found, but almost liquid-like order in the "bond-length" correlation on the order of 400 Å, i.e. 2-3 lattice periods.

Nematic Phase

Micellar Single Crystal

Dependencies on Block size and EO/PO Fraction

Mortensen & Brown [95] found that P85, F87, and F88, i.e. increasing the PEO content of the polymer, gave similar temperature and concentration dependencies. However, the larger the degree of polymerization of PEO, the smaller the core was observed and thereby the micellar aggregation number. In the study of *Alexandridis et al.* [5] of a large number of the Pluronics, it was found0 that the copolymer became less hydrophobic as a whole when the PEO content was increased or the molecular weight was low. Hence, aggregation occurred at higher temperatures. Conversely, the copolymers with a large hydrophobic domain of PPO formed micelles at lower temperatures, and CMC and CMT were found to decrease accordingly. Only a slight increase in CMC and CMT were found with increasing number of EO segments. Consequently, the aggregation is mainly determined by the PO content in the triblock copolymer.

1.2 Surface-Induced Ordering of P85 in Solution

The work of this thesis will be centered around the surface-induced morphologies of the different micellar structures occurring in the P85 temperature-concentration phase diagram.

Related Ordering in Microemulsions

The presence of a surface has previously been shown to have a subtle effect on the ordering of microemulsions. Under appropriate conditions the microemulsion consisting of AOT (sodium-di-2-ethylsulfosuccinate), water, and oil forms inverse micelles in which a water core is coated by a shell of AOT with tails sticking out into the oil. From a X-ray reflectivity study, *Schwartz et al.* [123] proposed a two-layer micellar or droplet model describing only the closest vicinity to the surface. The micelles were found to be aligned by the air-microemulsion surface in a close-packed array in the first layer with a subsequent less dense second layer. However, the simple droplet model neglected positional disorder occurring with increasing distance from the surface and size polydispersity of the droplets. Another example is the study of the surface-induced ordering of bicontinuous microemulsions which consist of mixtures of the nonionic surfactant $C_{10}E_4$ (polyethylene glycol monoalkyl ethers), water (D_2O), and oil (octane). The presence of the air-microemulsion surface was found to induce an alternate layering of water and oil penetrating deep into the bulk [141]. The latter study was extended to include the structure of the microemulsion near the hydrophobic silicon-microemulsion interface [68]. Ginzburg-Landau (G-L) theory, where the local concentration between oil and water is the order parameter, was used to analyse the reflectivity measurements. A damped oscillatory one-dimensional order parameter profile, derived from the G-L Hamiltonian, was found to reproduce the neutron reflectivity from the microemulsion at the hydrophobic silicon surface. This approach offers

two parameters to be determined: The surface correlation length and the domain size.

As we shall see, the decaying oscillatory form of the scattering length density obtained from neutron reflectivity measurements also emerges for the ordering of P85 micelles at a solid-liquid interface. Although the G-L theory offers insight into the surface ordering it is still a phenomenological approach. In order to analyse the P85 data a detailed modeling has been performed incorporating both computer simulations and detailed modeling of the structure of the micelle. This way more direct parameters relating to the structure of the micelles can be obtained.

A prerequisite for understanding the ordering of P85 micelles at a surface is insight in the behaviour of the various constituents of the system. Therefore, the next sections will be devoted to a brief introduction of the experimental methods, the investigated surface, and the adsorption of EO and PO single polymer chains on the surface.

Block Copolymers at Surfaces

Polymers adsorbed at interfaces have received a large interest not the least in view of the technological interest. The block copolymers have shown a remarkable ability to adsorb to interfaces in solution and are widely used as an efficient agent for steric stabilization [55]. Previously, low concentrations of block copolymers in solutions have been investigated where important parameters have been the layer thickness and the surface excess concentration as well as the adsorption and desorption kinetics. The influence of micelles on block copolymer surface adsorption and desorption kinetics [96, 97] has been investigated, but only little attention has been given to the structure of aggregates on a solid surface.

Experimental Methods

"Buried Interfaces"

Several experimental techniques [35, 128] are available for the investigations of "buried interfaces" such as the interface between polymeric materials and the solid-liquid interface. Usually, complementary techniques have to be combined in order to determine the surface structure unambiguously. Among the non-destructive techniques are the already mentioned X-ray and neutron reflectivity, ellipsometry, surface plasmons, photon correlation spectroscopy, surface forces apparatus measurements, and small-angle neutron and X-ray scattering. Although each technique is sensitive to a particular facet of the surface ordering (adsorption) only small-angle scattering and reflectometry can yield direct information about the polymer volume fraction profile at the surface.

Reflectometry

For investigations of the solid-liquid interface neutron reflectometry is ideally suited since it provides the possibility of passing trough large thicknesses of material with only slight attenuation and has subnanometer resolution. Thus, neutrons can reflect from the solid-liquid interface after having traversed the solid. In aqueous solution, the contrast between the solute and the solvent can be conveniently chosen for neutrons by deuteration of parts of the solute or by using mixtures of H_2O and D_2O. With X-ray reflectivity high energy radiation (>20 keV) is required to reach the solid-liquid interface. Usually, the liquid has to be covered by a thin foil, which makes interpretation of the data difficult. Furthermore, radiation damage to the polymer system may occur with the high energy X-rays. Several studies have been performed with X-ray reflectometry of surface ordering at the air-liquid interface [7, 10].

Small-Angle Scattering

In small-angle scattering any deviation from the scattering obtained from a two-phase system with sharp boundaries can be attributed to the polymer conformation at the interfacial region.

Ellipsometry

Ellipsometry provides an ideal tool for adsorption and desorption kinetics and gives information on the index of refraction and film thickness. However, the technique is model-dependent and the parameters are not unique. Often only one quantity, e.g. the total absorbed amount of polymer material, is accessible. The technique has its strength in the study of polymer adsorption dynamics.

Photon Correlation Spectroscopy

Photon Correlation Spectroscopy typically provides indirectly the hydrodynamic thickness of an adsorbed layer at spherical nanometer sized particles. This technique suffers from the drawback that the thickness is derived as the difference between the size of the particles with and without polymers adsorbed.

Direct Imaging

Direct imaging techniques such as atomic force microscopy could remove the unambiguity often arising in the structure determination, but the technique is still in its infancy in investigation of surfactant aggregates at solid surfaces in aqueous solution [80].

In this thesis neutron reflectometry is selected for the investigations of the micellar surface induced ordering due to the unique possibility for accessing the solid-liquid interface. Since neutrons are the main probe for these investigations of the solid-liquid interface, single crystal quartz is chosen as substrate. Quartz has a low absorption of neutrons, is transparent in crystalline form, and is available in crystals of centimeter large dimensions. In effect, these properties make it possible to pass a beam of neutrons through a large crystal and study the solid-liquid interface directly.

Silica

Forms of Silica

Silica is the common designation for SiO_2 in all its different forms (crystalline (quartz), amorphous, hydrated and hydroxylated). The soluble form of silica is called monosilicic acid generally formulated as $Si(OH)_4$. The structure of monosilicic acid is assumed to involve silicon coordinated with four oxygen atoms as in crystalline quartz [57]. There is no evidence that silica is "soluble" to any appreciable degree in any liquid other than water.

Structure

Ordinary quartz, SiO_2, has at 25°C three molecules in a hexagonal unit cell with dimensions $a_0 = 4.91304$ Å, and $c_0 = 5.40463$ Å [140], which gives a neutron scattering length density of $\rho^N_{quartz} = 4.17 \times 10^{-6}$Å^{-2}.

Water Adsorbed on Silica

When exposed to water, the hydrophobic siloxane (Si-O-Si) surface of clean SiO_2 reacts with water and thus becomes covered with the hydrophilic *silanol*, which is the common term for an OH group attached to silicon. All silicas dried from water at less than 150°C develops a fully hydroxylated surface in which the surface structure terminates in *silanol* (SiOH) groups. The surface is completely hydrophilic and readily wettable by water and by water-soluble organic molecules [57]. It is the silanol groups at which the water molecules are adsorbed and at which many organic molecules with polar groups hydrogen bind, linking them to the surface. Also charged silicic acid ($Si\text{-}O^-$) has been found to form on the surface [57] in the presence of water.

Silanol

Surface Structures an Issue of Discussion

Even though the surface structure and surface chemistry of silica have received large attention, see e.g. *Iler* [56, 57] or *Helms et al.* [53], the surface properties are still an issue of discussion [24, 137]. For example, *Cosgrove et al.* [24] found from reflectivity measurements that a 17 Å thick water layer was present at the surface of a cleaned quartz single crystal in air. The layer could be removed by heating the sample to about 150°C under vacuum. With water present, the layer was seen to reappear. The origin of the layer was suggested to be water penetrating into the quartz surface. Furthermore, *Vigil et al.* [137] have recently proposed a model for the behaviour of hydrophobic and hydrophilic silica. Instead of the previously accepted layering of water on hydrophilic silica, a protrusion of silicic acid $Si(OH)_4$ forms a silica gel layer typically 20 Å thick. Water is thus simply acting as a good

solvent for silica.

Since P85 is comprised of ethylene oxide (EO) and propylene oxide (PO) a brief summary of the properties of their homopolymer and block copolymers at the surface of hydrophilic quartz is provided in the following sections.

Absorption of the EO and PO Homopolymers

Polymer Adsorption

According to *Iler* [57] it is almost universally true that polymers tend to form a monomolecular layer at the solid-liquid interface. The adsorption is due to either ionic attraction, hydrophobic bonding, or hydrogen bonding. Polymers may have binding sites along the chain but in any case always at chain ends which contain polar atoms such as nitrogen, oxygen or double-bonded carbon atoms.

Factors Involved in Adsorption on Quartz

Iler [57] states, that three factors are involved in the adsorption on quartz. The degree to which linear polymer chains are adsorbed flat on the SiOH surface depends on the strength of hydrogen bonding of SiOH with the polar groups as well as competition of the solvent and the polymer for the SiOH surface. Secondly, the adsorption on silica involves the number of hydrocarbon to polar atoms in the molecule. According to *Iler* it is directly related to the tendency of hydrocarbon atoms or chain segments to escape from water and collect at an interface. Finally, the number of points of attachment to the surface is important.

As P85 has two outer segments of poly(ethylene oxide) it is important to look separately at the properties of ethylene oxide as it determines the adsorption at hydrophilic surfaces. From ellipsometry measurements [135] the tendency of PPO to adsorb to hydrophilic silica was found to be small or non-existent. Conversely, PEO was in this study only seen to adsorb in negligible amounts on hydrophobized silica.

Studies of EO

A large number of studies have been performed on ethylene oxide due to its advantageous properties in steric stabilization of colloids. Even though the surfaces of silica are highly dependent on the treatment, some of the most important conclusions that can be drawn from these studies are:

- Poly(ethylene oxide) is adsorbed to silica and that (suggestively) "isolated silanol groups provide the best adsorption sites, acting as proton donors in hydrogen bonding to ether oxygens -SiOH$\cdots$O(CH_2CH_2)" [120, 56, 57].
- In an aqueous medium the hydrogen bonding of ethylene oxide must be reduced by competition with water molecules [120].
- The hydrodynamic thickness of the adsorbed layer δ is proportional to the molecular weight M_w:

$$\delta \propto M_w^a, M_w = 4 \times 10^4 - 3.3 \times 10^6 \quad (3)$$

  where a was found to 0.5, increasing to 0.8 for a porous layer both experimentally and theoretically [63].

Curvature of the Surface

It was early realized from adsorption on latex spheres, that the curvature of the surface is of importance since a larger curvature of the surface allow polymer segments greater access to the regions immediately adjacent to the particle surface, resulting in an effectively higher segment density but a lower adsorption density. Several theoretical approaches have been made to describe adsorbed polymers at a curved interface. Among the more successful are self-consistent mean field (SCF) [83, 39, 72] and single chain mean field (SCMF) theory [131], where the latter is valid for shorter chains as is encountered in triblock copolymers whereas the former is applicable to longer chains typically used in diblock copolymer adsorption.

Triblock Copolymers

Loops, Trains, and Tails

For block copolymers the absorption typically occurs in loops, trains, and tails depending on the solvent and the character of the surface (see Figure 4). On a hydrophilic surface, loop and train conformations have been suggested for the EO-PO containing triblock copolymers [70] based on photon correlation spectroscopy measurements.

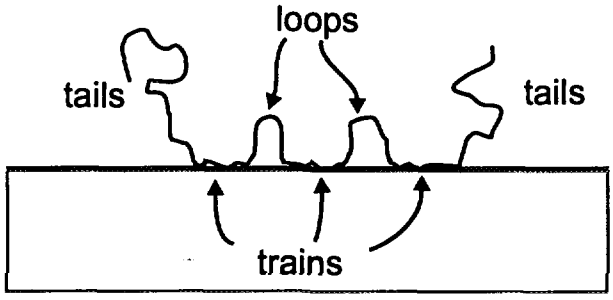

Figure 4. Loops, trains and tails of an adsorbed triblock copolymer.

Adsorption on Spheres

From the studies of adsorption on both silica and polystyrene latex spheres in aqueous solution [63], it was found that on hydrophobic surfaces the triblock copolymers adhere to the surface by van der Waals or hydrophobic interaction of the hydrophobic PPO segments with the hydrophilic EO extending into the solution. On hydrophilic silica the SiOH form hydrogen bonds with PEO (and to a lesser degree PPO) part of the triblock copolymer. The adsorption mechanism of triblock copolymers resembles homopolymer adsorption of EO on silica.

Adsorption on a Flat Surface

Ellipsometry experiments of PEO-PPO triblock copolymers adsorbed onto both hydrophilic [79] and hydrophobized [135] flat silica surface have been performed.

On the hydrophilic surface it was found that the adsorbed amount increases considerably just prior to the critical micelle temperature where-after it levels off to a plateau value. This behaviour is similar to EO homopolymer adsorption and has likewise been found in C_nE_m [134]. The time scale for the adsorption and desorption kinetics was measured to be within a few minutes.

Killmann et al. [63] found from photon correlation spectroscopy measurements that the thickness of PEO-PPO block copolymers, in contrast to PEO, adsorbed to precipitated silica is independent of the molar mass and attains a value of approximately 20 Å. However, this study was only performed in a limited molecular weight regime from 7×10^3 to 1.5×10^4 and at single concentration at the plateau value of adsorption.

On hydrophobized silica *Tiberg et al.* [135] suggested that PPO homopolymer adsorption was due to not only a hydrophobic attraction between PPO segments and the surface but also to the poor solvent conditions for the segments.

Theoretical Approach

Recently, *Linse et al.* [74] has extended the lattice model of *Scheutjens and Fleer* to include the assumption of the two conformations of the EO chain, which was introduced by *Karlström* and has been shown to reproduce qualitatively the concentration-temperature diagram for the Pluronics. From this model an excess of EO was predicted on a hydrophilic surface closest to the surface and extending into the solution shielding a layer of PPO in accordance with experiment. The preferential absorption on surface was explained from the model as a reduced fraction of polar states of PO and EO on approaching the surface, making the segment-solvent interaction less favourable.

As we have seen above the single chain adsorption and structure of single chains have been well understood. Since only limited work has been done on the surface

ordering of triblock copolymer aggregates, it will be the main topic of the remaining part of the present thesis.

1.3 Overview

The outline of this thesis is based on the exploration of the different types of aggregates of the triblock copolymer P85.

In Chapter 2 a model for the P85 micelle is established for which the scattering form factor can be expressed analytically. The developed model is used to analyse small-angle scattering data from P85 micelles and poly(styrene)/poly(isoprene) micelles in solution.

Chapter 3 focuses on the surface-induced structure of P85 micelles at the solid-liquid interface. The micellar model of Chapter 2 is extended to explain neutron reflectivity data by incorporating simulations of hard spheres at a hard wall.

In Chapter 4 details of the derivation of the numerical expression for the micellar surface ordering is given. Special attention is paid to the computer simulations and the parameterization necessary for the numerical expression.

Chapter 5 treats the morphologies of the bulk anisotropic aggregates of P85 on the quartz surface occurring at higher temperatures and the response to Poiseuille shear flow.

The last chapter is devoted to the attempt to understand the surface ordering of the micellar BCC crystal and the changes with temperature.

Finally, the main results of these investigations are summarized in the conclusion.

2 Micelle Model

Micelles as Model for End-grafted Polymers at a Curved Interface

Micelles have proven to be a valuable model system for investigating polymers end-grafted to a curved interface. Knowledge of the conformation of the these polymers, the tethered polymers, is crucial in the understanding of the interaction between micelles. Block copolymers composed of two parts, where the solvent is poor for one of them, can, for example, form spherical micelles in solution. The radius of curvature of the micellar core and thus the morphology of the anchoring interface can easily be changed by altering e.g. the temperature and concentration of the copolymer in solution. The conformation of the tethered chains is strongly dependent on the radius of curvature due to the difference in the available volume for the polymer chains. The two extremes are the star-like and the brush conformations. The brush conformation is known from the extensive investigations of polymer conformations at planar interfaces. Depending on the grafting density, which is the number of chains attached to the interface per area, the polymer will form either a mushroom- or brush-like conformation. In the former case the polymers do not interact, whereas in the latter case steric repulsion extends the polymers into the solution. Scaling theory [3, 27] and self-consistent field (SCF) theory [86] have been successful in the prediction of the density profile of tethered polymers. SCF calculations predicted a parabolic concentration profile for the brush for weak excluded-volume interactions and high surface coverage. Computer simulations [66, 98] and experiments (e.g. by surface force apparatus measurements [65] and neutron reflectometry [33, 34, 62]) have verified these findings. Furthermore, several studies have investigated the brush-to-mushroom transition as a function of grafting density, solvent quality, and polymer architecture [33, 34]. Recently, the more demanding curved interfaces have been the focus of attention by self-consistent field calculations [39, 83], Monte Carlo simulations [136], and experiments [39]. Scaling theory [25] has predicted that chains tethered to a small spherical core will have a polymer density profile which follows a power law decay away from the center of the core on the form $\rho(r) \approx (r/b)^{(1/\nu)-3}$, where ν is the Flory exponent reflecting the quality of the solvent and b is the statistical segment (Kuhn) length. In a good solvent $\nu = 0.6$, whereas $\nu = 0.5$ for a θ solvent[3]. The basic assumption is that the chains have a single free-chain behaviour within a blob of dimension $\xi(r)$. The blobs are close-packed around the center sphere. The scaling behaviour breaks down when the core size of a polymeric micelle becomes too large or when the coronal chain length is too short. For a larger core-to-chain size the volume fraction profile of the tethered polymers has a more parabolic form. *Gast* [39] found for polystyrene (PS)/polyethylene oxide (PEO) micelles in dilute solution, that diblock copolymers of 1700 repeat units of PS and 170 units of PEO obey the star-like scaling prediction, but it was found not to hold for a diblock copolymer having 80 units of PS and 65 PEO. The break down of the scaling was attributed to the non-random walk behaviour of the short chains. For an extensive review on tethered chains see e.g. *Szleifer & Carignano* [131] and *Gast* [39].

Star-like or Brush Conformation

Mushrooms and Brushes at a Flat Interface

Tethered Polymers at a Curved Interface

P85 Micelles

In the structure analysis of the triblock copolymer P85 in aqueous solution, the spherical micelles have been suggested to consist of a spherical core of the insoluble part, poly(propylene oxide), surrounded by a shell of dissolved polymer chains of poly(ethylene oxide). This shell is similar to the outer region of a multi-arm star polymer or a brush or mushroom consisting of end-grafted polymer chains. The two-shell picture has been used in e.g. the interpretation of SANS measurements [94, 89] of P85 micelles. To gain further insight on the structure of the

Two-shell Picture

[3]For a θ solvent the interactions between the chain segments, and the chains and the solvent are equal.

micelle, a more detailed model is developed in the present chapter. Here, the micelle is modeled as a spherical core of radius R with chains attached at the surface (see Figures 5 and 6). An analytical expression for the form factor is calculated and compared to both Monte Carlo simulations and small-angle scattering experiments. Furthermore, Monte Carlo simulations are performed to remove the unphysical penetration of the core by the chains, i.e. include excluded volume effects between the chains and the core in the model. The self-avoidance of the chains is neglected.

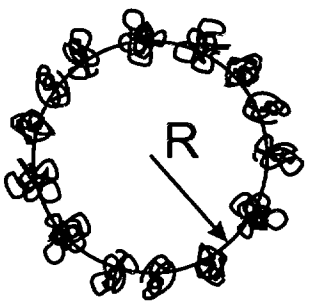

Figure 5. The mathematical model of the micelle: Gaussian chains attached to a sphere of radius R.

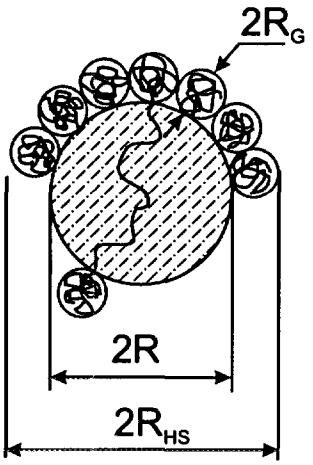

Figure 6. The physical model, which includes the excluded volume effects between the tethered chains and the core of the micelle. The thickness of the attached polymer layer is $2R_g$. The radius of the core is R and the interaction radius between micelles is R_{HS}.

2.1 Small-Angle Neutron Scattering

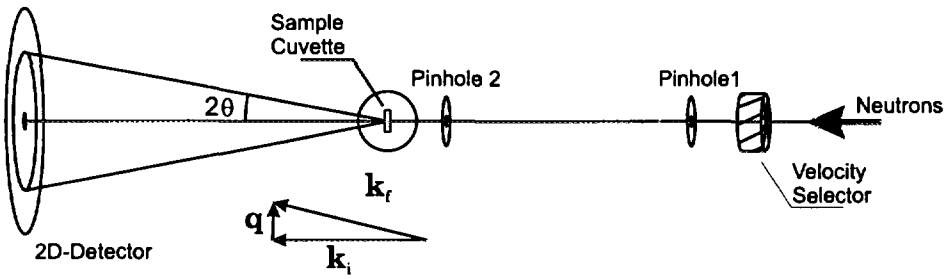

Figure 7. A schematic view of the small-angle neutron set-up at Risø National Laboratory.

Small-angle scattering has proven to be a very successful technique for structural investigations of macromolecules and their aggregates in solution with characteristic length scales in the range from 10 to 3000 Å [43]. Both X-rays and neutrons are used as probes and provide complementary information of the samples as these probes scatter from electrons or nuclei, respectively. Especially, the difference in scattering length of hydrogen (H) and deuterium (D) for neutrons makes

it possible to alter the contrast between the solvent and the macromolecules by either selective deuteration or contrast variation. In this way, different parts of the molecules can be investigated: The former by exchanging hydrogen with deuterium in the macromolecules and the latter by using different mixtures of H_2O and D_2O. Usually, D_2O is used as solvent in order to obtain good contrast and low background.

Selective Deuteration

The small-angle neutron set-up used at Risø National Laboratory is shown in Figure 7. The wavelength of the cold neutrons is between 3 and 15 Å and is chosen by the velocity selector, a rotating drum of thin helical ordered sheets coated with the neutron-absorbing material cadmium. The wavelength spread $\Delta\lambda/\lambda$ can be chosen by changing the angle of the plates to the incoming neutron beam. Here, $\Delta\lambda$ is the full-width-at-half-maximum value of the neutron wavelength distribution. The neutrons are collimated by two pinholes or two vertical slits, their mutual distance being matched to the sample-to-detector distance. After the neutrons have been scattered by the sample, they are detected by a two-dimensional detector of radius 0.28 m. For the experiments presented in this chapter three settings with 9.6, 4.7, and 2.8 Å neutrons with a spread of $\Delta\lambda/\lambda = 0.18$ have been used with sample-to-detector distances of 6, 3, and 1 m, respectively. The absolute value of the scattering vector $\vec{q}$ is given by

Small-angle Neutron Set-up

$$q = |\vec{k_f} - \vec{k_i}| = \frac{4\pi}{\lambda}\sin\theta, \tag{4}$$

Length of Scattering Vector $\vec{q}$

where 2θ is the scattering angle between the incoming and scattered neutrons with wave vector $\vec{k_i}$ and $\vec{k_f}$, respectively. Hence, the current settings provide three different q-ranges: 0.0037-0.029, 0.015-0.12, and 0.084-0.57 $Å^{-1}$. The more subtle details of the instrumental set-up can be found in the thorough review by *Pedersen* [104]. Since the scattered intensity for non-oriented samples is azimuthally isotropic, an azimuthal average is performed leaving the intensity as a function of the length of the scattering vector q. The averaged intensity is corrected for the background arising from the quartz sample container, inhomogeneous detector response, and electronic noise, and finally it is normalised to the spectrum of H_2O.

Data Reduction

Basic Scattering Theory

When neutrons impinge on non-interacting particles the intensity of the scattered neutrons can be written on the form [43]

Non-Interacting Particles

$$I(\vec{q}) = C\left|\sum_i^N b_i \exp(-i\vec{q}\cdot\vec{r})\right|^2 \tag{5}$$

$$= C\sum_i^N\sum_j^N b_i b_j \exp(-i\vec{q}\cdot(\vec{r_i} - \vec{r_j})), \tag{6}$$

where the sum is performed over the number of atoms, N, in the particle. Here, $\vec{r}$ is the position of an atom inside the particle and C is a prefactor related to the incident flux of neutrons and the geometry of the small-angle scattering instrument.

In equation (5) the single sum is known as the *form factor* amplitude and consist of the scattering length b_i times a phase factor representing the difference in phase between an arbitrary zero point and a scatterer within the particle. As the number of scatterers inside the particle becomes large, $N \to \infty$, the intensity can be written on integral form

Form Factor Amplitude

Expression for the Intensity on Integral Form

$$I(\vec{q}) = C\left|\int_V \rho(\vec{r})\exp(-i\vec{q}\cdot\vec{r})d\vec{r}\right|^2, \tag{7}$$

where the scattering length density $\rho(\vec{r}) \equiv \int_{\text{particle}} b(\vec{r})/V_{\text{particle}} d\vec{r}$, V and V_{particle} being the total volume of the sample and the particle, respectively.

Spherically Symmetric Particles

For spherically symmetric particles, where $\rho(\vec{r}) = \rho(r)$, the expression can be further simplified [43]:

$$I(q) = 4\pi C \int_0^\infty p(r) \frac{\sin(qr)}{qr} dr. \tag{8}$$

Pair-Distance Distribution Function

Here, $p(r)$ is the pair-distance distribution function, which gives the probability of having two volume elements with a mutual distance between r and $r + dr$ weighted by the scattering length density within the particle. In simulations, the small angle scattering is typically calculated from the pair-distance distribution function $p(r)$. The $p(r)$ function is related to the scattering length density by the auto-correlation function $\gamma(r)$:

Auto-Correlation Function

$$p(r) = r^2\gamma(r) = r^2 \int_0^\infty \rho(r)\rho(r + r')dr'. \tag{9}$$

The aim here has only been a simplistic account of relations which govern small-angle scattering. More extensive accounts can be found in the works by *Guinier & Fournet* [46], *Glatter & Kratky* [43], and *Jacrot* [58]. With the necessary scattering theory in place, the form factor for the proposed micellar model will be calculated in the following section.

2.2 Analytical Expression for the Form Factor

In order to calculate the form factor, several different terms related to the distances within the micelle has to be determined: The self-correlation of the sphere, the self-correlation of the chains, the cross term between sphere and chains and the cross term between different chains. The normalized $[F_s(q = 0, R) = 1]$ self-correlation term for a sphere [113] with the radius R is given by $F_s(q, R) = \Phi(q, R)^2$, where $\Phi(q, R)$ is the form factor amplitude:

Self-Correlation Term for a Sphere

$$\Phi(q, R) = \frac{3[\sin(qR) - qR\cos(qR)]}{(qR)^3}, \tag{10}$$

and q is the length of the scattering vector. For chains with Gaussian statistics the self-correlation term is given by the Debye function [29]:

Self-Correlation Term for the Chains

$$F_c(q, L, b) = \frac{2[\exp(-x) - 1 + x]}{x^2}, \tag{11}$$

where $x = R_g^2 q^2$ and R_g is the radius of gyration given by: $R_g^2 = Lb/6$, where L is the contour length and b is the statistical segment (Kuhn) length of the chain.

Cross Terms

The cross terms are calculated taking a starting point in the Debye equation [28], which gives the scattering function of particles consisting of subunits with spherical symmetry. Let us first consider two infinitely thin shells of radii R_1 and R_2 separated by the distance r. The interference term for the scattering from these two shells is

$$\frac{\sin(qR_1)}{qR_1} \frac{\sin(qR_2)}{qR_2} \frac{\sin(qr)}{qr}, \tag{12}$$

where the two first terms represent the form factors of the shells and the last term is the phase factor due to the separation of their centers. In the cross terms for the micelle model, the objects under consideration are not thin shells but spheres or Gaussian chains. Therefore the first two $\sin(x)/x$ terms in equation (12) have to be integrated over R_1 and R_2, respectively, with appropriate weighting functions. For a sphere, the weighting function is $p_s(R_1) = 4\pi R_1^2$ for $R_1 \leq R$ and zero elsewhere. The integration gives the function $\Phi(q, R_1)$ in equation 10.

For a Gaussian chain, one has to consider the contribution from each point along the contour. For the point separated by the contour length l from the point of attachment, the probability distribution function for having the distance R_2 is given by

$$p_l(R_2) = 4\pi \left(\frac{3}{2\pi d_l^2}\right)^{\frac{3}{2}} R_2^2 \exp\left[-\frac{3}{2}\left(\frac{R_2}{d_l}\right)^2\right], \tag{13}$$

where $d_l^2 = bl$ is the mean-square distance between the two points. In order to get the full contribution at R_2, one also has to integrate over the contour length l. However, in order to perform the calculations analytically the integration over R_2 has to be performed first. This gives the phase factor:

$$\phi_l(q) = \int_0^\infty p_l(R_2)[\sin(qR_2)/(qR_2)]dR_2 = \exp(-q^2 d_l^2/6). \tag{14}$$

The integration over the points along the contour gives the amplitude form factor of the chain [50]:

$$\psi(q, L, b) = \frac{1}{L}\int_0^L \phi_l(q)dl = \frac{[1-\exp(-x)]}{x}, \tag{15}$$

where $x = R_g^2 q^2$ as before.

For a sphere with a chain attached to the surface the distance r in equation (12) is equal to the radius R of the core and the interference cross term becomes:

Sphere-Chain Interference Term

$$S_{sc}(q) = \Phi(q, R)\psi(q, L, b)\frac{\sin(qR)}{qR}. \tag{16}$$

In order to calculate the interference term between the chains attached to the surface of a sphere the proper weighting of the distance r in the phase factor of equation (12) has to be performed. The chains are assumed to be homogeneously distributed on the surface of the sphere and therefore the proper weighting function is the pair distance distribution function of an infinitely thin shell with radius R. The integration over r gives the form factor of an infinitely thin shell ($[\sin(qR)/(qR)]^2$) and the cross term becomes:

Interference Term between the Attached Chains

$$S_{cc}(q) = \psi(q, L, b)^2\left[\frac{\sin(qR)}{qR}\right]^2. \tag{17}$$

It is now possible to calculate the form factor of the micelle. If the aggregation number of the micelle is N_{agg} and the total excess scattering length of the blocks in the core and in the chains are ρ_s and ρ_c, respectively, one obtains:

$$\begin{aligned} F_{mic}(q) &= N_{agg}^2\rho_s^2 F_s(q, R) \\ &\quad + N_{agg}\rho_c^2 F_c(q, L, b) \\ &\quad + N_{agg}(N_{agg}-1)\rho_c^2 S_{cc}(q) \\ &\quad + 2N_{agg}^2\rho_s\rho_c S_{sc}(q). \end{aligned} \tag{18}$$

The forward scattering is:

$$F_{mic}(q=0) = N_{agg}^2(\rho_s + \rho_c)^2. \tag{19}$$

Note, that these expressions reproduce the form factor of a Gaussian star polymer for $R \to 0$ [14].

The next step is to compare the found expressions for the micelle model with Monte Carlo simulations. This will allows us to extend the model and incorporate the excluded volume interactions between the sphere and the chains.

2.3 Monte Carlo Simulations

In the derivation of the form factor the chains are free to penetrate into the core, which they would obviously not be allowed to do in a real system. In order to investigate this effect, Monte Carlo simulations of the micelles both with and without core penetration of the chains were performed. The Gaussian chains were generated as random walks in three dimensions starting at the surface of the sphere. All interactions between sections of the chains were omitted, i.e. no excluded volume effects of the chains were taken into account. In case of non-penetration of the core, the chains were first generated and simply rejected if they penetrated the core. For each simulation the center-chain $p_{\text{center}}(r)$ and the chain-chain $p_{\text{chain}}(r)$ distance distribution functions were generated from 1000 independent samples as a function of the radial distance r from the center of the sphere.

Simulations of Micelles With and Without Core Penetration

For N_{chain} chains with N_{segm} segments tethered to a core with N_{core} chains we obtain the forward scattering in an analogous way to the one used in the micelle model:

$$F(q=0) = (N_{\text{core}}\rho_s + N_{\text{segm}}N_{\text{chain}}\rho_c)^2, \tag{20}$$

where ρ_s is the scattering length density per segment of the core (sphere), and ρ_c the scattering length density per segment of the chains. For the non-interacting micelles the form factor $F(q)$ can be calculated from equation (8) by

Form Factor of Non-Interacting Micelles

$$\begin{aligned} F(q) &= N_{\text{core}}^2\rho_s^2\Phi(q,R)^2 + \\ &\quad N_{\text{chain}}^2N_{\text{segm}}^2\rho_c^2\int_0^\infty p_{\text{chain}}(r)\frac{\sin(qr)}{qr}dr + \\ &\quad 2N_{\text{chain}}N_{\text{segm}}N_{\text{core}}\rho_c\rho_s\Phi(q,R)\int_0^\infty p_{\text{center}}(r)\frac{\sin(qr)}{qr}dr \end{aligned} \tag{21}$$

Here, the first term is related to the distances within the sphere, the second term to the distances of the points on the chains, and the last term to distances between the sphere and points on the chains.

The analytical and the simulated form factors are compared in the following section for a range of core sizes and chain lengths.

Comparison between Simulation and Analytical Expression

Penetrating Chains. To test the agreement between the model and the simulations for the penetrating chains a micelle with 60 attached chains with 15 random steps in each was simulated. The core radius was chosen to be 10 times the unit step length of the random walks used for generating the chains.

For the penetrating chains there was very good agreement observed between the analytical and simulated results. However, the Kuhn length had to be adjusted to $b = 1.09$ from the initial value of unity. This is a finite size effect originating from the small number of steps in the chains and the relatively large value of q (up to $q = 3/b$) for which the scattering curves are calculated. In effect, the adjustment of b is linked to the assumption that the chains follow Gaussian statistics, which is only strictly valid for long chains and not the relative short chains in this study.

Good Agreement Between Analytical and Simulation Results

Non-penetrating Chains. In order to investigate which effect the excluded volume of the core has on the conformation of the tethered chains, eight different values of the core radius were chosen in the range between 0.625 and 80 times the unit step length of random walks used for generating the chains. Three different configurations with 60 tethered chains, each comprised of either 7, 15, or 30 random steps, and a single configuration with 30 tethered chains and 60 random

Excluded volume of the Core

steps in each were simulated. The small core-to-chain sizes resemble the conformations of star polymers in a good solvent and these cores have a highly curved surface. When the core radius becomes large compared to the tethered chains, the chain conformation will have a likeness to a mushroom conformation for polymers tethered to a flat surface.

For each configuration of the non-penetrating chains the normalized form factor $F(q)/F(0)$ was calculated for eight different contrasts

$$\frac{\rho_s^{\text{tot}}}{\rho_c^{\text{tot}}} = \frac{N_{\text{core}}\rho_s}{N_{\text{chain}}N_{\text{segm}}\rho_c}, \tag{22}$$

where $\rho_s/\rho_c = -4, -2, -1, -0.5, 0.5, 1, 2, 4$.

Eight Contrasts

The analytical model was simultaneously fitted to the eight different contrasts obtained from the simulations allowing only two parameters to vary; the radial distance of attachment of the chains ΔR and the effective Kuhn length b_{eff}. A simultaneous fit for a micelle with 30 chains with 60 random steps in each attached at a core with a radius of 40 chain units is depicted in Figure 8.

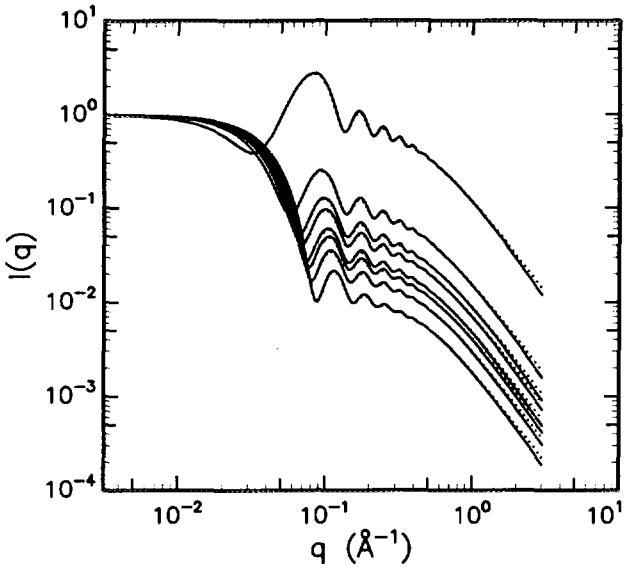

Figure 8. Calculated (dotted curves) and simulated (full curves) normalized scattering function $I(q) = F(q)/F(0)$ for eight different contrasts for 30 attached chains with 60 random steps in each attached to a core with radius of 40 chain units. The contrast are from top to bottom $\rho_s/\rho_c = -0.5, -1, -2, -4, 4, 2, 1, 0.5$. In the analytical expression the Gaussian chains are starting at $R' = R + 1.2R_g$.

General Features of The Normalized Scattering Function

Figure 8 shows general features occurring for both the penetrating and non-penetrating chains. At large q the scattering curves obey a q^{-2} behavior of $F(q)/F(0)$ which is characteristic for Gaussian chains. The same exponent of q is valid for star-like polymers, whereas linear chains radiating from the core follows a q^{-1} dependence. For the positive values of the contrast the scattering functions are dominated by the scattering from the spherical core at low q (lower four curves), whereas for the corresponding negative values, the scattering functions show large amplitude oscillations due to the abrupt change in the sign of the scattering length density at the surface of the sphere. The scattering curves for the non-penetrating chains are shifted slightly with respect to the curves for the penetrating chains. This is mainly caused by a shift of the position of the chains due to the space occupied by the sphere, which is unavailable.

$\Delta R/R_g$ Versus R/R_g

One of the main results from the fitting of non-penetrating spheres is comprised in Figure 9, where the increment, $\Delta R/R_g$, is plotted versus the radius of the sphere, R/R_g, for the four different chain lengths. As pointed out by *Szleifer & Carignano* [131], the relevant scaling parameter for chains, which are too short to obey scaling laws, is the radius of gyration of the tethered chains, R_g, given by $R_g^2 = N_{segm} b_{eff}^2/6$ and not the distance between tethering points. All the curves have the same functional form even though they do not collapse to a single curve. The form of the curves can be understood in terms of the excluded volume imposed on the chains by the core. For a radius of the core, which is small compared to length of the chains, only a small part of the configurational space is occupied by the core. This will hardly affect the random walk of the chains and the chains only have to move slightly outward to regain the lost volume. As the radius of the core increases, the points of attachment of the chains have to move further outward in order to compensate for the lost volume and $\Delta R/R_g$ increases. However, when the core radius becomes very large, a plateau level is reached. The reason for the plateau lies in the fact, that for large core radii, half of the volume originally occupied by the tethered chains, $4\pi R_g^3/3$, is removed. A further increase in core radius will not have a marked effect on the size of the excluded volume. This is similar to a flat interface, which is the limiting case as $R \to \infty$ of the anchoring surface.

The Difference in $\Delta R/R_g$ Curves

The long chains are extended further outward from the surface of the core compared to the short chains even though the size dependence has been accounted for by normalisation to R_g of the chains. An explanation is that the longer chains, which are comprised of a large number of random steps, are more likely to be rejected by making an incursion into the spherical exclusion zone. Moreover, the further outward the point of attachment is from the center of the core the less likely it is for the chains to encounter the excluded volume due to the larger volume available. Thus, the longer chains are moved further outward compared to their size (R_g) as a result of a combination of these two effects. A more simple explanation is that the difference is a finite N effect, where N is the number of segments.

The Cross-over and Plateau Value of $\Delta R/R_g$

Figure 9 implies that two quantities are relevant to investigate: The plateau value of $\Delta R/R_g$ at large R/R_g and the cross-over to the plateau value of $\Delta R/R_g$. Figure 10 shows the relation between the plateau value of $\Delta R/R_g$ and the number of segments of the tethered chains. The plateau level is almost constant, signifying that starting points of the chains are moved from the distance R to $R' \approx R + R_g$ from the center of the sphere. Note, that the shorter chains are moved a smaller distance away from the surface of the core compared to their size than the longer chains. Figure 10 shows the cross-over value of R/R_g as a function of $\sqrt{N_{segm}}$, which is proportional to the radius of gyration of the chains, R_g. The plot indicates that the shorter chains are more sensitive to the changes in excluded volume, since they reach the plateau level at higher values of R/R_g. The sensitivity to the excluded volume of the shorter chains arises due to the fact that these chains have their point of attachment closer to the surface of the core and therefore are affected to a higher degree by the excluded volume.

In the next section, it will be shown that there is a considerable agreement between the micelle model experiments from micellar systems.

2.4 Experiments

The applicability of the model to real systems of micelles was investigated by performing SANS experiments of P85 at several concentrations in D_2O and from other published examples.

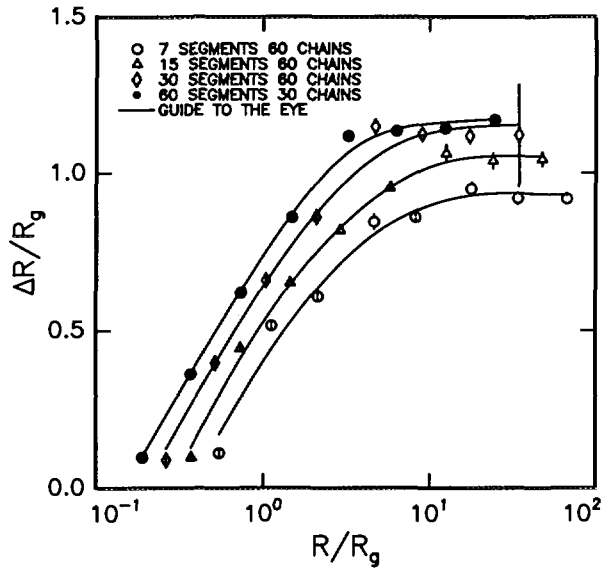

Figure 9. The displacement of the chains as a function of the radius of the core R both normalized to the radius of gyration of the chains, R_g, for four different configurations.

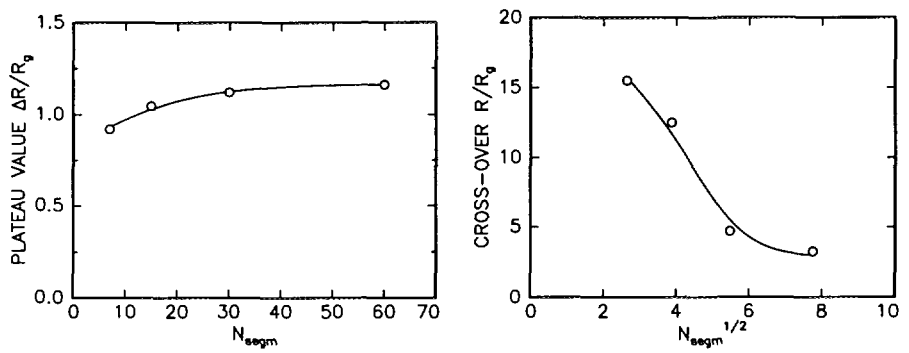

Figure 10. The left figure shows the plateau value as a function of the total number of segments and the right the cross-over as a function of $\sqrt{N_{\rm segm}} (\propto R_g)$.

SANS Measurements of P85 Micelles

The first example is micelles of P85 dissolved in D_2O in concentrations from 0.25 to 10 wt % in a temperature range from $T = 50$ to 60°C. The measurements were performed at the SANS instrument at Risø National Laboratory [104]. Figure 11 shows four different scattering curves for 0.25, 1, 5, and 10% solutions at a temperature of $T = 50$°C. The q^{-2} scattering from the Gaussian chains around the core is clearly observed at large q. In order to illustrate this behaviour, a Kratky plot, showing the intensity multiplied by q^2, is depicted in Figure 12. At the higher concentrations, we see the appearance of a peak at $q = 0.04$ Å^{-1} indicating increasing correlations in the suspension.

q^{-2} Scattering from the Gaussian chains

The inter-micellar effects were included in the analysis of the SANS data using a hard-sphere structure factor $S_{HS}(q)$ for mono-disperse spheres following *Mortensen & Pedersen* [94]. The structure factor is generally given by [46]

Inter-Micellar Effects

$$S(q) = 1 + 4\pi N \int (g(r) - 1) \frac{\sin(qr)}{qr} r^2 dr, \tag{23}$$

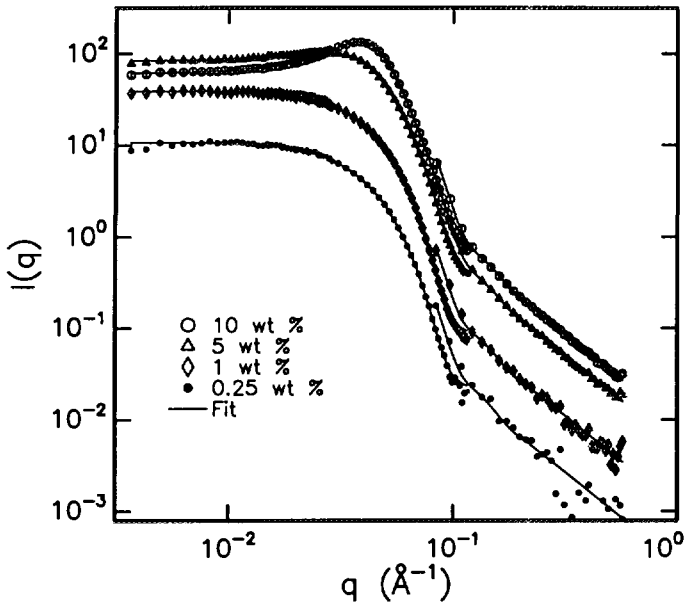

Figure 11. Four concentrations: 0.25, 1, 5, and 10 wt % of P85 in D_2O at 50° C. The data were recorded using three instrumental settings. Note, that the data from different settings overlap due to the instrumental smearing. The solid line is the model fit to the data. The peak appearing close to 0.04 Å^{-1} for 10 wt % indicates the increasing correlation between micelles in the solution.

where N is the number density of scatterers and $g(r)$ is the radial distribution function describing the arrangement of the micelles. For a hard-sphere interaction potential

$$\Phi(r) = \begin{cases} \infty & \text{for } r < R_{\mathrm{HS}} \\ 0 & \text{for } r \geq R_{\mathrm{HS}}, \end{cases} \tag{24}$$

where R_{HS} is the hard-sphere interaction radius, the structure factor can be obtained on analytical form in the Percus-Yevick approximation [64, 109]:

Percus-Yevick Approximation

$$S(q) = \frac{1}{1 + 24\eta G(2qR_{\mathrm{HS}}, \eta)/(2qR_{\mathrm{HS}})}, \tag{25}$$

where G is a trigonometric function of $x = 2qR_{\mathrm{HS}}$ and the hard-sphere volume fraction η:

$$\begin{aligned} G(x,\eta) &= \frac{\alpha(\eta)}{x^2}[\sin(x) - x\cos(x)] + \\ &\quad \frac{\beta(\eta)}{x^3}[2x\sin(x) + (2 - x^2)\cos(x) - 2] + \\ &\quad \frac{\gamma(\eta)}{x^5}[-x^4\cos(x) + 4[(2x^2 - 6)\cos(x) + \\ &\quad (x^3 - 6x)\sin(x) + 6]], \end{aligned} \tag{26}$$

with

$$\alpha(\eta) = (1 + 2\eta)^2/(1 - \eta)^4 \tag{27}$$

$$\beta(\eta) = -6\eta(1 + \eta/2)^2/(1 - \eta)^4 \tag{28}$$

$$\gamma(\eta) = (\eta/2)(1 + 2\eta)^2/(1 - \eta)^4. \tag{29}$$

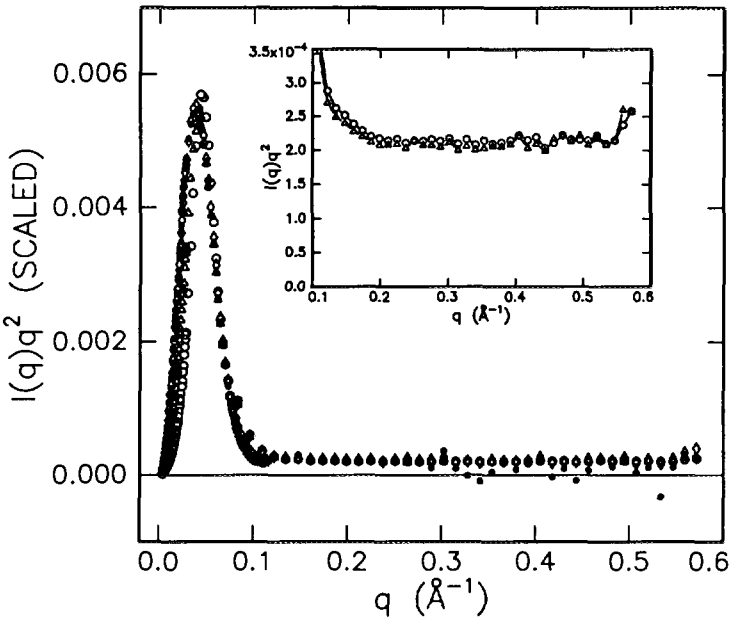

Figure 12. The corresponding Kratky plot for the data in Fig. 11, which almost collapse to a single curve when scaled to the intensity of 0.25 wt %. The same symbols have been used as the above figure. The insert shows the q^{-2} behaviour originating from the tethered Gaussian chains.

Physical Constants for P85 Micelles

The excess scattering length densities were calculated from the composition of the P85 triblock copolymer and the specific volumes, which can be derived from density measurements [12]. Polydispersity of the micelles was included using a Schulz-Zimm distribution for the aggregation number [87, 129]. In a first attempt, the core was assumed to be constituted solely of the PPO parts of the chains. For each aggregation number the radius of the core was calculated from the PO monomer volume V_{PO} = 96.2 Å^3, V_{PO} = 96.4 Å^3, and V_{PO} = 96.9 Å^3 derived from the specific volumes at 50, 55, and 60°C [12, 105], respectively. The contour length of the PEO chain was calculated to be 90 Å from the bond length and the bond angles [1, 37]. The distance from the surface of the core to the starting points of the Gaussian chains was left as a fitting parameter.

Scattering Intensity

The scattering intensity was described by

$$I(q) = \frac{c}{M}\langle F_{mic}(q)\rangle S_{HS}(q), \tag{30}$$

where c is the mass concentration of sample and M is the average mass of the micelles. $\langle F_{mic}(q)\rangle$ is the form factor in equation (18) averaged over the distribution of aggregation numbers. The theoretical scattering curve was smeared by the instrumental resolution function [107] when fitted to the experimental scattering data.

Model Fits to SANS Data

The model gave reasonable fits to the scattering data (see Figure 11). The main deviations were in the region where the scattering data cross over to the q^{-2} behavior. In order to get perfect agreement in this region it was necessary to include a low density PEO shell around the core in accordance with the suggestion by *Mortensen & Pedersen* [94]. The inclusion of the shell gave rise to two additional parameters: The fraction that the PEO shell constitutes of the total volume of the PEO chains, $V_{\mathrm{PEO,shell}}/V_{\mathrm{PEO}}$, and the fraction of the shell which is occupied by EO, $V_{\mathrm{PEO,shell}}/V_{\mathrm{shell}}$. The results are tabulated in Table 1 and depicted in Figure 13.

Low Density PEO Shell

Temperature and Concentration Dependence

For temperatures above $T = 50°C$ and concentrations above 2 wt %, the R_{HS}/R was below one, which is unphysical. Therefore, in these cases R_{HS}/R was fixed to unity in the fitting. The reason for the discrepancy is likely to be more elongated micelles driven by the increasing hydrophobicity of EO with increasing temperature. For the lowest temperatures below a concentration of 5 wt %, the aggregation number N_{agg} and therefore the size of the core is nearly constant as a function of the concentration (see Figure 13(a)): $N_{agg} = 73$ and 82 at 50°C and 60°C, respectively. The aggregation numbers correspond to a core radii of 41 and 42 Å in each case. However, a decrease in the aggregation number can be seen at higher concentrations (e.g. from $N_{agg} = 73$ at 0.5 wt % to 63 at 10 wt % at 50°C), where intermicellar correlations start to be significant. Figure 13(b) shows that the volume fraction η increases with increasing concentration which agrees with earlier findings by *Mortensen & Pedersen* [94], who treated the micelle as a solid sphere in the Percus-Yevick approximation. A noticeable difference between the present study and the one by *Mortensen & Pedersen* is the decrease in volume fraction for 60°C compared to the expected similar values obtained for 50 and 55°C (see Figure 13). This finding strengthens the hypothesis that the micelles depart from the spherical symmetry already at $T = 60$ °C.

Aggregation Number

PEO Shell

Figures 13(d) and 13(e) show that the additional shell contains approximately 24 and 28% of the PEO chains at 50°C and 60°C, respectively, with a water content ($= 1 - V_{PEO,shell}/V_{shell}$) of 77 and 75% for the same temperatures, decreasing slightly with temperature. The radius of the second shell is 50 Å at 50°C and 52 Å at 60°C.

Polydispersity

The polydispersity of the aggregation number attains an almost constant value of $\sigma(N_{agg})/N_{agg} = 0.40$, where $\sigma(N_{agg})$ is the standard deviation of the Schulz-Zimm distribution (see Figure 13(e)). However, an increase in polydispersity is observed for the higher concentrations. The corresponding polydispersity of the radius of the core is $\sigma(R)/R \approx 1/3\sigma(N_{agg})/N_{agg} = 0.13$. This relatively large polydispersity explains the observations reported in Ref. [88] that the shear-induced BCC phase observed at higher concentration only possesses angular order and not positional order.

The Kuhn length is determined to be $b = 10$ Å, which is slightly larger than the value of 7.7 Å determined from measurements of the plateau modulus of melts [1].

Starting Point of the Tethered Chains

The starting point for the chains is approximately $0.3 \times R_g$ away from the surface of the PEO shell (see Figure 13c), where the radius of gyration of the chains is $R_g = 11$ Å. In general, the fits for 50°C show a better correspondence to the experimental data than the ones for 60°C. This can possibly be explained by the

wt %	T (°C)	N_{agg}	$\Delta R/R_g$	η_{HS}	R_{HS}/R	$V_{PEO,shell}/V_{PEO}$	$V_{PEO,shell}/V_{shell}$	$\sigma(N_{agg}/N_{agg})$
0.25	60	80.6±0.2	0.70±0.01	0.014±0.001	1 (fixed)	0.32±0.01	0.267±0.003	0.368±0.004
0.5	50	73.0±0.2	0.25±0.01	0.016±0.001	1.19±0.04	0.24±0.003	0.23±0.002	0.37±0.004
	60	82.7±0.2	0.52±0.01	0.013±0.001	1 (fixed)	0.306±0.005	0.275±0.002	0.380±0.004
1	50	72.0±0.2	0.30±0.01	0.025±0.001	1.06±0.02	0.24±0.003	0.23±0.002	0.35±0.005
	60	82.3±0.2	0.30±0.01	0.022±0.001	1 (fixed)	0.279±0.003	0.247±0.002	0.378±0.004
2	50	73.9±0.2	0.32±0.01	0.035±0.001	1.01±0.02	0.248±0.004	0.239±0.002	0.371±0.006
	60	81.0±0.4	0.39±0.02	0.02 (fixed)	1 (fixed)	0.284±0.005	0.222±0.003	0.494±0.008
5	50	65.0±0.4	0.37±0.01	0.118±0.001	1 (fixed)	0.247±0.003	0.265±0.003	0.378±0.004
	55	74.3±0.2	0.35±0.01	0.110± 0.001	1 (fixed)	0.289±0.003	0.317±0.003	0.386± 0.004
	60	76.8±0.3	0.36±0.01	0.063±0.002	1 (fixed)	0.306±0.004	0.299±0.003	0.455±0.005
10	50	63.5±0.2	0.43±0.01	0.221±0.001	1 (fixed)	0.224±0.003	0.322±0.004	0.373±0.003
	55	71.7±0.3	0.37±0.01	0.202±0.001	1 (fixed)	0.251±0.005	0.344±0.006	0.384±0.005
	60	71.3±0.3	0.63±0.02	0.137±0.002	1 (fixed)	0.294±0.007	0.414±0.008	0.453±0.006

Table 1. Results from the modeling of the spherical P85 micelles. The uncertainties are obtained from the fitting procedure.

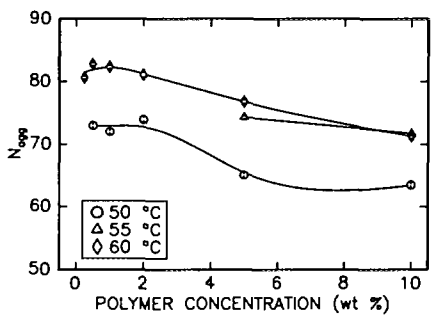

(a) Aggregation Number

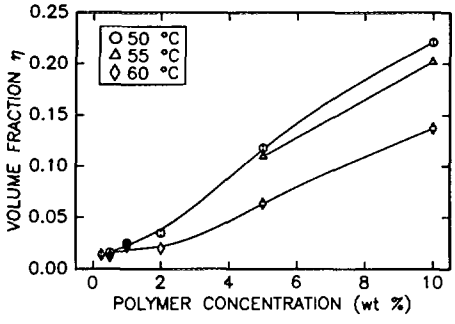

(b) Hard-Sphere Volume Fraction

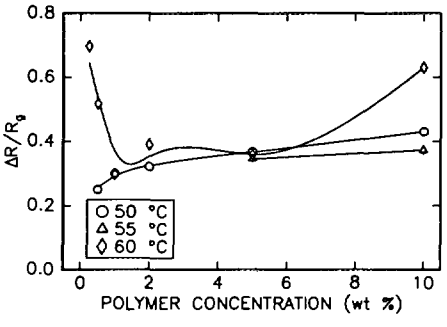

(c) Point of Attachment

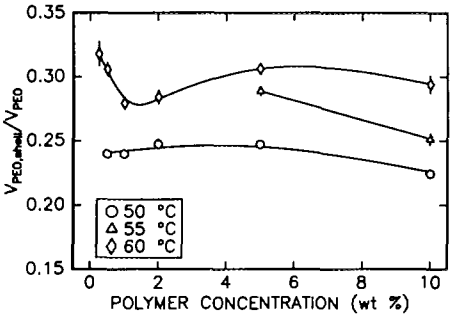

(d) Fraction of the PEO chains in the additional shell

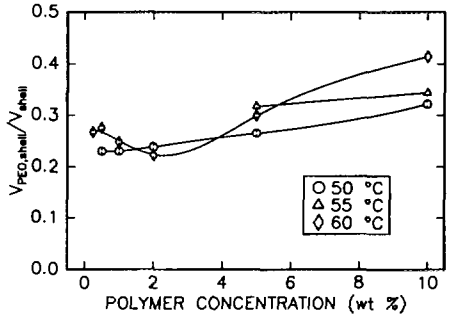

(e) Fraction of PEO (compared to water) in the additional shell

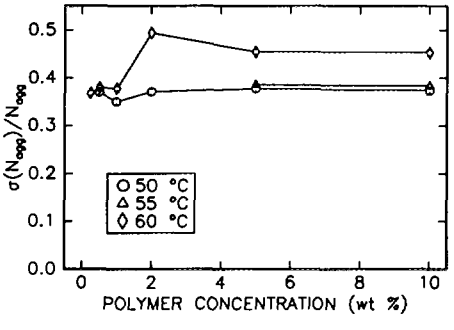

(f) The polydispersity of the aggregation number

Figure 13. The concentration and temperature dependence of the parameters in the micellar model when fitted to SANS data of P85 in aqueous solution. The full lines are guides to the eye.

elongation of the micelles leading to the phase transformation to prolate ellipsoids as suggested by *Mortensen & Pedersen* [94] which explains the discrepancies seen especially at 60°C.

Conformation of the PEO Chains

An indication of whether the poly(ethylene oxide) chains have a brush or mushroom conformation can be found from a comparison between the area available per chain on the surface of the core and the projected area of a single chain. Assuming that each chain occupies a volume equal to $(4/3)\pi R_g^3$, the latter area can estimated as πR_g^2 which equals 366 Å^2 for the 25 monomers of ethylene oxide. The

area available per chain at the point of attachment of the chains (approximately $R + R_g$) is given by

$$\frac{1}{\sigma_G} = \frac{4\pi(R+R_g)^2}{2N_{agg}} \tag{31}$$

where σ_G is the grafting density. We obtain 233 and 215 Å^2 from the aggregation numbers $N_{agg} = 73$ at 50°C and 83 at 60°C. Hence, the area available is approximately 60 % of the area needed for a single chain, i.e. the chains must overlap. This simple and rough estimation indicates that the polymers have a slightly deformed mushroom conformation.

Comparison of SANS and SAXS Measurements

A comparison between SANS and small-angle X-ray scattering (SAXS) data recorded by Glatter *et al.* [44] for 1 % P85 in D_2O is shown in Fig. 14.

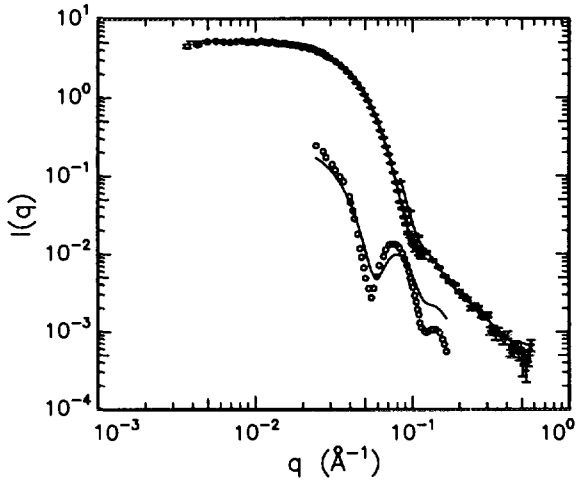

Figure 14. The small-angle neutron scattering data of 0.5% P85 ($EO_{25}PO_{40}EO_{25}$) in D_2O (upper data). The data were recorded using three different instrumental settings. The curve is the fit by the analytical model including polydispersity of the micelles. Note that the fitted curve is discontinuous where the data from different settings overlap due to the instrumental smearing. The lower data are SAXS results on similar micelles. The curve is calculated for the results determined by fitting the SANS data.

The two scattering curves are remarkably different due to the difference in contrast between the different parts of the micelle and the solvent. For SAXS the excess electron density of the PPO is slightly negative and significantly smaller than the (positive) electron density of the PEO. The electron densities were calculated from the measured densities [12]. Thus, the scattering is dominated by the PEO shell in contrast to SANS where the core contrast with the solvent is predominant. Using the parameters obtained from the SANS fit the corresponding scattering intensity of the resulting model for X-rays was calculated. The resulting intensity, after adjusting only an over-all scale factor, is shown in Figure 14. The model intensity curve reproduces the pronounced oscillation at $q \approx 0.1$ Å^{-1} in the measured data and a reasonable qualitative agreement is obtained.

d-PS-PI Diblock Copolymer Micelle

The small-angle neutron scattering data of 2% *d*-PS-PI (polystyrene (deuterated)-polyisoprene) in *d*-decane are shown in Fig. 15 [32]. The molecular weight of the PS and PI blocks are 10000 and 7500, respectively. The PS is insoluble in decane and micelles are formed. The deuterated PS core has a scattering length density which is close to that of the solvent and therefore the main part of scattering intensity originates from the PI chains. One observes also for this example a q^{-2} behavior at large q. The SANS data from the shell of PS chains has a pronounced secondary maximum in the form factor at around $q = 0.03$ Å^{-1} and it is quite different from the SANS data for the P85 micelles. It is in fact similar to the SAXS data for the P85 micelles for which the scattering is dominated by the scattering from the chain shell.

The scattering length densities were determined from the densities given in Ref. [20] using the known composition of the molecules. The contour length of the PI chains was calculated to be 139 Å[1]. Due to the relatively large concentration it was also necessary to include the hard-sphere structure factor to describe the inter-particle interference effects.

Model Reproduces the Pronounced Maxima

The fit to the scattering data is shown in Fig. 15. The model reproduced quite well the pronounced maxima at 0.03 Å^{-1} and the q^{-2} behavior at large q. The fit was obtained for the following parameters: $N_{agg} = 230$ ($R_{av} = 95$ Å), $\sigma(N_{agg})/N_{agg} = 0.30$, $b = 19$ Å, and $R_g = 21$ Å. The center of the Gaussian chains is moved $0.90 \times R_g$ further away from the surface of the core. The aggregation number and radius are a good agreement with the estimates given in Ref. [32]. The value for b is somewhat larger than the value ($b = 8.8$ Å) determined for melts of PI [1].

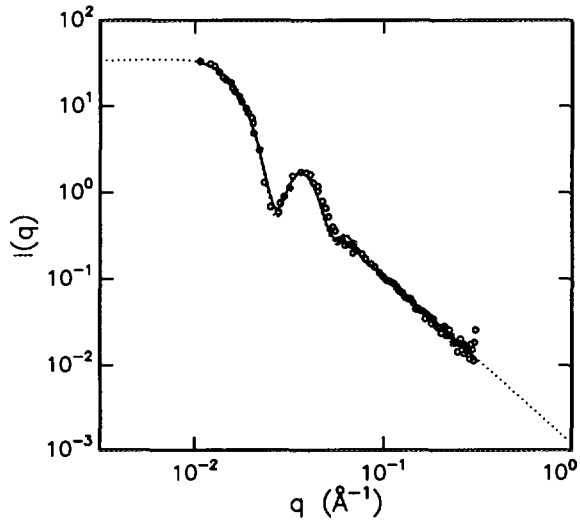

Figure 15. The small-angle neutron scattering data of 2% d-PS-PI in d-decane. The curve is the fit by the analytical model including polydispersity of the micelles.

2.5 Discussion

In the present chapter an analytical expression for the form factor of a micelle has been presented. The micelle was treated as a sphere with tethered Gaussian polymer chains. The form factor was found to agree with Monte Carlo simulations of chains, generated by three dimensional random walks starting at the surface of

a spherical core. Neither self- nor mutual avoidance of the chains were included in the simulations. Several radii of the spherical core were simulated from 0.625 to 80 unit step lengths of the random walks of the chains and the considered chain lengths were in the short to intermediate range (7 to 60 steps). The conformations with a small core-to-chain size correspond to star-like polymers, whereas a large core-to-chain size is related to the mushroom regime of polymers at a flat interface. Due to the short chain lengths, the statistical segment length b in the model had to be slightly changed from the value used in the simulations. Since the chains in a micelle are not allowed to penetrate the core, MC simulations were performed where the core volume was excluded. It was found that the effect could be mimicked by moving the starting point of the chains in the analytical expression to $R' \approx R + aR_g$, where $a \approx 1$ and closely related to the curvature of the anchoring surface. Neglecting the mutual avoidance of the chains can be viewed as polymers dissolved in a θ-solvent, where the polymer-polymer and the polymer-solvent interactions are equal. For large core radii, the conformation of the chains will thus be comparable to the mushroom regime experienced in tethered polymers at a flat interface.

Because of the neglect of the self-avoidance of the chains, it is only possible to make conclusions concerning the influence of the curvature of the grafting surface on the conformation of the chains. The influence of the grafting density and the curvature of the surface on the chain conformation cannot be assessed without the inclusion of chain interactions. *Toral & Chakrabarti* [136] performed MC simulations of polymer chains grafted onto the outer surface of a sphere. The chains were generated as self-avoiding random walk of hard spheres of diameter unity connected by rigid rods starting from the first unimer. The monomers were not allowed to penetrate each other or the grafting sphere. They found that the profiles start to resemble those of a flat interface when the radius of the grafting surface is only about ten times larger than the monomer size, particularly for the moderate surface coverages. Of the more theoretical approaches, Self-Consistent Field (SCF) [39, 83] and Single Chain Mean Field (SCMF) [131] treatments of polymers at a spherical interface have proven to be successful. The dependence of the interaction potential and volume fraction profile of e.g. curvature of the tethering interface, surface density of the chains, and size of the chains have been determined. However, these approaches suffer from the inability of not being able to fit directly to experimental data.

Despite the limitations in the presented model, good agreement was found between the model and small-angle scattering measurements of P85 and PS/PI micelles. However, a slight modification was made for the P85 micelles by inclusion of a PEO shell on the core in the model. For three temperatures in the micellar regime $T = 50$, 55, and 60°C, a q^{-2} behaviour at large q is found, which for long tethered chains would indicate a star-like conformation. However, in light of the short PEO chains the q^{-2} behaviour is not caused by a star-like conformation but is simply due to almost Gaussian behaviour on the surface of the core. The study by *Gast et al.* [39] found a $q^{-1.5}$ scaling behaviour for the comparable micelles composed of 80 units of PS and 65 units of EO.

A significant result is the slight deviation from the model at the highest investigated temperature of 60°C. A likely explanation is the elongation of the micelles into a rod-like shape. This agrees with the expected increasing hydrophobicity of the ethylene oxide, which causes the chains to contract. At higher temperatures it is likely, that the ethylene oxide chains collapse on the surface of the propylene rich core. The values obtained from the model fitting underline the trend; both the aggregation number and the hard-sphere volume fraction increases with temperature. Thus, the micelles are found to grow with temperature, since the ethylene oxide is less swollen and more chains are needed to shield the propylene

oxide from the water. With the less swollen ethylene oxide chains, the Gaussian chain approximation is furthermore invalid. The core has been assumed to consist only of propylene oxide. It has been found by mean field calculations of *Linse et al.* [100], that water seem to be present in the core of the micelle. However, inclusion of water in the core would add an additional parameter to a many parameter model and consequently complicate the interpretation of the data.

The analysis could have been simplified by contrast matching the solution to either the core or the tethered chains. However, the propylene oxide and ethylene oxide has almost similar scattering length density which result in low contrast between the core and the chains when the solvent is contrast matched. For this study, the acquisition time for each experiment would have been too long in order to obtain reasonable statistics on the measurements.

3 Micellar Ordering at the Solid-Liquid Interface

In the previous chapter a model for the P85 micelle was introduced consisting of chains tethered to a spherical interface. We observed that the model was able to reproduce the outcome from bulk SANS measurements. In the present chapter the model is applied to neutron reflectivity measurements in order to describe the surface induced ordering of P85 micelles at the hydrophilic surface of single-crystalline quartz. In contrast to earlier investigations [74, 79, 135], which have focussed primarily on the low concentration regime and the adsorption of unimers, this chapter will primarily treat higher concentrations of P85 in aqueous solution where the aggregation of the triblock copolymers as micelles is predominant. Free-form analysis of the reflectivity data has inspired further modeling and simulations of the micellar ordering. It will be shown that the P85 micelles order like hard spheres at a hard wall. In the following chapter the detailed mathematical framework of the proposed model will be treated: Monte Carlo simulations of hard spheres at a hard wall are performed for a large range of micellar volume fractions and an expression for the projected center distribution of hard spheres is derived. By convoluting the projected center distribution with the projected density of the micelle a function can be obtained for direct fitting of the reflectivity data.

3.1 Neutron Reflectivity

In the last decade neutron reflectometry has been established as a well-suited technique for probing the surface structure of stratified media and "buried" interfaces along the surface normal. Reflectivity gives information on the *scattering length density* of the averaged structure perpendicular to the surface in contrast to other techniques (e.g. ellipsometry), where only the overall thickness and the refractive index are obtained. The large penetration depth for most materials and the large difference in scattering length of hydrogen and deuterium make neutrons ideal for investigations of soft condensed matter. The low absorption of neutrons in, e.g., single crystal quartz and silicon makes it possible to have liquid samples in thermostated enclosures and to study solid-liquid interfaces. The neutrons are able to traverse quartz and silicon crystals and can be reflected from the surface between the crystal and the liquid. One of the limitations in neutron reflectivity measurements is the relatively low neutron flux, which has the consequence that a reasonable flux can only be obtained by relaxing the resolution of the reflectometer. For most samples this is not a serious limitation as the reflectivity curve of, e.g., polymers at a solid-liquid interface show only broad features. It is usually more important that the maximum scattering vectors for which the reflectivity can be measured is limited by the diffuse and incoherent scattering from the sample. This leads to a limitation of the real-space resolution which can be obtained and it also leads to ambiguity in the interpretation of the data. These issues will be dealt with in detail. In the next section the theory of reflection will be discussed. Comprehensive accounts, which are closely related to actual experiments, can be found in *Hamley & Pedersen* [49], *Als-Nielsen* [8], *Lu et al.* [76] and with focus on the applications within polymer science *Russell* [121], *Penfold & Thomas* [108], and *Thomas et al.* [133]. More theoretical accounts are given by *Born & Wolf* [17] and *Lekner* [71].

Advantages of Neutron Reflectometry

Limitations

3.2 Theory

The Refractive Index

Generally, neutrons obey the same relations as electro-magnetic s-waves, and therefore the laws of optics. The motion of the neutron with mass m_n and energy E in a potential V is governed by Schrödingers equation for the wave function Ψ,

$$-\frac{\hbar^2}{2m_n}\nabla^2\Psi + V\Psi = E\Psi. \tag{32}$$

The neutron refractive index, n, can be brought about by transforming the Schrödinger equation into the Helmholtz equation valid for propagation of an electro-magnetic wave [31]:

$$(\nabla^2 + n^2k^2)\Psi = 0. \tag{33}$$

When the two equations (32) and (33) are combined the mean index of refraction n is

$$n = \sqrt{1 - V/E} \approx 1 - V/2E. \tag{34}$$

Since the wavelength of the neutrons are greater than the range of interactions with the nuclei from which they scatter, the potential can be described by an effective point-like Fermi ('pseudo') potential V_f [71]:

Fermi's "Pseudo-Potential"

$$V_f = 4\pi\left(\frac{\hbar^2}{2m_n}\right)b\delta(z), \tag{35}$$

where b is the scattering length unique for every element and $\delta(z)$ is a delta function. For reflection at a surface, it is the local average of the potentials of a collection of neutron scatterers with density N, i.e. the optical potential V, which is of importance. The potential becomes

$$V = 4\pi\left(\frac{\hbar^2}{2m_n}\right)Nb, \tag{36}$$

neglecting the magnetic interaction of the neutron with the magnetic moment of unpaired electrons in the medium. The product Nb is called the scattering length density and is commonly denoted ρ. If *Fermi's* expression for the potential is applied to the refractive index we obtain

General Form of the Refractive Index

$$n = 1 - \frac{\lambda^2}{2\pi}\rho, \tag{37}$$

where λ is the wavelength of the neutron. Usually, the refractive index is written on the form

$$n = 1 - \delta - i\beta, \tag{38}$$

where the extinction coeffient $\beta = \mu\lambda/4\pi = N(\sigma_{\text{inc}}+\sigma_a)$, μ is the linear absorption coefficient, and σ_{inc} and σ_a account for the incoherent scattering and nuclear reactions. The linear absorption coefficient μ is almost negligible for neutrons except for certain materials including cadmium, gadolinium, and samarium.

Reflection from an Interface

Subsequently, we consider the situation, depicted in Figure 16, where neutrons encounter an interface between two uniform media with potentials V_1 and V_2. Thus,

$$V(z) = \begin{cases} V_1 & \text{for } z > 0 \\ V_2 & \text{for } z < 0. \end{cases} \tag{39}$$

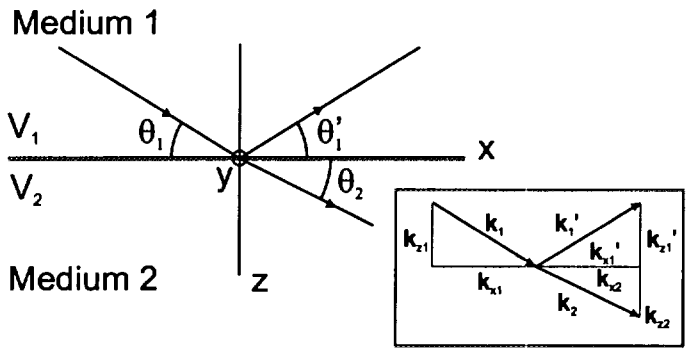

Figure 16. Reflection and transmission of neutrons at an interface.

For neutrons, taken as a plane waves propagating in the zx plane experiencing the varying potential $V(z)$, the neutron wave function Ψ is independent of y and can be separated in the variables z and x in the following way [71]:

$$\Psi(z,x) = \exp(ik_x x)\psi(z). \tag{40}$$

Insertion of $\Psi(z,x)$ in eqn. (32) gives

$$\frac{d^2\psi}{dz^2} + k_z^2\psi = 0, \text{ where } k_z^2(z) = \frac{2m_n}{\hbar^2}[E - V(z)] - k_x^2. \tag{41}$$

The x component of the wave vector $k_x = k_{x1} = k'_{x1} = k_{x2}$ is conserved in either medium. From Figure 16 we arrive at the laws for reflection and refraction:

$$k_1\cos(\theta_1) = k_1\cos(\theta'_1) \tag{42}$$

$$k_1\cos(\theta_1) = k_2\cos(\theta_2) \qquad \textit{Snell's law}, \tag{43}$$

where

$$k_i^2 = k_x^2 + k_{zi}^2 = \frac{2m_n}{\hbar^2}(E - V_i),\ i = 1,2. \tag{44}$$

Snell's law can be rewritten as *Snell's Law*

$$n_1\cos(\theta_1) = n_2\cos(\theta_2). \tag{45}$$

Whenever $\theta_1 < \theta_c$, where θ_c is called the critical angle, $\cos(\theta_1) > n_2/n_1$, and eqn. (45) has no real solution for θ_2. Hence, the neutron beam is said to be totally reflected. In this case, it can be shown [71], that the wave vector in the medium 2 becomes imaginary, and the neutron beam is thus an exponentially damped field in the medium.

The solution to eqn. (41) in each of the two media can be written as

$$\psi = \begin{cases} \exp(ik_{z1}z) + r\exp(-ik_{z1}z) & \text{for } z < 0 \\ t\exp(ik_{z2}z) & \text{for } z > 0. \end{cases} \tag{46}$$

Here, r and t are defined as the reflection and transmission amplitude, respectively. Continuity of ψ and $d\psi/dz$ at $z = 0$ requires, that *Fresnel Laws*

$$r = \frac{k_{z1} - k_{z2}}{k_{z1} + k_{z2}}, \quad \text{and} \quad t = \frac{2k_{z1}}{k_{z1} + k_{z2}}, \tag{47}$$

which are known as the *Fresnel laws.*

When an additional interface is added to the system (denoted medium 2) *multiple scattering* occurs between interface 0-1 and 1-2 (see Figure 17). The reflection *Multiple Scattering*

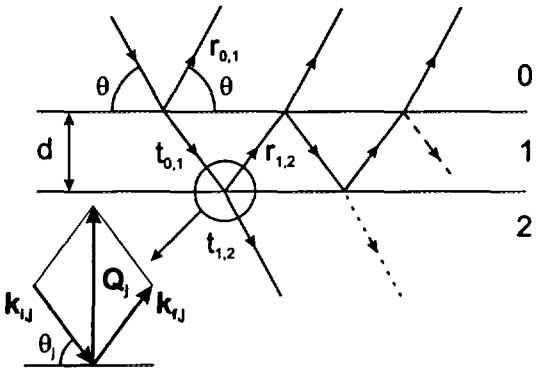

Figure 17. Multiple scattering in a stratified medium.

amplitude r becomes a power series in the phase difference between the two interfaces, ϕ, and summation of the series yields [17, 49]

$$r = \frac{r_{0,1} + r_{1,2}\exp(-i\phi)}{1 + r_{0,1}r_{1,2}\exp(-i\phi)}, \tag{48}$$

where $r_{i,j}$ is the amplitude for reflection between medium i and j and can be calculated from eqn. (47). *Parratt* [102] generalized this formulation to include an arbitrary number of layers. The reflectance was written as a recursion formula similar to eqn. (48),

Parratt's Formalism

$$r'_{j-1,j} = \frac{r_{j-1,j} + r_{j,j+1}\exp(-i\phi)}{1 + r_{j-1,j}r_{j,j+1}\exp(-i\phi)}, \tag{49}$$

where $\phi = Q_j d_j$, d_j is the thickness of layer j and $Q_j = |\vec{k_{f,j}} - \vec{k_{i,j}}| = 2k\sin\theta_j$ (cf. Figure 17) the length of the scattering vector for layer j, which is related to the length of the scattering vector in vacuum, Q, by Snell's law,

$$Q_j = \sqrt{Q^2 - 16\pi(Nb)_j} = \sqrt{Q^2 - (Q_j^c)^2}. \tag{50}$$

Here, $Q = 2k\sin\theta$ and $Q_j^c = 2k\sin\theta_j^c$ is the critical scattering vector below which total reflection occurs. The reflection amplitudes are calculated recursively from the substrate assuming that the substrate ($j = N$) does not give rise to any reflections, i.e. $r_{N,N+1} = 0$. The reflectivity, which is the ratio between the reflected and the incident intensity, is calculated as $R(Q) = r'_{0,1}r'^{*}_{0,1}$. Since any arbitrary profile can be approximated by a number of layers with constant scattering length density, it is thus possible to perform a full dynamical calculation of the reflectivity of an arbitrary shaped surface profile.

An alternative formulation for the calculation of the reflection from a stratified medium is the *Matrix formalism* [17], which has proven to be useful for bilayered structures as we shall see in Chapter 6.

Matrix Formalism

A full dynamical calculation is often time consuming and useful approximations have emerged [49] to overcome this problem. The widely used *kinematical approximation* provides a way to achieve physical insight relating the derivative of the scattering length density $\rho(z)$, by a Fourier transform to the reflectivity by the *master formula* [7, 11]:

Kinematical Approximation

$$R = R_F(Q)\left|\frac{1}{\rho_\infty}\int\frac{d\rho}{dz}\exp(-iQ'z)dz\right|^2, \tag{51}$$

where ρ_∞ is the scattering length density of the subphase and $R_F(Q)$ the (*Fresnel*) reflectivity from a sharp planar interface given by

$$R_F(Q) = \left|\frac{Q - Q'}{Q + Q'}\right|^2. \tag{52}$$

Above Q' is the refraction corrected scattering vector, $Q' = \sqrt{Q - (Q_\infty^c)^2}$. In this approximation multiple scattering is neglected and it is therefore ideally suited for e.g. self-assembled monolayers at the liquid-vapour interface [7, 10, 11, 52]. The formula is valid for $Q \gg Q_c$. However, to avoid approximations full dynamical calculations are performed wherever possible throughout the work described in the present thesis.

3.3 Experimental Section

The Reflectometer TAS8

Experimental Set-up

All the experiments were performed at the neutron reflectometer TAS8 at the reactor DR3, Risø National Laboratory (see e.g. ref.'s [18, 41]). In the experimental set-up the wavelength, λ (typically 4.6-4.8 Å), of the neutrons is selected by the (002) reflection of pyrolytic graphite (PG) with a mosaic spread of $\eta_{\text{mon}} = 0.5°$, which gives a Full-Width-at-Half-Maximum bandwidth of $\Delta\lambda/\lambda = \eta_{\text{mon}}/\tan\theta_{\text{mon}} \approx 1$ %, where θ_{mon} is the angle of incidence of the neutrons on the monochromator crystal. The higher order neutrons are removed from the beam by a beryllium filter. The monochromatized neutrons are collimated by a set of vertical double slits up- and downstream of the sample. To reduce the background a horizontal slit with an aperture of 30 mm is placed between each set of double slits. The set-up is depicted in Figure 18.

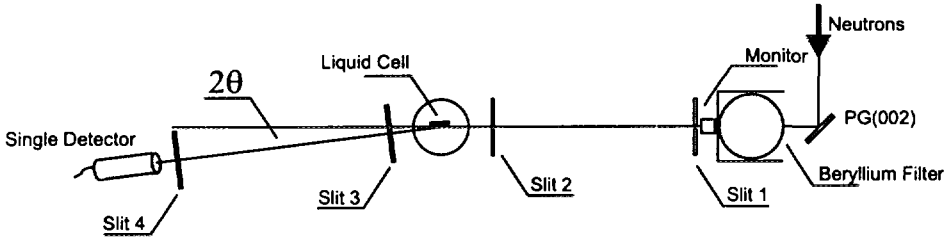

Figure 18. A schematic drawing of the reflectometer TAS8 at the heavy water moderated reactor DR3, Risø National Laboratory.

The scattering vector, $\mathbf{Q}$, is defined as $\mathbf{Q} = \mathbf{k}_f - \mathbf{k}_i$, $|k_i| = |k_f| = 2\pi/\lambda$, where $\mathbf{k}_i$ and $\mathbf{k}_f$ are the incident and final wave vector, respectively. As the scattering vector is along the surface normal, which is referred to as the z direction, information is obtained for the scattering length density profile $\rho(z)$. The reflectivity curve is obtained by measuring the intensity as the scattering vector is varied in the direction along the surface normal. To allow for higher flux at the sample position four settings of the slits with equal size apertures are used during an experiment, i.e. the slits are opened symmetrically for the footprint to match the sample area. At TAS8 one can at best obtain six orders of magnitude in a reflectivity curve and typically go to 0.1 Å^{-1}. For the symmetric double slit setting the obtained full-width-at-half-maximum (FWHM) of Q is [18]

Aperture of the Slits

Q-Resolution

$$\Delta Q = \sqrt{(\frac{4\pi}{\lambda}\frac{w}{L})^2 + (Q\frac{\Delta\lambda}{\lambda})^2}, \tag{53}$$

where L is the distance from the first to the last slit and w the width of the aperture, which is the same for all the slits. Typically, $w = 0.5$ mm, $L = 1600$ mm, $\lambda = 4.75$ Å, and at $Q = 0.01$ Å^{-1} a resolution of $\Delta Q/Q = 0.083$ is obtained. Due to wide slit settings, the sample does not intersect the whole width of the beam at low angles close to the critical edge. Hence, the measured intensity is corrected for the geometrical factors [42], known as the foot-print correction, to

Geometrical Corrections

adjust for the lower incident flux at low angles. At higher angles, each setting of the apertures of the slits ensures that the foot-print of the beam on the sample is less than the length of the sample in order to to avoid the (simple) corrections of the measured intensity.

Materials

Quartz Single-Crystal

For the experiments a quartz single-crystal with dimensions $50 \times 10 \times 100$ mm^3 was supplied by Gooch and Housego Ltd.. Initially, the two large faces of the crystal were polished to $\lambda/10$ and better than $\lambda/2$ on the rest of the faces.

P85

The triblock copolymer P85 was a gift from BASF Corp., Wyandotte, USA, and is commercially available. It was used without further purification. For all the samples the triblock copolymer was dissolved in D_2O at 5°C, where it forms a homogeneous solution. D_2O is chosen to reduce the contribution from the incoherent scattering of hydrogen, i.e. the background from the solvent, and to increase the contrast between micelles and solvent.

Cleaning Procedure

The exact chemical and physical properties of the surface are important for the result of the experiment. To ensure a perfectly clean surface a three-step procedure, adapted from *Field et al.* [33, 34], for cleaning the quartz crystal was applied. Initially, the crystal was cleaned in analytical grade ethanol/methanol followed by a Millipore (resistivity ρ_R = 18.2 MΩcm) water rinse. The crystal went through two acid baths, first a mixture of 3:1 HCl : HNO_3 and subsequently a 3:1 mixture of H_2SO_4: HNO_3, each time for 4-6 hours. After the acid baths the crystal was rinsed once again in Millipore water, analytical grade ethanol and methanol, and finally Millipore water. The crystal was left to dry in a vacuum oven at 50°C before the cell was assembled.

The Solid-Liquid Cell

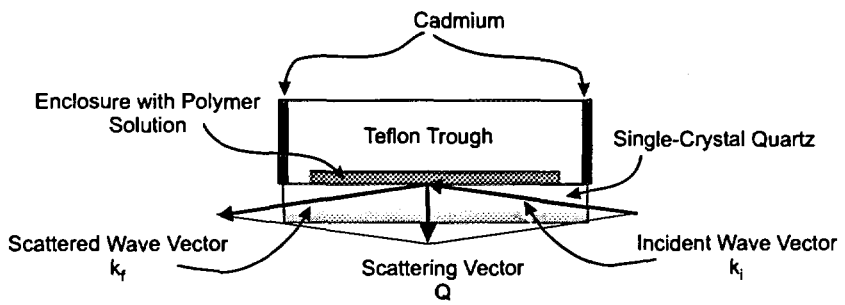

Figure 19. The cell used for the solid-liquid measurements. The neutrons traverse the quartz crystal, are reflected from the solid-liquid interface, and are finally detected after traversing the crystal once again.

The cell used for the reflectivity measurement under static conditions of the fluid is depicted in Figure 19 and will be denoted "the static cell". This type of cell has become standard for investigations of adsorption at the solid-liquid interface [33, 85, 116]. The incoming neutrons enter through the smallest face of the quartz single crystal, traverse through the quartz crystal, reflect off the quartz-solution interface and are thereafter detected. Single crystal quartz is virtually transparent to neutrons and more than 60 % is transmitted through 100 mm of single crystal

quartz in a wavelength range of 1 Å $< \lambda <$ 6 Å [116]. In reflectivity the angle of incidence is typically below 3°, thus refraction effects at the air-quartz interface can be considered to be negligible due to the almost normal incidence of the neutrons. Hence, no correction of the scattering vector, Q, is necessary. The use of quartz instead of silicon has the advantage that air bubbles in the liquid can be detected by eye. The liquid is kept in a 5 or 15 ml Teflon cell with a small inlet and outlet hole in the top and bottom of the back of the cell, respectively. Teflon is chosen because it is chemically inert and easy to clean. Furthermore, a third outlet hole in the top of the cell removes air from the sample chamber when the cell is being filled. For temperature measurements, a Platinum resistance thermometer (Pt-100) has been placed in close vicinity of the sample chamber in the Teflon cell. The quartz crystal and the Teflon cell are kept in a thermostated enclosure connected to a heat bath and can be controlled within 0.3°C. Two thin sheets of cadmium are attached to the side of the cell. They prevent the neutrons from entering the side of the Teflon cell giving rise to background. In addition, the cadmium pieces adsorb the neutrons reflected from the liquid-Teflon interface at the backside of the cell.

3.4 Reflectivity Results

The Quartz Crystal Surface

X-ray Reflectivity

To ensure that the crystal showed no sign of contaminants on the surface after the acid treatment, the X-ray reflectivity of the freshly cleaned quartz crystal in air was recorded. The scattering length density for X-rays is equal to the electron density ρ_e times the free electron radius r_e (Thomson radius). The Fresnel reflectivity can be written on the form [49, 133]

$$R_F(Q) = \left[\frac{Q - \sqrt{Q^2 - Q_c^2}}{Q + \sqrt{Q^2 - Q_c^2}}\right]^2 \times \exp(-Q^2\sigma_{\text{surf}}^2), \tag{54}$$

where $Q_c = \sqrt{16\pi\rho_e r_e}$ for X-rays and $Q_c = \sqrt{16\pi\rho}$ for neutrons, where ρ is the scattering length density. The exponential term takes into account the root-mean-square roughness of the surface, σ_{surf}, and is an approximate form of the factor introduced by *Nevot & Croce* [99]. In the fitting, the resolution of the experiment was taken into account by convolution with a Gaussian shaped resolution function with the standard deviation given by $\sigma_{\text{res}} = \Delta Q/2\sqrt{2\ln 2}$ (cf. eqn. 53 and ref. [18]). The result revealed a surface roughness of $\sigma_{\text{surf}} = 4.5 \pm 0.2$ Å and a scattering length density of $\rho^X_{\text{quartz}} = (2.27 \pm 0.02) \times 10^{-5}$ Å^{-2}, which is in good agreement with the value calculated from the structural parameters [140]: $\rho^X_{\text{quartz}} = 2.24 \times 10^{-5}$ Å^{-2}. A 17 Å thick water layer as stated by *Cosgrove et al.* [24] could not be identified in the present measurements.

Neutron Reflectivity

Before each run, a neutron reflectivity scan of the quartz/D_2O interface was performed before the polymer solution was injected into the cell. In this way both the purity of the solvent and the cleanliness of the surface were checked. A good estimate of the surface roughness requires reflectivity measurements at up to several times the critical scattering vector. With neutrons, the limited range of scattering vectors available make estimation of the roughness more uncertain. The values obtained for single-crystal quartz assuming a pure solvent was typically $\rho^N_{\text{quartz}} = (4.15 \pm 0.04) \times 10^{-6}$ Å^{-2} and $\sigma_{\text{surf}} = 9 \pm 3$ Å. The former value is in agreement with the theoretical value of $\rho_{\text{quartz}} = 4.17 \times 10^{-6}$ Å^{-2} for single crystalline quartz.

Micellar Ordering at the Solid-Liquid Interface

In the experiment, the solution of P85 in D_2O is injected into static cell at $T \approx 10°C$, where the triblock copolymers are unimers in solution. When the temperature is raised above 10°C, a large increase in the reflectivity occurs when the polymers start to aggregate into micelles. From rocking scans (ω) it is evident that a large part of the total scattering is due to diffuse scattering on which the specularly reflected neutrons are superimposed. Figure 20 shows a reflectivity curve of 15 wt % P85 in D_2O at a temperature of 50°C. The insert shows a rocking (ω) curve taken at $Q_z = 0.0276$ Å^{-1}, where the subscript z marks the direction normal to the surface. Evident is the large contribution from diffuse scattering to the total scattering.

Large Diffuse Component of the Scattering

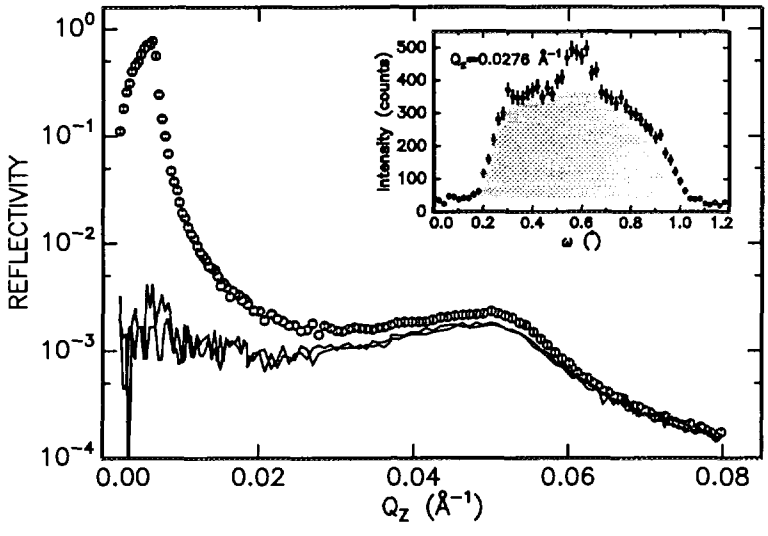

Figure 20. The raw data from a reflectivity scan of 15 wt % solution of P85 at 50° C. The solid lines show the background measured at $\theta \pm 3\Delta\theta_{sp}$. The insert shows the result of a rocking curve at $Q_z = 0.0276$ Å^{-1}. The specular peak is located at 0.6° on top of the broad diffuse peak (grey-shaded) which arises mainly from scattering from the micellar liquid.

Separation of the Bulk and the Surface Signal

In a reflection measurement, several contributions to the measured signal can be identified (see Figure 21). The specular reflected neutrons are superimposed on a background from diffuse scattering arising from the surface roughness and neutrons scattered from the bulk of the sample. The latter is either due to incoherent scattering from e.g. hydrogen or small-angle scattering from the molecules or aggregates in the solution. As pointed out by *Thomas* [133] the choice of D_2O to obtain high contrast between P85 and the solvent for the reflection measurements leads to considerable small angle scattering which, due to the dimensions of the aggregates, will scatter in the same region as the reflectivity measurements.

Contributions to the Measured Intensity

To obtain the intensity of the neutrons reflected specularly from the interface between the polymer solution and the quartz crystal, the diffuse scattering has to be properly subtracted. Hence, two points at $\omega = \theta \pm \Delta\theta$ were measured. The width of the bulk related ring of scattering is much larger than the typical width of the specular peak. Therefore, it is reasonable to perform a linear interpolation between the points and subtract it from the specular signal. The increment, $\Delta\theta$, is chosen to be approximately $3\Delta\theta_{sp}$ from the center of the specular peak, where $\Delta\theta_{sp}$ is

Background Subtraction Procedure

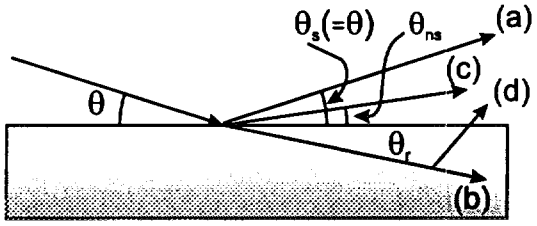

Figure 21. When the neutron beam encounters the solid-liquid interface, it is either specularly reflected (a), refracted (b), or non-specularly reflected (diffuse) (c). The refracted neutrons can furthermore be scattered by the molecules or aggregates in the bulk solution (d).

the FWHM of a Gaussian fit to the specular peak. Figure 20 depicts in addition to the reflectivity scan, the two background scans recorded at $\omega = \theta \pm 3\Delta\theta_{sp}$. It is apparent that the specular peak is indistinguishable from the diffuse background for scattering vectors larger than 0.07 $Å^{-1}$, which has the drawback of limiting the resolution in real space. The real space resolution is approximately determined by $1.5/Q_{max}$, where Q_{max} is the maximum scattering vector (see Appendix A). With $Q_{max} = 0.065$ Å the resolution is about 23 Å.

SANS Recordings of the Background. In order to investigate the separation of the surface signal from the bulk signal, the cell was mounted on the Risø SANS instrument [41]. The specularly reflected beam and the bulk small-angle scattering were recorded by varying the angle of incidence. The signal was recorded in two dimensions for each angle by a position-sensitive detector. A characteristic broad ring of scattering was observed from the bulk (see Figure 22), whereas the specularly reflected beam moved across the ring as the angle was varied.

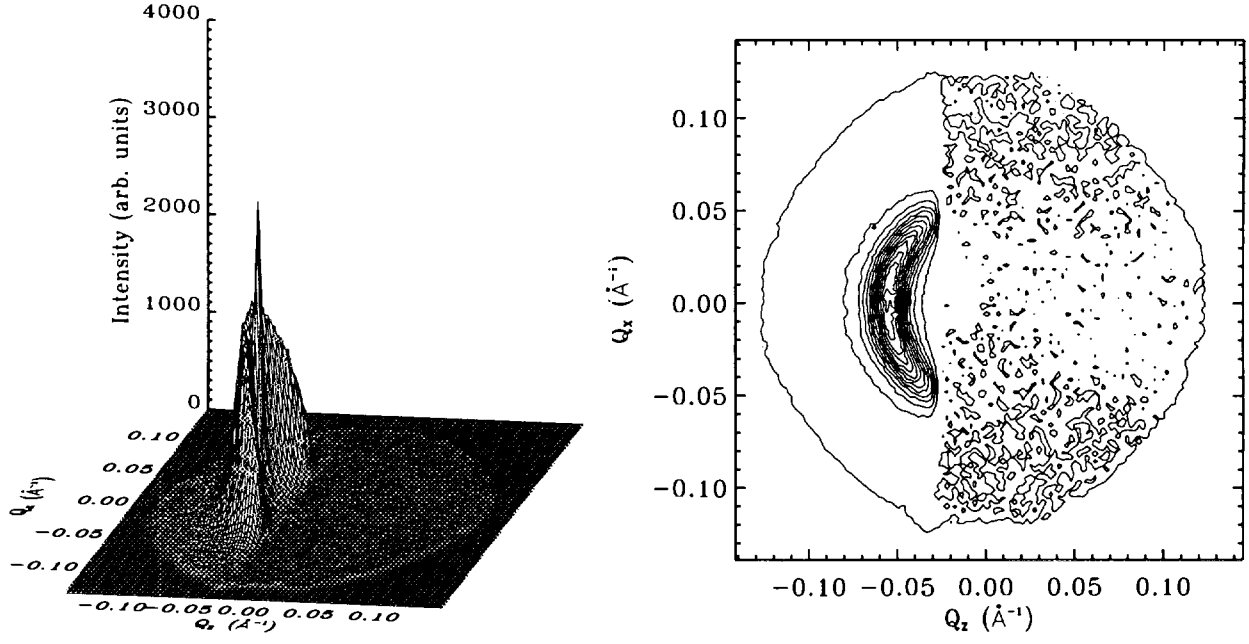

Figure 22. Intensity in the direction perpendicular to the surface from a 25 % wt solution of P85 in D_2O recorded at the Risø SANS instrument with an incidence angle of 1.05°. The scattering is only seen at negative Q_z values due to the fact, that the transmitted beam is absorbed by the cadmium on the sides of the Teflon cell. The sharp peak is the specularly reflected neutrons.

Scattering from Micelles

The scattering intensity of the micelles in the bulk can be described by the product of the micellar form factor and the structure factor, which describes the interference effects, as seen in chapter 2. The form factor is monotonically decreasing with increasing scattering vector. The structure factor has an oscillation at low scattering vectors and a peak at about $2\pi/d$, where d is the minimum intermicellar distance. At higher scattering vectors the structure factor is constant and the product of the form factor and structure factor gives a correlation ring of scattering centered at $Q_z = 0.04 - 0.06$ Å^{-1} depending on the temperature [94].

Achieving a Measure for the Reflectivity

The intensity in the direction of the surface normal ($Q_x = 0$) is shown in Figure 23 for three different incident angles 0.60°,1.05°, and 1.35°. The specular peak is apparent on the figures as a small shoulder on the broad peak, which is due to the micelles in the bulk. The bulk scattering was fitted by the intensity expression obtained for micelles with hard-sphere interactions [94], whereas a Gaussian function was used as a model for the specular peak. Even though the sample volume, which the neutrons in transmission see, becomes greater for large scattering vectors, the specular peak is independent of the volume change, because it arises from reflection from the solid-liquid interface. Thus the amplitude of the Gaussian line shape can be used as a measure for the reflectivity.

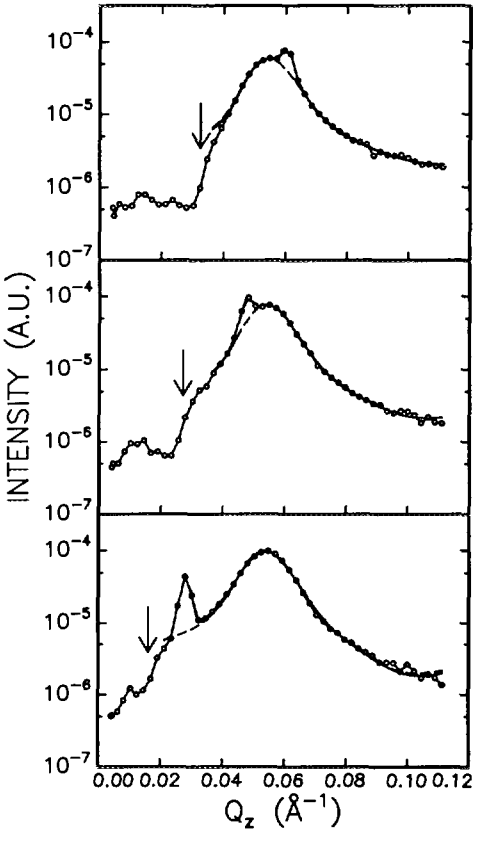

Figure 23. The intensity in the direction of the surface normal ($Q_x = 0$) is shown for three different angles of incidence 0.60° (bottom), 1.05°, and 1.35° (top), respectively. The movement of the specular peak is apparent in the figure. The solid line is the fit to a hard-sphere model and a Gaussian peak and the dashed line is the simple hard-sphere model. The arrows indicate the point where to the cadmium on the Teflon cell absorbs the neutrons.

Comparison of Reflectivities from TAS8 and SANS

In order to check the validity of the two-point subtraction of the background a comparison of the SANS and TAS8 reflectivity curves (see Figure 24) was performed and showed good agreement.

Range of Experiments

Reflectivity scans for 15, 20, and 25 % wt of P85 in aqueous solution (D_2O) were performed in a temperature range between 30 to 60°C. The range of temperatures are all in the spherical micellar phase according to the phase diagram determined by *Mortensen & Pedersen* [94] and *Glatter et al.* [44]. Examples of scans are shown

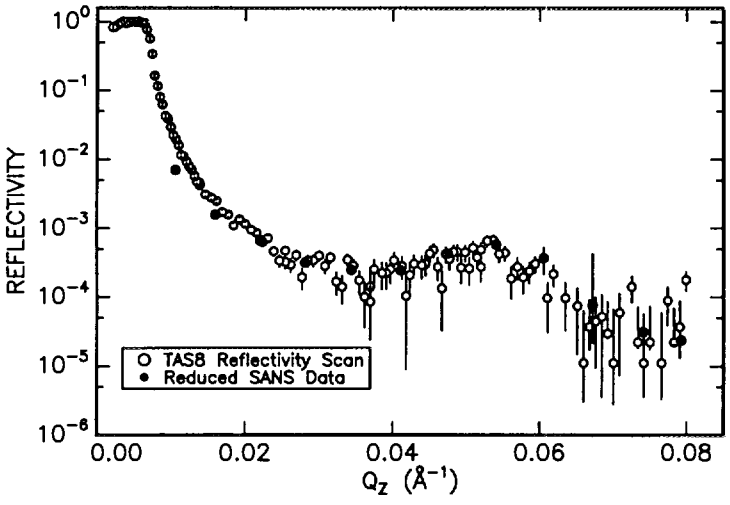

Figure 24. Reflectivity curve from a 25 % wt solution of P85 in D_2O. The figure also shows the comparison between the reflectivity curve obtained on the TAS8 reflectometer and on the SANS instrument by two different approaches for subtracting the diffuse scattering originating from the bulk and background.

in section 3.7 in connection with the analysis (see e.g. Figures 27 and 28).

3.5 Data Analysis

Critical Edge

A distinct feature in the reflectivity scans is the critical scattering vector, Q_c, of total external reflection, which provides information on the overall contrast $\Delta\rho_{\text{bulk}}$ (i.e. the difference in scattering length density) between the incident medium, ρ_{quartz}, and the bulk solution, ρ_{sol}, given by the relation $Q_c = \sqrt{16\pi\Delta\rho_{\text{bulk}}}$. Unfortunately, the critical edge appears at a very shallow angle and is influenced by the relatively poor resolution of the spectrometer. Furthermore, the reflectivity often has to be foot-print corrected, and Q_c is easily affected by systematic errors such as a slight bending of the quartz crystal. The scattering length density of the polymer solution, ρ_{sol}, can be calculated from

$$\rho_{\text{sol}} = \frac{\rho_{\text{P85}} + \rho_{\text{D}_2\text{O}} V_{\text{D}_2\text{O}}/V_{\text{P85}}}{1 + V_{\text{D}_2\text{O}}/V_{\text{P85}}}, \tag{55}$$

where V_i and ρ_i, i=P85 or D_2O is the volume and the scattering length density of material i, respectively. The ratio of the volumes can be related to the mass fraction w_p of the copolymer in the solvent by

$$\frac{V_{\text{D}_2\text{O}}}{V_{\text{P85}}} = \left[\frac{1}{w_p} - 1\right] \frac{\rho^m_{\text{P85}}}{\rho^m_{\text{D}_2\text{O}}}, \tag{56}$$

where ρ_i^m is the mass density of material i, respectively. We can calculate the total scattering length of P85, ρ_{P85}, from its constituents ethylene oxide and propylene oxide by $b_{\text{P85}} = 50b_{\text{EO}} + 40b_{\text{PO}}$, where b denotes the scattering length. Finally, the scattering length densities can be found from

$$\rho_i = \frac{\rho_i^m N_A b_i}{M_i^{mol}}, \; i = \text{EO, PO, P85} \tag{57}$$

where N_A is Avogadro's number, ρ_i^m, M_i^{mol}, and b_i is the mass fraction, the molar mass and the scattering length of material i, respectively. Table 2 contains the parameters at a temperature of 50°C.

i	ρ_i^m (g/cm^3)	M_i^{mol} (g/mole)	b_i (10^{-5}Å)	ρ_i (10^{-6}Å^{-2})
EO	1.182	44.053	4.139	0.669
PO	1.01	58.080	3.316	0.346
P85 (dry)	1.011	4500	339.6	0.459
D_2O	1.0957	20.031	19.14	6.306

Table 2. The physical data of the constituents of P85 at 50° C.

Concentration Dependence of The Critical Scattering Vector

Table 3 gives the values for the different mass fractions at a temperature of 50°C.

wt %	V_{D_2O}/V_{P85}	ρ_{sol} (10^{-6}Å^{-2})	$\Delta\rho_{bulk} = \rho_{sol} - \rho_{quartz}$ (10^{-6}Å^{-2})	Q_c (Å^{-1})
15	5.23	5.37	1.25	0.0079
20	3.69	5.06	0.94	0.0069
25	2.77	4.75	0.64	0.0057

Table 3. The calculated critical scattering vectors using the parameters in Table 2.

The critical scattering vectors for all the measurements were determined and are shown in the Table 4.

wt %	T (°C)	ρ_c (10^{-6}Å^{-2})	Q_c (Å^{-1})	Q_{calc} (Å^{-1})
15	50	1.20	0.0076	0.0079 (-4.5%)
20	50	0.740	0.0061	0.0069 (-11.3%)
25	49	0.748	0.0061	0.0057 (8.5%)

Table 4. Comparison between the measured and calculated critical scattering vectors. The values in parenthesis of the last column is the deviation in percent.

The seemingly large deviation in percent between the calculated and measured critical edges can be related to several factors. Firstly, the resolution $\Delta Q/Q$ of the experiment becomes increasingly poor close to $Q_z = 0$. Secondly, the dimensions of the crystal makes it possible to encounter optical effects such as focusing or defocusing of the neutron beam. Alignment was performed according to the procedure suggested by *Bouwman et al.* [19] to avoid pit-falls in the alignment of the low resolution neutron reflectometer. Furthermore, rocking curves taken just below and above the critical scattering vector were checked for any traces of crystal bending. The procedure should ensure a perfect alignment. It is uncertain how an undetectable bending of the crystal would affect the determination of the critical scattering vector. However, the reflectivity features for the investigated micellar structures occur at scattering vectors larger than five times the critical scattering vector, where a small displacement does not introduce significant errors in the data.

Free-Form Determination of the Surface Profile

In the investigated micellar liquid region the specular scattering solely gives rise to a broad peak (between 0.3 and 0.6 Å^{-2}) with respect to the usual Fresnel behaviour as seen in Figure 20. Further examples are given in connection with the data analysis (see Figures 25, 27 and 28). The peak shape and position are found

to depend on the temperature and concentration. As the temperature increases and concentration decreases, the peak moves towards lower Q values indicative of larger structures. It is difficult to obtain any direct knowledge of the ordering on the surface from the reflectivity data. Hence, the reflectivity measurements were analyzed using one step free-form determination of the surface profiles [106] in order to obtain real-space information on the structure. The free-form method provides scattering length density profiles without prior knowledge of the system, and thus gives a guide to suitable functional models. The solutions are unbiased and therefore not restricted to a functional form of the scattering density profile. However, *Sivia et al.* [125] found in their maximum entropy approach that a good fit to the reflectivity data could be obtained which had no resemblance with the real scattering length density profile. These authors found, that a good estimate of the overall thickness of the sample and a demand for a positive scattering length density profile could produce a reasonable fit to the test profile. This method does not eliminate the fast oscillations in the profile (ringing) which occur due to the limited range of momentum transfers.

Maximum Entropy Approach

A more efficient method for free-form determination of scattering length density profile has been introduced by *Pedersen & Hamley* [106]. The scattering length density $\rho(z)$ is expanded in a series of N cubic b splines:

One Step Free-Form Determination of the Surface Profiles

$$\rho(z) = \sum_{j=1}^{N} a_j B_j(z), \tag{58}$$

where a_j are the coefficients to be determined and $B_j(z)$ the cubic b-splines [103]. A non-linear least-squares method (Marquardt-Levenberg) is used for minimizing χ^2 given by

$$\chi^2 = \frac{1}{M-N} \sum_{i=1}^{M} [R(Q_i)_{exp} - R(Q_i)]^2/\sigma_i^2, \tag{59}$$

where $R(Q_i)_{exp}$ is the measured reflectivity with standard deviations calculated from the Poisson statistics of the measured intensities, $R(Q_i)$ the reflectivity calculated from $\rho(z)$ using dynamical theory [102], and M the number of measured points. To overcome the problem of slow convergence and solutions with large oscillatory behaviour, two constraints on $\rho(z)$ are included in the minimization. These are described by two functions

$$A_1 = \sum_{n=1}^{N-1} (a_{n+1} - a_n)^2 + w_1 a_1^2 \tag{60}$$

and

$$A_2 = \sum_{n=1}^{N-1} (a_n - a_{av})^2, \; a_{av} = (1/6)\rho_{av}, \tag{61}$$

which measure the smoothness of the solution and bias the solution towards the expected average scattering length density, respectively. They can be transformed into a general constraint,

$$N_c = [(1-w)A_1(N+3) + w\frac{150A_2}{N+3}]M, \tag{62}$$

which effectively changes the function to be minimized to $\chi^2 + \lambda N_c$, where λ is a Lagrangian multiplier. The optimum value of λ is found via a discrepancy criterion using the mean-square residual $MSR = \chi^2/M$.

With the inclusion of the constraints in the determination of the scattering length density profiles it is difficult to obtain the standard errors with standard

Uncertainty of the Free-Form Profiles

methods such as the propagation of errors [16]. However, a rough estimate can be obtained from purely statistical considerations [141]. The reflectivity R can for $Q \gg Q_c$ (kinematical approximation) be expressed as

$$R \propto \frac{\rho^2}{Q^4}. \tag{63}$$

where ρ is the scattering length density. The standard deviation of R is denoted by σ_R and accordingly for ρ. From the accumulation of errors of independent variables one has

$$\frac{\sigma_R}{R} = 2\frac{\sigma_\rho}{\rho}. \tag{64}$$

Thus, the relative error on ρ is half the relative error on the measured reflectivity. In the above expression the σ_Q term is negligible and has been omitted. It is the high Q values, which has the largest error and thus determine the error on ρ. Typically, $\sigma_R/R = 8$ %, and consequently σ_ρ/ρ=4%.

Another method for estimating the uncertainty on the ρ profiles is to analyse several data sets generated randomly from an original profile [130]. The data points of a generated reflectivity curve is obtained from a Gaussian distribution with center and the standard deviation of the original data point. The obtained ρ profiles can then be averaged and the uncertainty determined. An example is given for the reflectivity curve of 20 wt % solution of P85 in Appendix A.

Interpretation of the Profiles

The ρ profiles all show a damped oscillating variation with different periodicities dependent on the concentration and temperature. Examples of the scattering length density determined by the free-form method are shown in Figure 25 for three concentrations 15, 20, and 25 wt % at 50°C. The maximum of ρ for each profile occurs close to the surface of the crystal and has a value slightly less than the scattering length density of water, ρ_{D_2O}. A P85 micelle consist of a mainly propylene oxide core with a corona of tethered tails of ethylene oxide. Consequently, the scattering length density ρ_c of the core is approximately 0.34×10^{-6}Å^{-2}, which is much less than that of the surrounding solvent, $\rho_{D_2O} = 6.4 \times 10^{-6}$Å^{-2}. Caution should be taken in the quantitative analysis from the free-form profiles due to the fact that both the periodicity and maximum of the scattering length density is influenced by truncation effects, i.e. the limited range of scattering vectors [141]. In Appendix A a detailed discussion is given concerning the truncation effects for the present profiles. However, the effects are minor when the reflectivity data is measured beyond the broad peak. A micellar layer will exclude D_2O, which has a larger scattering length density, and thus give rise to a local minimum in the scattering length density profile. A disordered layer will have interpenetration of water, which decreases the amplitude of the corresponding oscillation in the profile. Hence, the damping of the oscillations is a result of the disordering of the layers away from the surface of the crystal. The bulk micellar liquid has random positions of the centers of the micelles with respect to the surface of the crystal, and therefore does the scattering length density profile only reflect the average scattering length density of the micelles. The tentative model is depicted in Figure 26, where the correspondence between the density profile and micellar layering is indicated.

Micellar Ordering at the Quartz Surface

Several other systems have shown the same oscillatory form of the scattering length density at a surface; e.g. the smectic surface ordering seen in the isotropic phase of nCB liquid crystals [9], the ordering of microemulsions $C_{10}E_4$-D_2O-octane and C_8E_3-H_2O-decane at the air-liquid [141] and solid-liquid [68, 69] interfaces,

Systems Showing Same Oscillatory ρ Profiles

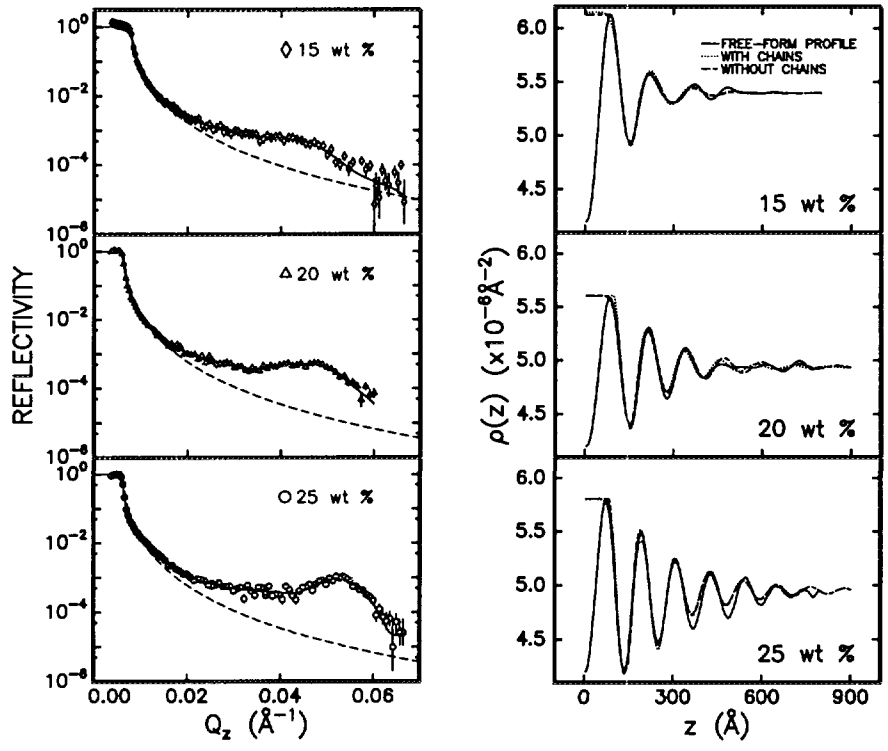

(a) Reflectivity Profiles

(b) Corresponding ρ Profiles

Figure 25. (a): The reflectivity scans, corrected for diffuse scattering, background and geometrical factors, of 15, 20, and 25 % wt P85 in aqueous solution (D_2O) at 50° C. The solid line is the free-form fit to the data. (b): The corresponding free-form scattering length density profiles. The dashed and dotted lines are the fits to the free-form ρ profiles of the micellar model with and without chains tethered to the solid core, respectively. The discrepancy between the fit and the free-form profile at the leading edge is due to a neglect of the roughness of the quartz crystal in the model calculations. Notice the inability for either model to fit the 25 wt % free-form ρ profile.

respectively, and even at the liquid-vapour interface of the metals (Sn [78] and Ga [114]). Several different approaches have been applied to quantify the surface profiles. Ginzburg-Landau theory reveals a decaying sinusoidal form of the density profile [9, 69]. Here, the order parameter ψ is related to the density of a component in the system e.g. the local concentration difference between water and oil inside the microemulsion. However, the damped sinusoidal form with a single period is often not sufficient to model the ordering. For the liquid metals, two more elaborate parameterizations have been applied. The first is obtained by treating the liquid-vapour interface as a truncated solid where the root-mean-square displacement amplitude of the atoms from their lattice positions diverges with increasing distance from the surface. In the second model an error-function density profile is superimposed by a periodic distortion occurring at the average position of the atoms perpendicular to the surface. However convenient for the physical interpretation of the reflectivity data, the above mentioned approaches all suffer from being parameterizations which do not relate directly to the physical system.

Ginzburg-Landay Theory

Truncated Solid Approach

A micellar ordering has been suggested for the adsorption of the ionic surfactant

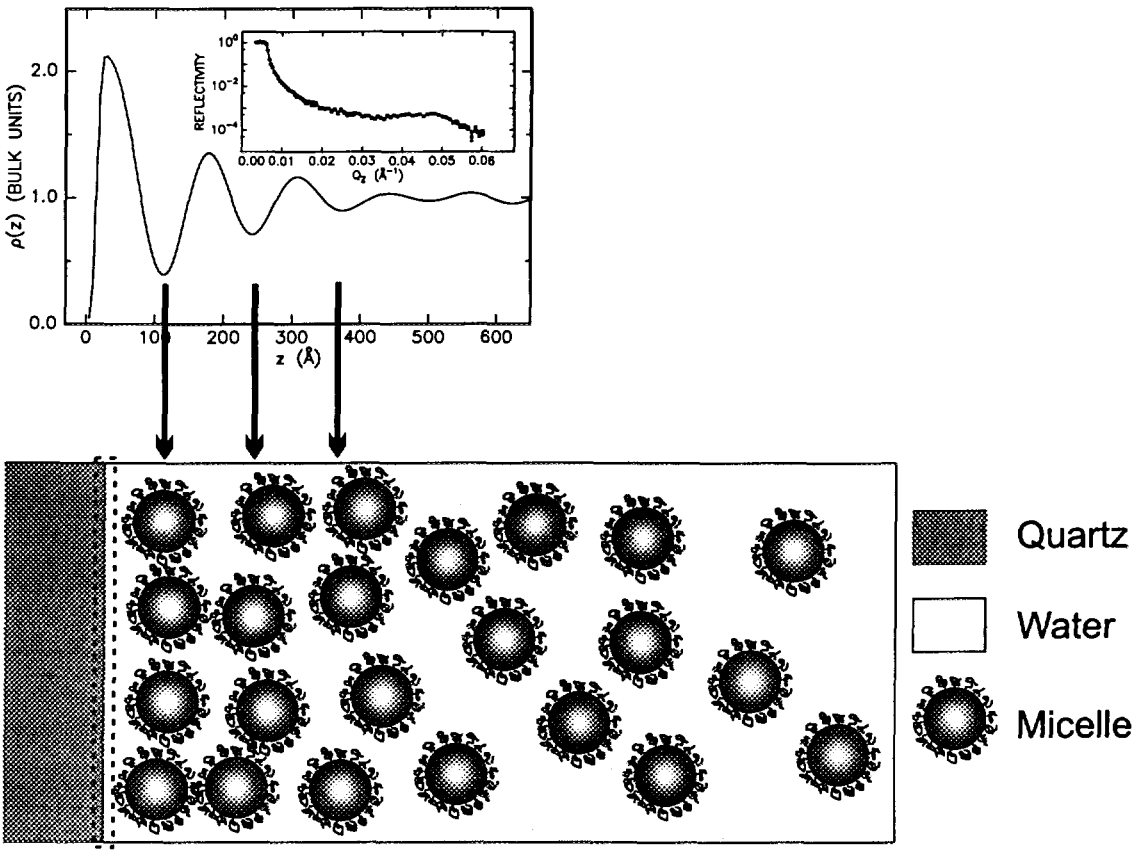

Figure 26. The scattering length density profile obtained by a free-form approach to the reflectivity data of 20 % wt P85 at 50° C from TAS8. The insert shows the reflectivity curve with the free-form fit shown as the solid line. The lower part of the figure shows the tentative model. Each minimum in the scattering length density profile corresponds to the position of a micellar layer as indicated by the arrows. The first peak in the profile is due to a water layer at the surface. The dashed box indicates the area which due to experimental resolution is difficult to assess.

tetradecyltrimethylammonium bromide (C_{14}TAB) above the critical micelle concentration at the air/solution interface by *Lu et al.* [77]. These authors suggested a connection to hard sphere ordering at a hard wall [45, 127]. The latter system display oscillations in the density of the hard spheres at the surface. *Groot et al.* [45] found from Monte Carlo simulations that the oscillations were caused by limited diffusion normal to the surface. The hard spheres are hindered in their motion from the bulk to the innermost layers and result in quasi two-dimensional layers of the hard spheres. The present results show large oscillations in the scattering length density profile and it is expected that the hard sphere ordering at the hard wall applies to the P85/D_2O-system. Therefore, the hard-sphere ordering close to a hard wall has been determined systematically. The simulations are briefly described in the next section and the modeling in detail in the next chapter.

Hard Sphere Ordering at a Hard Wall

3.6 Micellar Model: Simulations and Projection

On the basis of the tentative model a scheme was set up for calculating the scattering length density profile based on Monte Carlo (MC) simulations. A thousand hard spheres were confined between two hard walls located at $z = 0$ and $z = L_z$ with periodic boundary conditions in the x and y direction. It was possible to

obtain an expression for the distribution of the hard spheres from the MC simulations using numerical interpolation. Note, that this expression describes the center distribution of the micelles.

To account for the actual shape of the micelle the center distribution was convoluted with the density of the micelle projected onto the normal to the walls. The micelle structure was approximated in two ways: First, the micelles were described as solid spheres and secondly, as solid spheres with Gaussian chains attached to the surface. It was shown in Chapter 2, that Gaussian chains attached to a solid sphere is a valid representation of the P85 micelle. The core radius of the micelle, which contains the propylene oxide, is denoted R and the hard-sphere interaction radius R_{HS}.

In the case of solid spheres with tethered Gaussian chains the normalised scattering length density of the micelle, $\rho_{\mathrm{mic}}^{\mathrm{norm}}$, is the weighted sum of the normalised scattering length density of the solid sphere, ρ_s^{norm}, and the chains, ρ_t^{norm}. The solid sphere and the chains are weighted by the volume and the scattering length density of EO and PO with respect to the incident medium in the following way:

Normalised Projected Scattering Length Density of the Micelle

$$\rho_{\mathrm{mic}}^{\mathrm{norm}}(z,R) = \frac{\rho_t^{\mathrm{norm}}(z,R)\Delta\rho_{\mathrm{EO}}v_{\mathrm{PEO}}^{tot}(R) + \rho_s^{\mathrm{norm}}(z,R)\Delta\rho_{\mathrm{PO}}v_{\mathrm{PPO}}^{tot}(R)}{\Delta\rho_{\mathrm{EO}}v_{\mathrm{PEO}}^{tot}(R) + \Delta\rho_{\mathrm{PO}}v_{\mathrm{PPO}}^{tot}(R)}, \quad (65)$$

where $\Delta\rho_{\mathrm{EO}}$, $\Delta\rho_{\mathrm{PO}}$, v_{PEO}^{tot}, and v_{PPO}^{tot} are the scattering length density difference between the EO or PO chains and the incident medium and the total volume of EO or PO in a micelle with $N_{agg} = 4\pi R^3/3V_{\mathrm{PPO}}$ block copolymers, respectively, V_{PPO} being the volume of an propylene oxide block. Because the scattering length density of the tails, ρ_t^{norm}, and the solid spheres, ρ_s^{norm}, are normalised to unity, it can easily been seen that the total density of the micelles, $\rho_{\mathrm{mic}}^{\mathrm{norm}}$, likewise will be normalised to unity. The final expression for the micellar ordering on the surface is a convolution of $\rho_{\mathrm{mic}}^{\mathrm{norm}}$ with the density of the hard spheres, ρ_{HS}, obtained from the simulations:

Final Expression of the Micellar Model

$$\rho_m(z) = \Delta\rho_{\mathrm{fluid}} - (\Delta\rho_{\mathrm{fluid}} - 1)\int_{-\infty}^{+\infty} \rho_{\mathrm{mic}}^{\mathrm{norm}}(x)\rho_{HS}((z-z_0)-x)dx \quad (66)$$

where $\rho_m = \rho_m(z, \rho_{\mathrm{fluid}}, R, R_{HS}/R, \eta, z_0)$, $\rho_{\mathrm{mic}}^{\mathrm{norm}} = \rho_{\mathrm{mic}}^{\mathrm{norm}}(x,R)$, $\rho_{HS} = \rho_{HS}((z-z_0)-x, R, R_{HS}/R, \eta)$, and $\Delta\rho_{\mathrm{fluid}}$ is the scattering length density of the fluid closest to the quartz surface, R the radius of the core of the micelles, R_{HS} the hard-sphere interaction radius, z_0 an arbitrary zero point, and η the hard-sphere volume fraction. Hence, the model has five free parameters to be determined.

The constant, $\Delta\rho_{\mathrm{fluid}}$, and the prefactor, $\Delta\rho_{\mathrm{fluid}} - 1$, arise from the fact that the micelles are dispersed in a solvent. The prefactor of the convolution integral has the form $\Delta\rho_{\mathrm{fluid}} - 1$, because at low z values the total density of the micelles, ρ_m, is assumed to tend to $\Delta\rho_{\mathrm{fluid}}$ and at large z values to unity. Note, that the $\rho_m(z)$ is normalised to the bulk density, and $\Delta\rho_{\mathrm{fluid}}$ is in units of the bulk density. When fitting the reflectivity curves, the offset z_0 has been replaced with $3\sigma_{\mathrm{surf}}$, where σ_{surf} is the standard deviation used in the error function which has been chosen to describe the quartz-liquid interface. When the micelles are modeled as solid spheres, we simply use $\rho_{\mathrm{mic}}^{\mathrm{norm}} = \rho_s^{\mathrm{norm}}$ in the convolution integral. In the subsequent chapter a detailed discussion of the simulations and the derivation of the final expression for the scattering length density profile can be found.

3.7 Modeling Results

Figure 27 shows scans, corrected for diffuse scattering, background and geometrical factors [42], of 15 % wt at a temperature of 40°C, 50°C, and 60°C, while Figure 28 compares three different concentrations, 15, 20 and 25 wt % at a temperature of

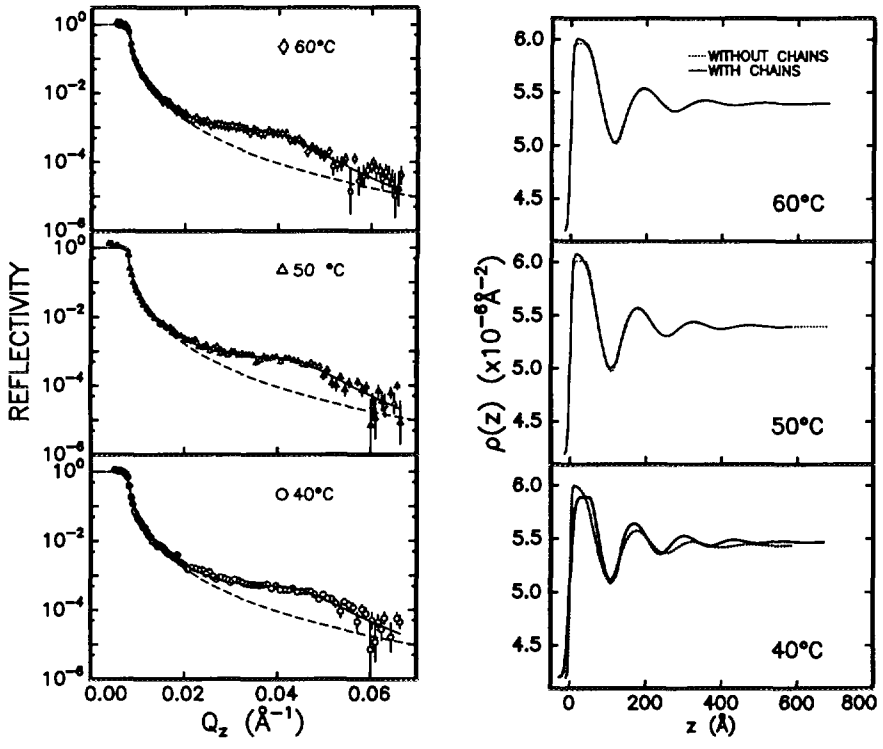

(a) Reflectivity Profiles

(b) Corresponding ρ Profiles

Figure 27. (a): The reflectivity scans, corrected for diffuse scattering and background and geometrical factors, of 15 % wt P85 in aqueous solution (D_2O) at 40° C, 50° C, and 60° C. The solid lines are fits obtained from the solid sphere with tethered chains model of the micelle. The dashed lines represent the theoretical form of the Fresnel reflectivity expected from a infinitely sharp interface with the bulk scattering length density of the P85 solution. (b): The corresponding scattering length density profiles obtained from the two models .

50°C. Also shown are the model fits to the reflectivity data and the corresponding ρ profiles which will be discussed below.

Model Fits to the Free-form ρ profiles

Initially, non-linear least-squares fits were performed to the free-form profiles and the resulting values are listed in Tables 5 and 6 for the pure solid sphere and the solid sphere with tethered chains, respectively. Figure 25 shows the results of the free-form analysis for three concentrations 15, 20, and 25 wt % at $T = 50°C$ and the corresponding profiles. Also shown are the model fits to the free-form ρ profiles.

The values from the fits to the free-form ρ profiles serve as input parameters for optimization of the model parameters by a non-linear least-squares fit directly to the reflectivity data calculated from dynamical theory and smeared with instrumental resolution. In the direct fitting the leading edge of the scattering length density profile was modeled by an error function of width σ_{surf}. The values for the best fits are listed in Table 8 for the solid sphere and in Table 7 for the solid sphere with tethered chains. Two series of data are shown in Figures 27 and 28 for constant temperature ($T = 50°C$) and constant concentration (15 wt %), respectively.

The Uncertainty on R and R_{HS}

The values of the core radius R have large errors arising from the fact that R

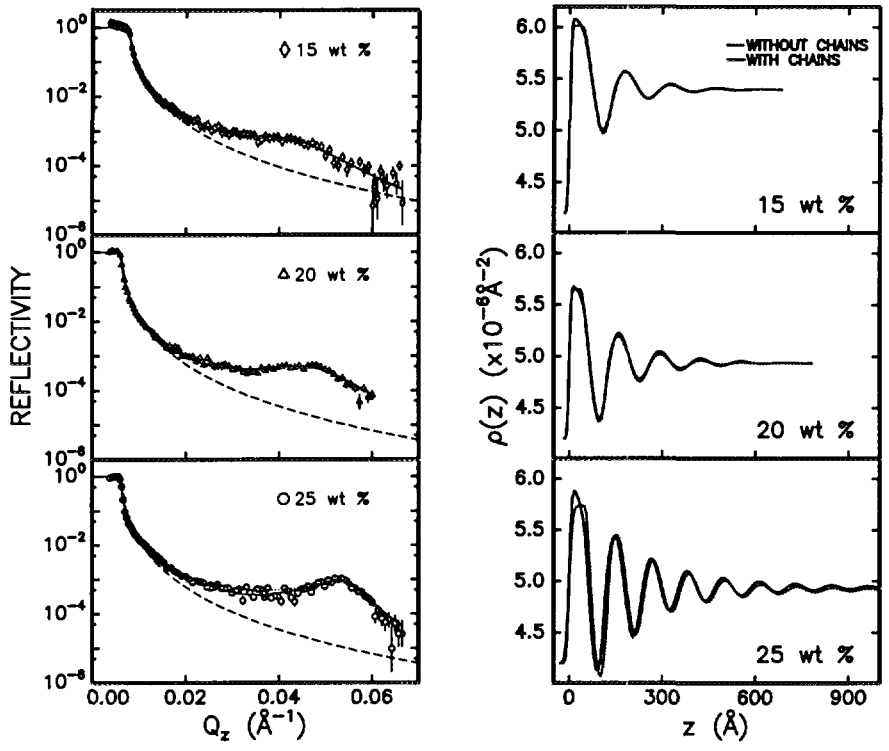

(a) Reflectivity Profiles

(b) Corresponding ρ Profiles

Figure 28. (a): The reflectivity scans, corrected for diffuse scattering and background and geometrical factors, of 15, 20 and 25 % wt P85 in aqueous solution (D_2O) at 50° C. The solid lines are the hard-sphere model fits to the data. For 15 % and 20 wt % the fits to the reflectivity data are indistinguishable for the two models (see text), thus only one curve is shown. Notice the inability of the model to fit the pronounced peak of the 25 % wt reflectivity data indicating a possible pre-crystallization at the surface of the quartz crystal. The inability is more pronounced from the solid sphere with tethered chains. The dashed lines represent the theoretical form of the Fresnel reflectivity expected from a infinitely sharp interface with the bulk scattering length density of the P85 solution. (b): The corresponding scattering length density profiles obtained for the solid sphere and solid sphere with tethered chains models of the micelle.

enters the calculation through a convolution. Since the hard-sphere interaction radius R_{HS} is linked to R in the model, as it enters the model through R_{HS}/R, it will also have a large error associated with in. However, in Appendix A it is shown that the actual error on R_{HS} is considerably less than the fitting procedure estimate. Therefore, the uncertainty is not shown in Figure 29b.

Systematic Variation of The Model Parameters with Temperature and Concentration

The parameters in Tables 8 and 7 vary systematically with temperature and concentration. Figure 29 shows the variation of the core radius R, the hard-sphere radius R_{HS}, and the hard-sphere volume fraction η with temperature for the 15 and 20 wt % solutions. In accordance with earlier SANS measurements [94] the hard-sphere volume fraction η increases with concentration and attains an almost constant value ($\eta = 0.31$ at 15 wt % and $\eta = 0.39$ at 20 wt %) with temperature. Furthermore, the hard-sphere radius R_{HS} increases with temperature regardless of which of the two micelle representations are used. An increase in concentra-

wt%	T (°C)	ρ_{fluid} (10^{-6}Å^{-2})	N_{agg}	R (Å)	R_{HS} (Å)	η	R_c^{bulk} (Å)	$R_{\text{HS}}^{\text{bulk}}$ (Å)
15	30	6.09	83	42	66	0.27	45	71
	40	6.08	63	39	66	0.27	50	77
	50	6.13	88	43	70	0.30	53	81
	60	6.04	118	48	78	0.28	-	-
20	40	5.89	73	41	61	0.40	49	74
	50	5.61	80	42	64	0.41	52	78
25	49	5.81	81	42	63	0.47	51	76
	61	5.95	111	47	65	0.36	-	-
-	-	±0.1	-	±1	±1	-	-	-

Table 5. The results from fitting the free-form scattering length densities with the hard-sphere center distribution convoluted with the projected density of a solid sphere. The bottom line indicates the average value of the uncertainty obtained from the fitting procedure. The omitted errors are less than the last digit in the tabulated values.

wt %	T (°C)	ρ_{fluid} (10^{-6}Å^{-2})	N_{agg}	R (Å)	R_{HS} (Å)	η
15	30	6.09	38	59	70	0.31
	40	6.14	34	41	71	0.28
	50	6.15	39	65	70	0.34
	60	6.03	41	73	77	0.33
20	40	5.89	32	36	61	0.43
	50	5.61	36	50	69	0.44
25	49	5.81	32	35	63	0.47
	61	5.95	40	72	69	0.40
-	-	±0.1	-	±1	±1	-

Table 6. The results from fitting the free-form scattering length densities with the hard-sphere center distribution convoluted with the projected density of a solid sphere with Gaussian chains tethered to the surface. The bottom line indicates the average value of the uncertainty obtained from the fitting procedure. The omitted errors are less than the last digit in tabulated numbers.

tion appears to decrease R_{HS}. However, the core radius R, hence the aggregation number $N_{\text{agg}} = \frac{4}{3}\pi R^3/V_{\text{PPO}}$ where V_{PPO} is the volume of poly(propylene oxide) in each block copolymer, seems to increase with temperature, however, with the current uncertainty this dependency is only suggestive. It would be in agreement with the SANS findings. The values of R and R_{HS} for the solid spheres agree

wt%	T (°C)	ρ_{fluid} (10^{-6}Å^{-2})	N_{agg}	R (Å)	R_{HS} (Å)	η	σ_{surf} (Å)	ϕ_{surf}^{P85} (Å)	R_c^{bulk} (Å)	$R_{\text{HS}}^{\text{bulk}}$ (Å)
15	30	5.89±0.24	70	40±9	66±5	0.37±0.03	9±2	0.072	45	71
	40	5.91±0.15	74	41±12	71±7	0.32±0.03	5±3	0.070	50	77
	50	6.01±0.38	97	45±14	71±7	0.31±0.02	5±2	0.053	53	81
	60	5.96±0.14	121	48±15	78±8	0.29±0.03	5±3	0.061	-	-
20	40	5.87±0.15	76	41±5	64±4	0.39±0.02	5±1	0.065	49	74
	50	5.65±0.18	76	41±2	67±3	0.35±0.02	5±1	0.105	52	78
25	49	5.7±0.2	60	38±3	63±2	0.49±0.01	11±1	0.11	51	76
	61	5.6±0.2	70	42±4	72±5	0.46±0.01	13±3	0.13	-	-

Table 7. The results from fitting the reflectivity data densities with the hard-sphere center distribution convoluted with the projected density of a solid sphere.

wt %	T (°C)	ρ_{fluid} (10^{-6}Å^{-2})	N_{agg}	R (Å)	R_{HS} (Å)	η	σ_{surf} (Å)	$\phi_{\text{surf}}^{\text{P85}}$	$R+2R_g$ (Å)
15	30	6.01±0.14	61	38±9	67±5	0.34±0.04	5±3	0.054	60
	40	6.01±0.20	80	42±4	73±3	0.32±0.03	3±1	0.054	63
	50	6.09±0.15	73	41±7	72±4	0.33±0.03	5±2	0.042	62
	60	6.01±0.14	73	41±6	78±3	0.31±0.02	5±2	0.054	62
20	40	5.94±0.28	36	32±8	64±5	0.40±0.02	5±3	0.065	53
	50	5.7±0.3	50	36±13	68±8	0.39±0.02	5±3	0.11	57
25	49	5.9±0.3	40	33*	64±2	0.47±0.01	6±2	0.08	55
25	61	5.7±0.3	40	33*	73*	0.43*	6*	0.11	55

Table 8. The results from fitting the reflectivity data densities with the hard-sphere center distribution convoluted with the projected density of a solid sphere with Gaussian chains tethered to the surface. The errors are obtained from the fitting procedure. An asterisk denotes a fixed parameter.

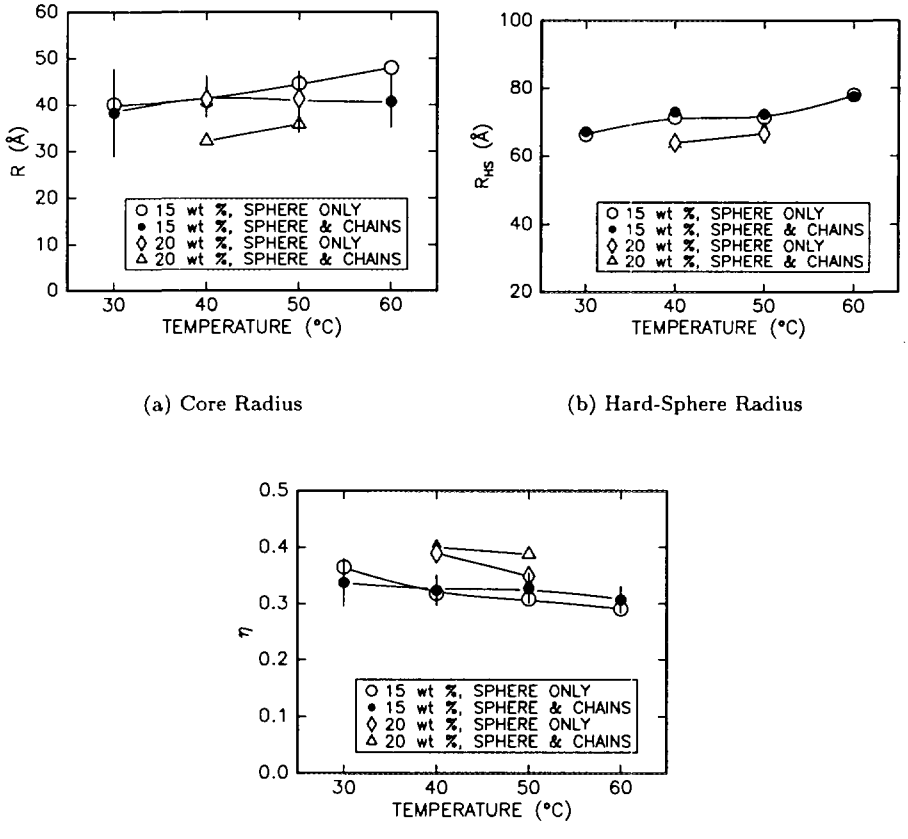

(a) Core Radius

(b) Hard-Sphere Radius

(c) Hard-Sphere Volume Fraction

Figure 29. Trends from the model-fitting.

within the errors with bulk values [94]. However, there appear to be a tendency for the surface radii to be smaller than the corresponding bulk values (see Table 7).

Effect of the Tethered Chains

The results of the analysis seem to indicate that the inclusion of the tethered chains gives rise to a decrease in the core radius of the micelles, R. This change is

expected as the solid sphere model must incorporate the less dense chains in its radial extent. For the solid spheres *with* tethered chains, the difference between R_{HS} and R is a measure of the influence of the chains on the micellar interaction. Since the volume of the PEO chain is approximately $V_c = 4\pi R_g^3/3$ at the surface of the core, where R_g is the radius of gyration of the PEO block, the tethered chains will contribute with roughly $2R_g$ to the hard-sphere interaction radius of the micelle. The SANS analysis in Chapter 2 showed that this assumption is valid when the PEO chains are excluded from the volume of the PPO core. In the present micelle model the radius of gyration of PEO is kept constant at 10.8 Å. From Table 8 the two measures, $R+2R_g$ and R_{HS}, agree within 10 Å (14 %), R_{HS} being the largest. Consequently, the PEO chains appear to be extended into the solution, which is likely to be caused by excluded volume interactions between the PEO chains and the PEO chain itself. Excluded volume effectively extends the polymer chains and the steric interactions are likely to result in a more brushlike chain conformation.

The Roughness at the Solid-Liquid Interface

The last parameter in the model is the roughness at solid-liquid interface, σ_{surf}. The values obtained is 5 ± 2 Å, which is below the resolution of the experiment and can thus only be related to the general form of the initial peak and not the true surface roughness.

Volume Fraction of P85 at the Surface

Tables 7 and 8 gives the volume fraction of P85, ϕ_{surf}^{P85}, at the surface, which is calculated from $\rho_{fluid} = (1 - \phi_{surf}^{P85})\rho_{D_2O} + \phi_{surf}^{P85}\rho_{P85}$. Evidently, the values are reduced to less than approximately 50 % of the bulk values ($V_{P85}/(V_{P85}+V_{D_2O}) \approx 0.16$ for 15 wt % and $V_{P85}/(V_{P85}+V_{D_2O}) \approx 0.21$ for 20 wt %). The same result is obtained if it is assumed that only EO is present close to the surface. This indicates a possible depletion layer close to surface of the quartz crystal.

Depletion Layer

Discrepancy Between the Model and the 25 wt % Solution

According to Figures 27 and 28 the model is in excellent agreement with the experimental reflectivity curves for 15, 20 wt %, whereas a larger discrepancy is found at 25 wt %. The discrepancy of the 25 wt % solution becomes larger with temperature. In particular, the solid spheres with tethered chains cannot reproduce the large amplitudes in the ρ profile, which are necessary in order to obtain the more pronounced peak in the reflectivity data. This point is clearly elucidated when a model fit to the free-form ρ profile of 25 wt % at 61°C is attempted (see Figure 30).

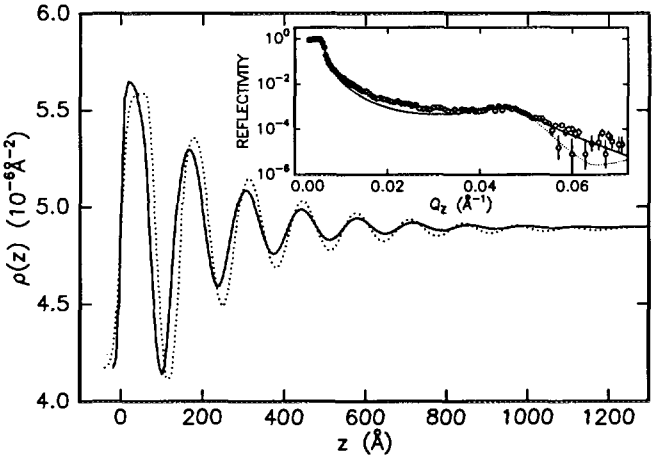

Figure 30. The best fits to the 61° C scan of 25 wt % P85 in solution. Evident is the inability to reproduce the features of the reflectivity curve. The dotted curve is without tethered chains and the full curve is with the tethered chains to the solid sphere.

The free-form profile of 25 wt % at 49 °C depicted in Figure 25 shows, that the amplitude of model oscillations decay too rapidly compared to the free-form profile. The slight inability of the model to reproduce the amplitudes at 25 wt %, which is on the border of the body-centered micellar region, can suggest an even stronger pre-crystallization than the model is able to describe. From SANS measurements of P85 solutions in Couette geometry it has been shown that the polycrystallites can be transformed into a single crystal by application of shear [88]. Therefore, shear flow reflectivity measurements (see Chapter 5) in Pouseuille geometry was performed.

Shear Study of the Micellar 25 wt % Solution.

The objective of this study was to investigate whether shear would induce a transition to a single-crystal assuming that poly-crystallites of cubic ordering is present in the solution at 25 wt %. Thereby, it was hoped that an increased surface ordering would be seen. The cell used for the experiments is described in detail in Chapter 5. Figure 31 shows the comparison between static run at $T = 44°C$ and two different shear rates at an average flow rate of 27 mm/s and 111 mm/s.

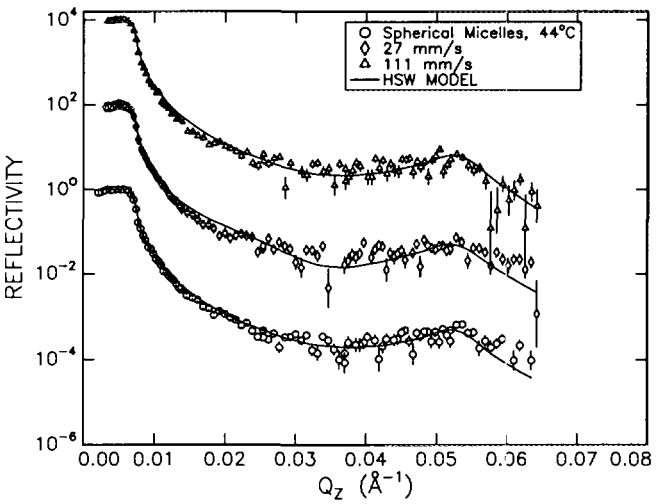

Figure 31. The best model fits to the reflectivity curves obtained for static and flow conditions at $T = 44°C$ scans of 25 wt % P85 in solution.

No significant differences are observed in reflectivity curves in response to the shear field. SANS measurements [88] have shown, that the transformation to a single crystal of a solution containing cubic poly-crystallites happens instantaneously at any shear rate. Consequently, the 25 wt % solution does not contain poly-crystallites or it does not have a high enough volume fraction of crystallites to align macroscopically. Figure 32 shows the obtained scattering length densities of the micellar model (solid spheres with or without tethered chains) for the static and the shear reflectivity curves. It is evident, that even though a reasonable fit was obtained for the static curve, no good agreement could be obtained for the shear curves both with and without tethered chains. This result appears to indicate some change in the micellar structure with shear. Due to the poor statistics of the data it is beyond the data to suggest an elongation of the micelles or other forms of disorder in the static micellar ordering. The parameter values from the model fitting are listed in Table 9.

Model Fitting to the Shear Data

No Change in Response to Shear

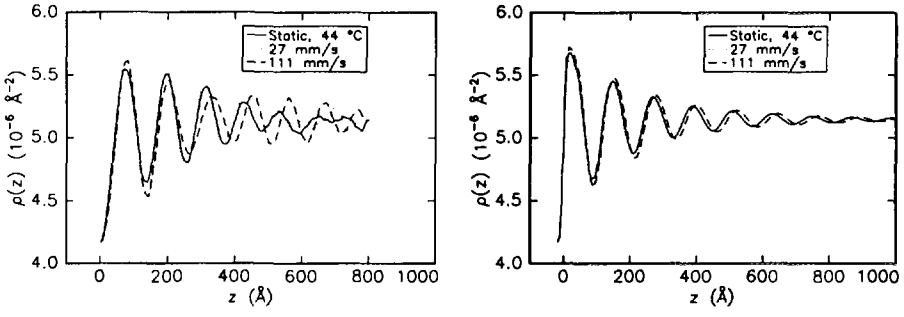

(a) Free-Form ρ profiles

(b) The sphere & chains ρ profiles

Figure 32. Results analysis of the shear measurements of a 25 wt % P85 solution at a temperature of 44° C.

Avg. Flow Rate (mm/s)	ρ_{fluid} (10^{-6}Å^{-2})	N_{agg}	R (Å)	R_{HS} (Å)	η	σ_{surf} (Å)
w/o chains						
0	5.7*	77	42±3	67±4	0.48±0.02	5*
27	5.6*	25	29±6	67±2	0.48±0.04	3*
111	5.6*	34	31±2	66±3	0.48±0.03	8*
w/chains						
0	5.7*	51	36±4	66±4	0.48±0.04	6±3
27	5.6*	50	36±3	68±4	0.48±0.02	6±2
111	5.6*	30	30±4	66±3	0.48±0.02	5±2

Table 9. The results from fitting the reflectivity data from the sheared solution with and without the Gaussian chains tethered to the solid sphere in the model. An Asterisk denote a fixed parameter.

3.8 Discussion

The surface induced ordering of P85 micelles at the hydrophilic surface of quartz has been successfully modeled by the density of hard spheres at a hard wall convoluted by the projected density of a solid sphere with or without tethered Gaussian chains. The density of the hard spheres at a hard wall was obtained by parameterizing a series of Monte Carlo simulations as a function of the hard-sphere volume fraction η. The model for the micelle was inspired by earlier bulk analysis of P85 micelles in solution; the solid sphere was used by *Mortensen & Pedersen* [94] and Chapter 2 described the solid sphere with tethered chains as a useful model of the micelle. A limitation of this model is the neglect of polydispersity, which in Chapter 2 was shown to be quite large ($\sigma(N_{\text{agg}})/N_{\text{agg}} = 0.4$). This might influence the determination of the hard-sphere interaction radius, R_{HS}, and the micellar or core radius, R. However, the limited region of scattering vectors in the reflectivity measurements makes it problematic to include another parameter to the existing five parameters in the model. In addition, the tethered chains has a single value of the radius of gyration in the model fixed at a reasonable estimate. Another key assumption, the hard sphere interaction of the micelles, will be justified in the next chapter.

A large contribution to the reflected neutrons arises from micellar bulk scattering and has to be subtracted to arrive at the true surface related signal. This signal can not be separated from the background at scattering vectors larger than

0.065 $Å^{-1}$, which in effect reduces the real space resolution to about 23 Å (see Appendix A). The large background signal from the bulk is an inherent property of high concentration solutions and cannot be avoided. Fortunately, it has been shown that the truncation is only crucial if the reflectivity data is truncated below the broad peak in the data (see Appendix A and ref. [141]). The relatively low resolution of the experiment does pose problems in e.g. determination of a low valued roughness at the solid-liquid interface.

Excellent agreement was obtained between the 15 and 20 wt % data and both micellar models. Hence, it strongly supports the assumption that discrete aggregates are formed close to the surface of quartz and not e.g. a lamellar structure. Moreover, the free-form method ensures that the achilles heel of reflectivity, the ambiguous scattering length density profile, is resolved since no recurrence of a second *physically acceptable* profile was found in the analysis. The parameters of the model were determined by two different approaches: Either the model was fitted to the free-form scattering length density profile or directly to the reflectivity data. The values obtained from the two approaches differ insignificantly, however the reflectivity fitting was biased as the free-form values were typically used as initial parameters.

Close to the boundary of the bulk micellar crystallization at 25 wt % the inability of the model to reproduce the amplitudes of the ρ profile can suggest an even stronger pre-crystallization than the model is able to describe. Another possibility is surface ordering of disordered micellar bulk cubic polycrystallites. From SANS measurements of P85 it has been shown that the polycrystallites can be transformed into a single crystal by application of shear. However, shear flow reflectivity measurements showed no abrupt changes or additional peaks in the reflectivity profile with shear indicative of the formation of a single crystal. Consequently, there is no indication of a crystallite formation for the 25 wt % solution.

The analysis showed that a water rich layer exists closest to the surface of quartz. From the parameter, ρ_{fluid}, which signifies the scattering length density of the fluid closest to the quartz crystal, the corresponding volume fraction of P85 or EO was less than 50 % of the bulk value. This result indicates a possible depletion layer close to the surface of quartz. The formation of a depletion layer has previously been seen in a molecular dynamics study of the aggregation of amphiphilic molecules in an oil-water-surfactant system [126]. The origin of this layer was suggested to be due to short range repulsion, a solvation force, between the micelles and the monolayer of surfactant at the oil-water interface. Opposing these ideas are the findings of *Cosgrove et al.* [24] and *Field et al.* [33, 34] who both reported a water layer inherently bound to the surface of quartz. Below the critical micelle temperature, triblock copolymers adsorb in low amounts on quartz and are unsaturated at the surface, thus only giving rise to a thin adsorbed layer of approximately 20 Å [63, 79]. Mean Field theory with the inclusion of two conformations of the -OCCO- segments (see Introduction) found that PEO is present closest to the hydrophilic quartz surface and extending into the solution with PO most abundant in the middle part of the adsorbed layer [75]. An adsorbed layer may be repulsive and give rise to a thin water layer as observed. However, a repulsive layer would imply a dense layer at the surface thinner than it would be possible to discern with the present resolution.

From these findings it seems clear that the hydrophobic PPO part of the triblock copolymer determines the surface structure and aggregation, which are thus governed by same interplay between entropy and enthalpy as seen for the bulk solution. In order for an increased amount of PEO to adsorb to the surface and thus increasing the enthalpic term of the free energy, the adsorption has to be accompanied by an entropic gain from desorption of solvent from the surface or

by creating a less dense layer of polymer on the surface. However, PPO is sufficiently hydrophobic to prevent EO from adsorbing in the micellar regime and thus exposing the PPO chains to a more water rich environment at the surface. It is primarily micelles which are formed in the solution and thus only the remaining "free" triblock copolymers (which is present in a concentration equal to the critical micelle concentration) which are likely to adsorb. The water rich inner layer implies that the micelles do not adsorb directly to the surface. *Wijmans et al.* [139] found from simulations of amphiphilic diblock copolymer micelles at a hydrophilic surface, that micelles close to the surface deviated from spherical symmetry. The present investigations do not warrant such a conclusion, however, the hard-sphere interaction and micelle radius perpendicular to the surface were slightly below the values found in the bulk.

It has been suggested that hemispherical micelles may form at the surface [135]. However, the formation of such structure requires a strong attraction between the core and the surface. Ellipsometry measurements of the adsorption of homopolymers PEO and PPO on hydrophilic silica led *Malmsten et al.* [79] to the conclusion, that PEO adsorbs to the surface, whereas PPO does not in a measurable amount. The PPO will thus not initiate the growth of a hemi-spherical micelle at the surface as the critical micelle temperature is passed. The break-up of existing micelles is not plausible because it demands a strong attraction between the core and surface, which does not seem to exist. From the present study it does not seem likely that these aggregates form on the surface due to the water layer at the surface.

It has been observed that as the critical micelle temperature or concentration is surpassed, there is a strong increase in the adsorbed amount [79]. From the present study this increase can be explained by geometrically confined micelles showing hard-sphere ordering at the solid-liquid interface.

4 Modeling of the Micellar Order at the Solid-Liquid Interface

Free-form determined surface profiles from the reflectivity measurements indicated that triblock copolymer micelles form layers at the surface with increasing disorder away from the surface. Inspired by the free-form profiles, a model was proposed which showed excellent agreement with the experimental reflectivity data. The micelle was modeled as either a solid sphere or a solid sphere with tethered Gaussian chains in accordance with the findings of Chapter 2. With the assumption that the micelles interact trough a hard-sphere potential, the density of hard-spheres at a hard wall was assumed to be representative of the distribution of the micelles. The convolution of the projected density of the model of the micelle and the density of hard spheres at a hard wall gave the final expression for the scattering length density, which could be fitted to the data. Even though an outline of the derivation of the scattering length density already was given in the previous chapter, we will focus on the details of the rather tedious calculations involved in the model: First, a numerical expression for the density of hard spheres at a hard wall is obtained from Monte Carlo simulations in the micellar volume fraction, η, ranging from 0.05 to 0.4789. Secondly, a parameterization is obtained for the projected radial scattering length density of the micelle, which is finally convoluted with the center distribution of the micelles to arrive at the final expression for the scattering length density, $\rho(z)$.

4.1 Density of the Hard Spheres at a Hard Wall

The first part of the calculation scheme is to obtain a numerical expression for the center distribution of the micelles.

The Hard-Sphere Interaction

Is the Hard-Sphere Model a Good Approximation?

In the following it will be argued, that hard-sphere interaction is a reasonable assumption for the micelles. *Genz et al.* [40] set forward a scheme for determining under which conditions the hard-sphere model is a sufficiently good approximation. In the framework of perturbation theories, the osmotic pressure and the isothermal compressibility were calculated using liquid state theory, which employs the closure relation of *Rogers and Young* [118], and thereafter compared with the theoretical hard-sphere behaviour. The authors found, that a direct hard-sphere, an effective hard-sphere, and a soft-potential regime could be distinguished from two characteristic parameters defined as

Perturbation Approach

$$L^*_{\mathrm{ST}} = 1 + d_L/R - \sigma^*_{EV} \tag{67}$$

and

$$\sigma^*_{EV} = \sigma_{EV}/(2R), \tag{68}$$

where R is the particle core radius, d_L the thickness of the polymer layer, and σ_{EV} the diameter of the hard sphere corresponding to a pure hard-sphere system. L^*_{ST} and σ^*_{EV} are a measure of the soft-tail effects and of the excluded-volume effects, respectively. The approximate values for the P85 micelles are $R = 50$ Å and $\sigma_{EV} = 150$ Å [94] and the radius of gyration $R_g(= d_L/2)$ for the 25 monomers of ethylene oxide is 11 Å [105]. Hence, the two parameters for the P85 triblock copolymer are $\sigma^*_{EV} = 1.5$ and $L^*_{\mathrm{ST}} = -0.06 \approx 0$, which according to *Genz et al.* is representative of an effective hard-sphere system. An effective hard-sphere

system is in this context defined as system where the interaction is only slightly "soft". Hence, the volume fraction of the system can be scaled in such a way that hard-sphere behaviour is recovered.

Self-Consistent Field Theory

Self-consistent field (SCF) theory has been used to calculate the form of the interaction potential between polymer chains tethered to a spherical interface [83, 72]. The tendency in the calculations is that the steepness of the potential increases with decreasing degree of polymerization of the tethered chains, N, and with larger core radius, R. From comparison with the SCF calculations [72] the potential is hard-sphere like for the 25 monomers of EO tethered to a core radius of $R \approx 50$ Å, the values for the P85 micelle [94].

SANS Measurements

As a last argument for the hard-sphere potential, *Mortensen & Pedersen* [94] have successfully treated the micelles as hard spheres in the analysis of the small-angle neutron scattering data. Also evident from Chapter 2 is the fact that inter-micellar interactions gives rise to a peak in the scattering curves which increase with increasing polymer concentration and temperature (see Figure 11). The interaction peak can be fitted by a structure factor calculated for a hard-sphere model. This indicates that the inter-micellar interaction potential rises sharply as soon as the PEO chains in the coronas start to interpenetrate.

For these reasons the micelles in solution are treated as a hard-sphere fluid.

Monte Carlo Simulations

Previously, the hard-sphere fluid near a hard wall has been extensively studied by Monte Carlo (MC) [127, 45] and Molecular Dynamics (MD) simulations [54] in order to test, e.g., density functional theory of fluid ordering. The first Monte Carlo simulation study was performed by *Snook & Henderson* [127] in 1978 and has later been extended by *Groot et al.* [45]. However, none of the simulation studies offered a paramerization of the density profile. In order to fit the experimental data, a complete parameterization has consequently been performed of the MC simulations of hard spheres at a hard wall for hard-sphere volume fractions, η, ranging from 0.05 to 0.46. Note, that instead of volume fraction one often refers to the system in terms of the dimensionless volume $\rho\sigma^3 = 6\eta/\pi$, where η is the bulk volume fraction, σ the hard core diameter, and ρ the number density. In the present simulations $\rho\sigma^3$ varies from 0.096 to 0.879.

Simulation Set-up

A series of Monte Carlo simulations were performed on a system consisting of 1000 hard spheres confined by a pair of hard walls. The system is identical to the one used by *Snook & Henderson* [127]. The $x-y$ plane is defined to be parallel to the walls, which act as a boundary for the system in the z direction at $z = 0$ and $z = L_z$. Periodic boundary conditions are used in the x and y direction. Initially, the hard spheres are placed on a face-centered cubic (FCC) lattice. The cubic lattice parameter is determined by the nominal hard-sphere volume fraction, η_{nom}, from

$$a = \sqrt[3]{\frac{4V_{\text{HS}}}{\eta_{\text{nom}}}}, \tag{69}$$

where V_{HS} is the hard-sphere volume, a the lattice parameter, and $\eta_{\text{nom}} = V_{\text{HS}}^{\text{tot}}/V^{\text{tot}}$, $V_{\text{HS}}^{\text{tot}}$ and V^{tot} being the total volume of hard sphere in the system and the total volume, respectively. The whole system has an equal number of unit cells in the x and y direction and twice the number in the z direction. To avoid finite size effects all the simulations had (x,y,z)-dimensions greater than the minimal size of $10\sigma \times 10\sigma \times 16\sigma$, where $\sigma = 2R_{\text{HS}}$ is the hard-sphere diameter, as suggested by *Groot et al.* [45].

Actual Volume Fraction

Due to the finite size of the system, the hard-sphere volume fraction decreases

as the hard spheres order on the surface effectively removing hard spheres from the bulk. Thus, the actual volume fraction, η, is lower than η_{nom} and has to be calculated from the plateau, where the density reaches a constant value far away from the walls. The plateau occurs due to the bulk liquid like ordering of the hard spheres, which has no translational order with respect to the walls. Hence, the walls can be considered as independent and the profile averaged over the two walls with the midpoint between the two walls as center of symmetry.

Simulation Procedure

The simulation was run for nominally 10^3 equilibration steps per particle, before the 10^5 sampling steps per particle. Each movement of the randomly chosen hard sphere was rejected if an overlap occurred with neighboring spheres or the walls. The increment was chosen to efficiently probe phase space, which has been found to correspond to a rejection rate chosen to 0.5 as a rule-of-thumb [51]. After the equilibration, the configuration of the system was probed every 10^4 steps and a center position histogram was calculated. The position histogram was split into ten blocks in order to estimate the standard errors. Because the hard sphere-wall system is athermal, the structure depends only on the volume fraction η. Simulations were performed for ten values of η below the hard-sphere freezing transition [111] at $\eta = 0.49$.

Simulations by Groot et al.

In the simulations by *Groot et al.* [45] the start configuration was obtained by randomly moving a number of spheres, initially placed on a FCC lattice, until the desired density was reached. In these simulations the spheres were randomly moved using a Maxwell-Boltzmann distribution for the velocity multiplied by a fixed time step. Within this approach, ideal fluid mixing is obtained for a time step that results in an acceptance of 18 % of the attempted moves. The results from the two simulation approaches will be compared in a later section.

Parameterization of the Density of Hard Spheres

From the simulations, a numerical approximation consisting of analytical functions for the density of the hard spheres was found. This will later allow us to convolute with the projected density of the micelles. In effect, this step enables us to fit to the free-form scattering length density profiles and finally the reflectivity data directly as demonstrated in the previous chapter. From the simulations it was found by trial-and-error, that the density of hard spheres can be expressed as:

$$\begin{aligned}\rho(z,\eta) &= 1+\left[A_1\frac{\sin(x_1)}{x_1}+A_2\frac{\cos(x_1)}{x_1}\right]\exp(-D_1 z)\\ &+\left[A_3\frac{\sin(2S_1x_2)}{2x_2}+A_4\frac{\cos(2S_2x_2)}{2x_2}\right]\exp(-D_2 z)\\ &+A_5\frac{\sin(3S_3x_3)}{3x_3}\exp(-D_3 z)\\ &+\frac{A_6}{|x_{g1}-\eta|}\frac{1}{\sigma_g\sqrt{2\pi}}\exp\left[-\frac{1}{2}\left(\frac{L_p+x_{g2}-z}{\sigma_g}\right)^2\right].\end{aligned} \tag{70}$$

In equation (70) A_i are the amplitudes, D_i the decay constants, S_i the "slip" factors, and x_i is given by $x_i = 2\pi(z-\phi_i)/L_p$, where L_p is the period and ϕ_i a displacement. Here, x_{gi} are offsets optimized in order for the expression to increase ρ at the first side maximum and σ_g is the standard deviation of the Gaussian.

Optimization of the parameters Each simulation was initially fitted by the expression for ρ starting with the most structured density profile, i.e. the highest volume fraction $\eta = 0.459$, and thereafter the less structured profiles with decreasing volume fraction. The variation of L, A_i, D_i, ϕ_i, and S_i was expressed

as polynomials of maximum fourth degree in η. The result revealed a function of 53 ($= N_{\text{par}}$) parameters, which was fitted to the full range of ten ($= N_{\text{sim}}$) simulations ranging from $\eta = 0.050$ to $\eta = 0.459$. Due to oscillatory behavior of the fits below z_0, the minimum z value of the simulations, a linear extrapolation was performed for z values lower than z_0. The z_0 value can be expressed as a function of η on the following form $z_0(\eta) = 0.08121 + 1.388\exp(-(\eta + 0.2814)/0.1249)$. The ten data sets were fitted once again including the extrapolation. The final expression was tested against the published results of *Groot et al.* [45]. Since a reasonable correspondence was found, the $\eta = 0.4789$ data set of *Groot et al.* was included to provide a parameterization valid up to almost the point of hard-sphere crystallization occurring at $\eta = 0.49$. For the full ten data sets

Inclusion of the $\eta = 0.4789$ Groot et al. data set

χ^2

$$\chi^2 = \frac{1}{(\sum_{i=1}^{N_{\text{sim}}} N_i) - N_{\text{par}}} \sum_{i=1}^{N_{\text{sim}}} \sum_{j=1}^{N_i} \frac{[\rho_i^{\text{SIM}}(z,\eta_j) - \rho_i^{\text{PARAM}}(z,\eta_j)]^2}{\sigma_{i,j}^2} \tag{71}$$

was 4.5, where ρ^{SIM} is the density obtained from the simulation, ρ^{PARAM} the density from the parameterization, and N_i the number of points for volume fraction η_i in the simulation. Each point has a standard deviation $\sigma_{i,j}$. Without the *Groot* data set, a optimization of the parameters gave $\chi^2 = 2.5$.

Deviations

The largest deviation in percent between the simulation and the parameterization was found to be 12.2% occurring in the *Groot* data set. Without the *Groot* data, the largest deviation was found to be 10.9% occurring at the highest volume fraction $\eta = 0.46$. Another measure is the difference between the simulation and parameterization divided by the standard deviation of the simulation, which was found to be largest (9.79) for the lowest volume fraction $\eta = 0.05$. Typically, both measures were below 5% and 5, respectively. The parameters found from the parameterization are listed in Table 10 and six examples of the best simultaneous fit to the density profiles are depicted in Figure 33. The full parameterization is depicted on the left hand side of Figure 38.

Term	η^4	η^3	η^2	η	η_0
L				-1.390	2.475
A_1			-543.7	198.5	-7.800
A_2	8327	-7142	2033	-291.5	7.485
A_3			24.83	-5.796	0.6781
A_4		121.8	-68.17	12.28	-0.5645
A_5			-9.567	1.160	0.07987
A_6					3.869×10^{-4}
D_1			1.924	-3.992	1.658
D_2		-82.04	82.13	-27.94	3.762
D_3			-13.49	3.917	1.299
ϕ_1				1.728	-7.365
ϕ_2				-0.2868	0.09303
ϕ_3			-0.9152	-0.2843	0.4658
S_1			-1.614	0.7620	0.9761
S_2	18.67	-80.00	73.61	-24.16	3.452
S_3		19.84	-19.98	5.269	0.7720
x_{g1}					0.4736
x_{g2}					0.07436
σ_g					0.07660

Table 10. The coefficients of the polynomials of the volume fraction η obtained for the parameterization of density of hard spheres at a hard wall. In the case of a zero value coefficient, it is omitted from the table.

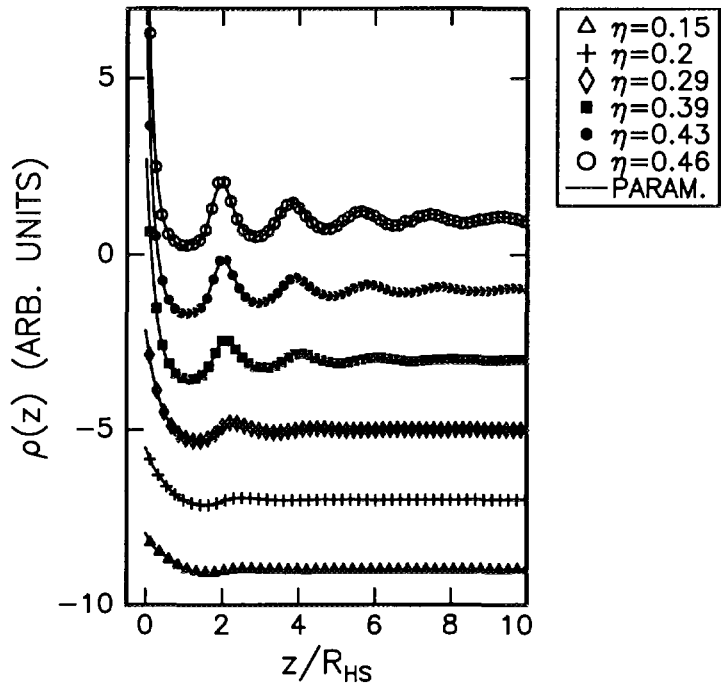

Figure 33. Six examples of the parameterization of the density of hard spheres at a hard wall found from Monte Carlo simulations.

In order to test the parameterization below $\eta = 0.4789$, the final expression was least-squares fitted to the four other examples given by *Groot et al.* [45]. The hard-sphere volume fraction, η, was the only parameter allowed to vary. The values are listed in Table 11 and the fits are depicted in Figure 34.

The largest relative deviation in percent between the parameterization and four examples of the *Groot*-density below $\eta = 0.4789$ is 7.0 % ($\eta = 0.3744$ data set). Hence, good agreement is found between the two simulation procedures.

η_{Groot}	η_{param}	$\Delta\rho/\rho_{\text{Groot}}$ (%)
0.3008	0.3054±0.0013	1.5
0.3744	0.3718±0.0009	0.7
0.3969	0.3943±0.0008	0.7
0.4247	0.4216±0.0010	0.7
0.4783	0.4789±0.0007	0.1

Table 11. The hard-sphere volume fractions η obtained from fitting to the five published data sets of Groot et al. [45]

4.2 Determination of the Projected Density of a Micelle

The Center-Symmetric Scattering Length Density $\rho(r)$

The next step after determination of the center distribution of the micelles is to model the micelle and obtain an expression for the projected scattering length density. The projection is necessary due to the fact that only the scattering length

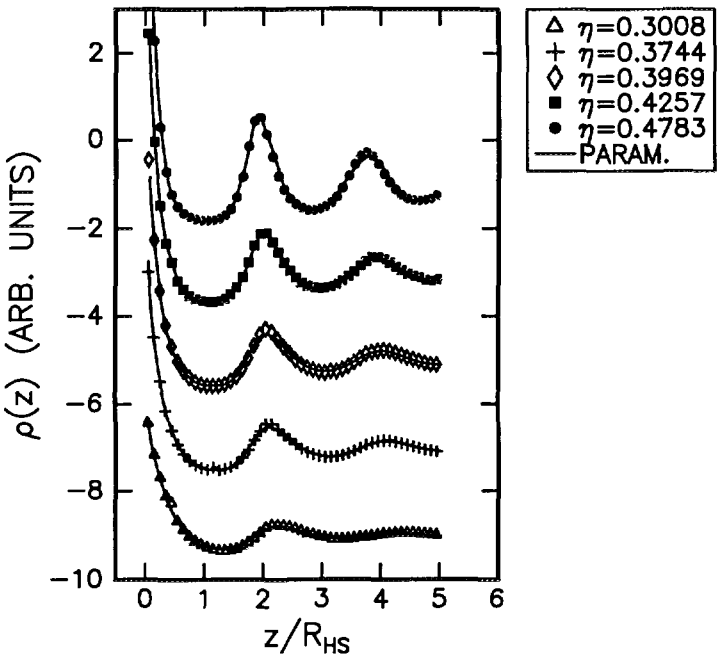

Figure 34. Fits to the Monte Carlo simulations of hard spheres at a hard wall from Groot et al.. The only fitting parameter was the micellar volume fraction η, which in all cases were found to correspond to the values given by Groot (see Table 11).

density profile along the surface normal is obtained from specular reflectivity.

In Chapter 2 it was shown from bulk measurements of P85, that the micelles can be modeled as a spherical core with polymer chains tethered to the surface. The chains are incapable of penetrating the core and Monte Carlo simulations showed that the effect can be mimicked by a translation of the points of attachment of the chains to approximately $R + R_g$, where R and R_g is the radius of the sphere and the radius of gyration of the chains, respectively. For center-symmetrical particles the radial scattering length density $\rho(r)$ can be written on the form [43]:

Radial Scattering Length Density

$$\rho(r) = \frac{1}{2\pi^2}\int_0^\infty A(q)\, q^2 \frac{\sin(qr)}{qr} dq, \tag{72}$$

where $A(q)$ is the form factor amplitude , and $q = (4\pi/\lambda)\sin\theta$ is the scattering vector of neutrons scattered at an angle 2θ and with a wavelength λ. An expression for $A(q)$ of a solid sphere or a tethered chain can be identified from the expression for the total scattered intensity from a micelle with a spherical core and Gaussian chains attached to the surface (cf. Chapter 2 and ref. [105]):

$$\begin{aligned} I(q) &= |A|^2 \\ &= \left|\int \rho(\vec{r}) \exp(iq\cdot\vec{r})\right|^2 \\ &= S_{ss}^{self} + 2S_{sc} + S_{cc} + S_{cc}^{self} \end{aligned} \tag{73}$$

where s and c are abbreviations for sphere and chain, respectively.

The normalized self-correlation term S_{ss}^{self} for a sphere with radius R is given by $S_{ss}^{self} = \Phi(q,R)^2$, where $\Phi(q,R)$ is the form factor amplitude:

$$\Phi(q,R) = \frac{3[\sin(qR) - qR\cos(qR)]}{(qR)^3}. \tag{74}$$

Fourier Transform of $\Phi(q,R)$ gives the trivial contribution from the sphere to $\rho(r)$:

Contribution from the Sphere

$$\rho_s(r) = \frac{1}{2\pi^2}\int_0^\infty \Phi(q,R)q^2\frac{\sin(qr)}{qr}dq \tag{75}$$

$$= \begin{cases} 3/(4\pi R^3) = V_{hs}^{-1} & r \le R \\ 0 & r > R. \end{cases} \tag{76}$$

For chains attached center-symmetrical at a distance $R + R_g$ the form factor amplitude is

$$A_c(q) = \left[\frac{1-\exp(-x)}{x}\right]\frac{\sin(q(R+R_g))}{q(R+R_g)}, \tag{77}$$

where $x = R_g^2q^2$, R_g is the radius of gyration given by $R_g^2 = Lb/6$, L the contour length, and b the statistical segment (Kuhn) length of the chain. The Gaussian chain statistics break down at distances smaller than the Kuhn length b. This gives rise to a singularity in the radial scattering length density for the tails $\rho_t(r)$, which can be removed by introducing an effective cut-off in the following way:

$$\rho_t(r) = \frac{1}{2\pi^2}\int_0^\infty A_c(q)q^2\frac{\sin(qr)}{qr}\exp[-(q/q_0)^2]dq, \tag{78}$$

where $q_0 = 10/R_g$ is chosen as a reasonable estimate in the present case. The solution of the integral can be expressed analytically as

Contribution from the Chains

$$\rho_t(r) = \frac{1}{16\pi^{\frac{3}{2}}R_g^2(R+R_g)r}\times \tag{79}$$

$$\left\{|R+R_g-r|\left[\Gamma\left(-\frac{1}{2},0.2475u_1^2\right)-\Gamma\left(-\frac{1}{2},25u_1^2\right)\right]+\right. \tag{80}$$

$$\left.(R+R_g+r)\left[\Gamma\left(-\frac{1}{2},25u_2^2\right)-\Gamma\left(-\frac{1}{2},0.2475u_2^2\right)\right]\right\}, \tag{81}$$

where

$$u_1 = \frac{R+R_g-r}{R_g}, \qquad u_2 = \frac{R+R_g+r}{R_g}, \tag{82}$$

and $\Gamma(a,z) = \int_z^\infty t^{-a-1}e^{-t}dt$ is the incomplete Gamma function.

The Projected Density $\rho(z)$

After having obtained the radial expression for the scattering length density we want to calculate the projected scattering length density profile $\rho(z)$ from the radial $\rho(r)$.

Solid Sphere. In the case of a solid sphere, $\rho(r)$ is constant within the sphere. In a projection along an arbitrary axis through the center of the sphere, which is conveniently denoted as the z axis, $\rho(r)$ will have to be weighted by the volume element ΔV centered around the corresponding z value (cf. Figure 35). The volume element will have the same form as a right circular cone of radii x_1 and x_2 with height Δz:

$$\Delta V = \frac{1}{3}\pi(x_1^2 + x_1x_2 + x_2^2)\Delta z. \tag{83}$$

As Δz becomes infinitesimal, $x_2 = x_1$ and the index can be removed in the differential form

$$dV = \pi x^2 dz = \pi\ (R^2 - z^2)dz, \tag{84}$$

where R is the radius of the solid sphere. Hence, the projected scattering length density $\rho_s^{\text{norm}}(z)$, normalized to unity over the z range, becomes

$$\rho_s^{\text{norm}}(z,R) = \frac{3}{4}\frac{1}{R}\left[1-\left(\frac{z}{R}\right)^2\right]. \tag{85}$$

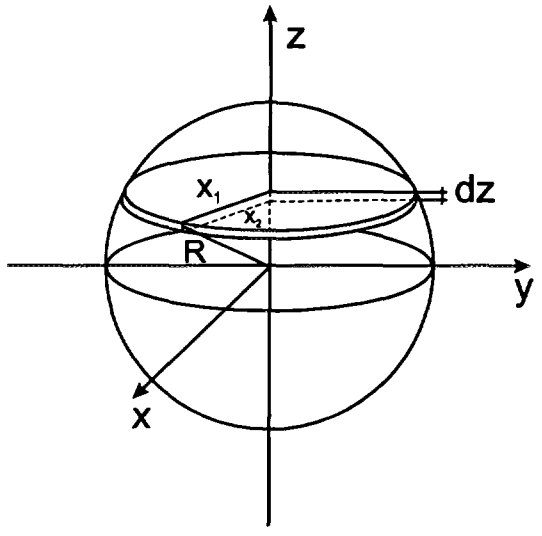

Figure 35. An illustration of the weighting of the constant $\rho(r)$ in the solid sphere.

Gaussian Chains. As shown from the bulk analysis the dissolved chains of the micelles can be treated as Gaussian chains attached radially at $R+R_g$, where R is the radius of the core and R_g the radius of gyration of the Gaussian chains. Since the density of the chains has been found as a function of the radial distance r, each z value will cut the radial density at different r values depending on the distance from the z axis, i.e. for different aximuthal angles ϕ (cf. Figure 36). If x is the distance from the z axis, we have the relation $x^2+z^2=r^2$. To achieve the full contribution to $\rho_t(z)$ we have to sum all the contributions from different x values with the appropriate weighting. For a given z, each x and thus $\rho_t(r)$ value is weighted by the outer surface area, ΔA, of the right circular cone with center at z and with radii x_1 and x_2 and height Δz:

$$\Delta A = \pi(x_1+x_2)\Delta z. \tag{86}$$

For an infinitesimal Δz, $x_2=x_1$ and the index can be removed leaving the differential relation

$$dA = 2\pi x dz. \tag{87}$$

The summation of all the chain contributions perpendicular to the z axis has to be calculated, leaving the final expression for the projected normalized scattering length density:

$$\rho_t^{\text{norm}}(z,R) = \frac{\int_0^\infty 2\pi x\rho_t(r)dx}{\int_{-\infty}^\infty\int_0^\infty 2\pi x\rho_t(r)dxdz} = \frac{\int_0^\infty 2\pi x\rho_t(\sqrt{z^2+x^2})dx}{\int_{-\infty}^\infty\int_0^\infty 2\pi x\rho_t(\sqrt{z^2+x^2})dxdz}. \tag{88}$$

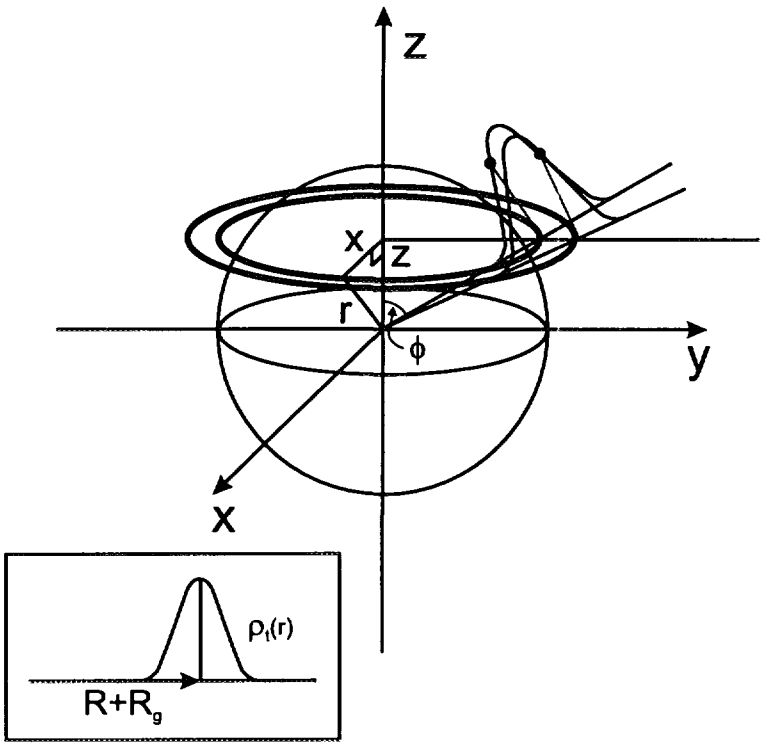

Figure 36. An illustration of the weighting of the density $\rho_t(r)$ of the tethered chains attached at $R + R_g$. The full circles show how two values of $\rho_t(r)$ are obtained for different x at constant z. The insert shows the radial density of the chains attached at $R + R_g$.

Parameterization of the Tails Unfortunately, it has not been possible to obtain an analytical expression for the projected chains. Consequently, a first approach is to calculate numerically the projected density from eqn. (88) and then parameterize the projected scattering length density for the 25 monomers of ethylene oxide. The radius of gyration for 25 monomers of EO, treated as Gaussian chains, can be calculated to be $R_g^{PEO} = 10.8$ Å [105], which is used in the calculation of the projected scattering length density of the tails. No simple power law expression was found for the projected density, and consequently the following functional form was used in the parameterization of $\rho_t^{\text{norm}}(z)$:

No Analytical Expression for the Projected Chains

$$\rho_{\text{chain}}(z) = \begin{cases} B_2 & z < B_1 \\ B_2 \exp(-|B_3(|z| - B_1)|^{B_4}) & r \geq B_1. \end{cases} \tag{89}$$

The values of the function was found by least-square fitting to $(B_1, B_2, B_3, B_4) = (57.22 \pm 0.31, 0.006691, 0.0527 \pm 6 \times 10^{-4}, 1.849 \pm 0.011)$ for chains tethered to a sphere with radius $R = 60$ Å. Note, that B_1 is a function of the radius of the core of the micelle, R, thus it would have to be rescaled when $R \neq 60$ Å along with the recalculation of the normalization integral in the denominator of eqn. (88). The projected scattering length density and the parameterization are depicted in Figure 37.

Weighting of the Sphere and the Tails

Finally, we will calculate the appropriate weighting factors W_s and W_t, when the contribution from the tails and the chains have to be taken into account in the total scattering length density profile, $\rho_{mic}(z)$:

$$\rho_{mic}(z) = W_s \rho_s^{\text{norm}}(z) + W_t \rho_t^{\text{norm}}(z). \tag{90}$$

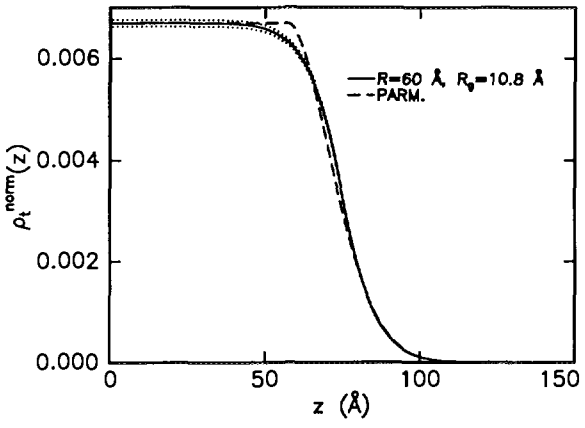

Figure 37. The projected scattering length density profile of Gaussian chains attached at $R+R_g$, where the radius of gyration $R_g = 10.8$ Å and the radius $R = 60$ Å (full curve). The dotted curves are the 1 % uncertainty on the projection used for optimizing the parameterization (dashed curve).

Weighting by the Excess Scattering Length Density and the Volume in the Micelle

Firstly, the normalized scattering length density of the PEO chains and the PPO sphere are each weighted by their excess scattering length density (with respect to medium through which the neutrons enter the solid-liquid interface) and their total volume in the micelle. For the EO chains the excess scattering length density and the total volume in the micelle are $\Delta\rho_{EO} = \rho_{EO} - \rho_{quartz}$, where ρ_{quartz} is the scattering length density of quartz, and

$$V_{PEO}^{tot} = N_{agg} N_{EO} V_{EO}, \tag{91}$$

respectively. In this case $N_{agg} = 4\pi R^3/(3V_{PPO})$, N_{EO}, and V_{EO} are the aggregation number, the number of monomers in a single chain, and the monomer volume, respectively. Hence, the basic equation is

$$W_t \rho_t^{norm}(z) = \frac{\rho_t(z)}{\int \rho_t(z)dz} \Delta\rho_{EO} V_{PEO}^{tot}. \tag{92}$$

Normalized Projected Scattering Length Density

Similar relations are valid for PO. The final expression for the normalized scattering length density is given by

$$\rho_{mic}^{norm}(z,R) = \frac{\rho_t^{norm}(z,R)\Delta\rho_{EO}V_{PEO}^{tot}(R) + \rho_s^{norm}(z,R)\Delta\rho_{PO}V_{PPO}^{tot}(R)}{\Delta\rho_{EO}V_{PEO}^{tot}(R) + \Delta\rho_{PO}V_{PPO}^{tot}(R)}, \tag{93}$$

where $\Delta\rho_{EO}$ and $\Delta\rho_{PO}$, are the scattering length density difference between the EO or PO chains and the medium through which the neutrons enter the solid-liquid interface, respectively. Because the scattering length density of the tails, ρ_t^{norm}, and the solid spheres, ρ_s^{norm}, are normalized to unity, it can easily been seen that the total density of the micelles, ρ_{mic}^{norm}, likewise will be normalized to unity.

When the micelles are modeled as solid spheres, we simply use $\rho_{mic}^{norm} = \rho_s^{norm}$ in the convolution integral.

Figure 38 shows the different parts of the model calculation. In the insert the projected scattering length density of the sphere, the chains, and their combination are depicted.

4.3 Final Expression

The last step in the derivation of the model expression is to convolute the center distribution of the micelles, ρ_{HS}, with the normalized scattering length density of

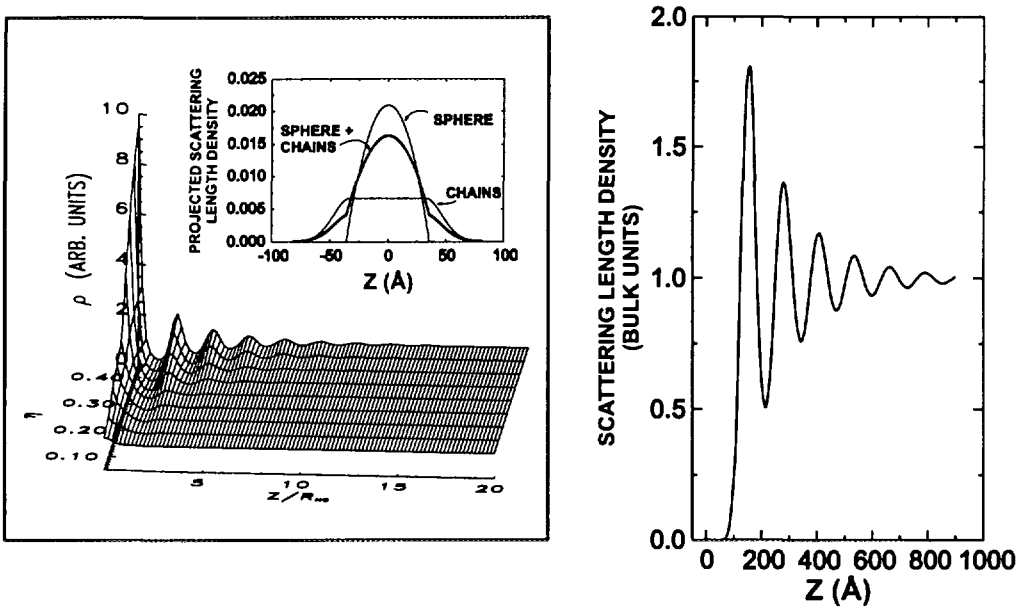

Figure 38. The different parts in the model calculation. The left-hand side shows the parameterization of density, $\rho(z)$, of hard spheres at a hard wall obtained from Monte Carlo simulations as a function of the volume fraction, η, and distance, z, from the surface. The insert depicts the normalized scattering length densities of the projection of the sphere, the tethered chains and the combination. The convolution of the density of hard spheres and the density of the solid sphere with tethered chains is depicted on the right-hand side. The values used are $R = 36$ Å, $R_{HS} = 68$ Å, $\eta = 0.44$, and $z_{offset} = 140$ Å.

a micelle, ρ_{mic}^{norm}. In order to compare the model with the experimental profiles we have to take into account that the micelles are dispersed in a solvent.

Taking the Solvent into Account

From the reflectivity measurements (see Chapter 3) we deduced that a layer forms on the surface with a scattering length density, which we denote ρ_{fluid}. Furthermore, at large distances from the surface the scattering length density must tend to the bulk average value of the micellar liquid. If we for convenience normalize the scattering length density with respect to the bulk average value, the final expression must tend to ρ_{fluid}/ρ_{bulk} when z goes to zero and 1 when z is large. Here, ρ_{bulk} is the scattering length density of the bulk liquid. The following expression fulfills the requirements:

Final Expression

$$\rho_m(z, \rho_{fluid}, R, R_{HS}/R, \eta, z_0) = \Delta\rho_{fluid} - (\Delta\rho_{fluid} - 1) \times \int_{-\infty}^{+\infty} \rho_{mic}^{norm}(x, R)\rho_{HS}((z - z_0) - x, R, R_{HS}/R, \eta)dx \quad (94)$$

where $\Delta\rho_{fluid}$ is the excess scattering length density of the fluid closest to the quartz surface, R the radius of the core of the micelles, R_{HS} the hard-sphere interaction radius, z_0 an arbitrary zero point. Consequently, the model has five free parameters ρ_{fluid}, η, R, R_{HS}/R, and z_0, to be determined from a non-linear least-squares fit to the free-form profiles or directly to reflectivity data. In the latter case, z_0 is replaced by three times the standard deviation of an error function, σ_{surf}, describing the solid-liquid interface. The aggregation number is readily calculated from the core radius by $N_{agg} = 4\pi R^3/(3V_{PPO})$, where V_{PPO} is the volume of a propylene oxide block in the triblock copolymer. An example of the convolution integral only is shown on the right hand side of Figure 38 for $R = 36$ Å, $R_{HS} = 68$ Å, $\eta = 0.44$, and $z_{offset} = 140$ Å.

Figure 39 shows a comparison between the convolution of the projected scattering length density and the center distribution of the micelle for the two representations of the micelle: The solid sphere and the solid sphere with tethered Gaussian polymer chains. The introduction of the tethered chains has a dramatic effect on the amplitude and shows a more smooth profile, which indicates that the tails cannot be neglected.

Comparison between the Convolution of the Projected Scattering Length Density and the Center Distribution of the Micelle

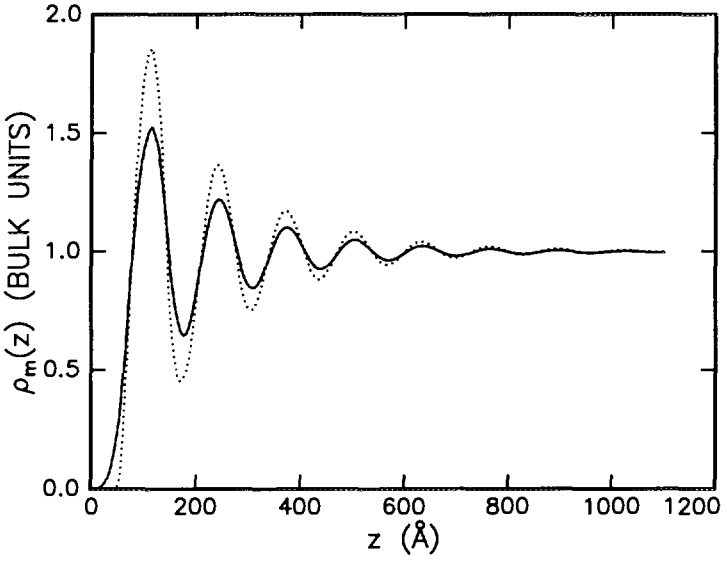

Figure 39. A comparison between the convolution of the projected scattering length density and the center distribution of the micelle for the two different representations of the micelle. The micelle is treated as a solid sphere (dotted curve) or as a solid sphere with tethered chains (full curve).

4.4 Limitations of the Model

We have presented a model for the ordering of micelles at the solid-liquid interface. An analytical expression has been obtained for the density of hard spheres, which convoluted with the projected scattering length density of the micelle, is capable of either the free-form determined scattering length density profiles or the neutron reflectivity measurements directly. The model has five free parameters ρ_{fluid}, η, R, R_{HS}/R, and z_0 or σ_{surf}. The micelle was either treated as a solid sphere or a solid sphere with tethered Gaussian chains. The inclusion of the tethered chains was found to significantly modify the projected density of the micelle and hence the convolution integrals. The main limitations of the model are:

- The model did not include any form of polydispersity.
- The micelles were assumed to interact via a hard-sphere potential.
- The conformation of the tethered chains is assumed to obey Gaussian statistics with a radius of gyration fixed at a reasonable value; R_g=10.8 Å.
- The parameterization of the projection of the tails may be improved.

5 The Surface Induced Ordering of the Rod-like Phase

In the previous chapter focus has been directed towards the surface-induced ordering of spherical micelles. The micelles were found to order like hard spheres at a hard wall. At higher temperatures the bulk micelles have been found to elongate at elevated temperatures close to 70°C [94]. The obvious question is now what effect the presence of a surface has on the ordering of the micelles of P85 as they become more anisotropic. It has been shown that the structure of rod-like aggregates of amphiphilic molecules in solution is closely related to the ordering of liquid crystals [89]. For liquid crystals, the molecules have been found by experiments and simulations to attain different structures at the surface than in the bulk. Examples are the clear evidence for surface induced smectic ordering in the nematic phase of octyloxycyanobiphenyl (8OCB) seen by X-ray diffraction [9, 110] and the nematic ordering of rod-like molecules in an isotropic bulk phase [81, 82, 101]. The rod-like micelles of the triblock copolymer P85 in aqueous solution provide a way to investigate the surface ordering of anisotropic aggregates at a hydrophilic single crystal quartz surface. The temperature dependence of the ordering will be investigated and thus the effect of elongation of the aggregates in solution. As the P85 micelles elongate, an increased degree of order is expected at the surface from purely geometrical considerations.

Surface-Induced Ordering of Anisotropic Aggregates

However, the geometrical constraints are not the only aspect to consider. The hydrophobic interactions and consequently the interplay between enthalpy and entropy play a vital role in the aggregation of the amphiphilic P85. The same considerations apply to the surface ordering. Structures as e.g. lamellae might form on the surface as the triblock polymers find it favourable to dehydrate and thereby exclude water from the structure. At elevated temperatures, ordering of this kind might occur as the water becomes a poorer solvent with temperature for the ethylene oxide chains which consequently contract.

Hydrophobic Interaction

In the bulk, rod-like aggregates of P85 have been observed to align in a shear field [89]. Furthermore, the charged thread-like micelles of the cationic surfactant cetyl-trimethylammonium 3,5-dicholorobenzoate have been shown to form a shear-induced hexagonal ordering at a quartz surface [47, 48]. Consequently, the response of the rod-like micelles of P85 to a shear field will be examined at the surface of quartz.

Applied Shear Field

5.1 Bulk Measurements

Drastic changes occur in the bulk phase when aqueous solution of P85 with concentration $c < 15$ wt % is heated above approximately 70 °C. In the structure analysis by *Mortensen & Pedersen* [94] based on SANS measurements, the scattering function was observed to change drastically above approximately 70 °C in the low-concentration regime; the characteristic correlation peak, seen for the spherical micelles, totally disappeared. The pair-correlation function was found to be similar to the one of prolate ellipsoids with an increasing major axis with increasing temperature. It was observed that an increase in temperature or concentration caused a more elongated structure of the aggregates. *Mortensen & Pedersen* [94] suggested a transformation from spherical to rod-like micelles with an intermediate prolate ellipsoidal structure.

SANS Measurements

In the more dilute region, aqueous solutions of P85 have been shown to transform into a soft gel at higher temperatures in support of the sphere-to-rod transition hypothesis. Capillary viscosity measurements [122] ($c < 1$ wt %) showed

Soft Gel

a large increase in the viscosity as the temperature exceeded 70°C. The effect became more pronounced with increasing concentration. These findings were in agreement with low-shear viscosity measurements [44], which showed a similar temperature dependence of the viscosity up to about 15 wt %. Furthermore, in the related system of P94, which has approximately the same molecular weight as P85, *Jørgensen et al.* [115] found from viscoelastic techniques a transformation from a Newtonian behavioured solution to a soft gel when the temperature exceeded 60°C for concentrations in the range from 2 to 20 wt %.

Simple Rigid-rod Model

Based on the SANS findings and the viscosity measurements, *Schillén et al.* [122] assumed a simple rigid-rod model of the aggregates in order to interpret dynamic light scattering experiments. The length of the rods were estimated to be between 1400 and 2000 Å for 1 wt % at 75°C increasing with concentration and temperature. The length-to-diameter ratio is $L/d \approx 7$ for the lowest measured concentration $c = 0.025$ wt %. The simple model did, however, neglect the flexibility, polydispersity, and the non-uniform length of the aggregates.

Shear Measurements

Nematic Phase

Mortensen [89] found that the rod- or worm-like micelles align in a steady shear field forming a nematic phase. The alignment is stronger for higher concentrations (1 wt % compared to 10 wt %), since the viscosity and the length of the rods increase with concentration. The nematic ordering does not persist with time and the isotropic scattering is seen to reccur within the time resolution of a few seconds.

Because of the liquid crystalline features of P85 in solution, it is natural here to adopt the nomenclature and some of the features occurring in liquid crystal ordering. The next section will briefly introduce the properties and studies, which have been found useful for the present investigations.

5.2 Characteristics of Liquid Crystals

Director $\vec{n}$ and Order Parameter Q

The bulk state of a nematic phase is characterized by two parameters, a director $\vec{n}$ and an order parameter Q. The former is related to the average orientation of the molecules in a small volume element (though large on a molecular level) and the latter characterizes the distribution of the orientations of the molecules. The order parameter Q is equal to unity when all the molecules are aligned parallel to $\vec{n}$ and equal to zero when the distribution is isotropic. Characteristic for the liquid crystals is the occurrence of mesophases in between the disordered (isotropic) and the purely crystalline phases. In the isotropic phase, the molecules are disordered and can attain all orientations, whereas in the nematic mesophase the elongated molecules align parallel to each other, but have no long-range positional order. The smectic phase occurs when the aligned elongated molecules form well-defined layers perpendicular to the elongation direction. The general behaviour of liquid crystals, e.g. phase transformation and response to external fields, is comprised in the book of *de Gennes* [26]. The lyotropic colloidal mesophase relevant to the present chapter (such as rod-like micelles of amphiphiles in solution) and polymer liquid crystals have been reviewed by *Vroege and Lekkerkerker* [138].

Isotropic, Nematic, and Smectic Mesophases

The nematic phase is very sensitive to even weak external perturbations. The perturbation caused by a surface is likely to introduce a positional order of the molecules. The alignment can be planar, tilted, or homeotropic depending on whether the director directions are, respectively, parallel, tilted, or perpendicular to the plane of surface.

Smectic Surface Ordering

Several transitions have been identified at the surface of liquid crystalline materials. The first and now classic X-ray diffraction studies performed by *Als-Nielsen* [9], *Pershan* [110] and co-workers showed the clear evidence for surface induced

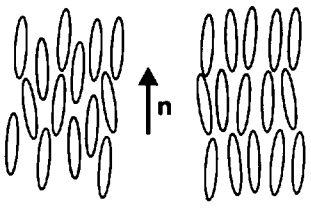

Figure 40. The nematic (left) and the layered smectic phase (right) occurring in liquid crystals. The vector $\vec{n}$ is the director.

smectic ordering in the nematic phase of octyloxycyanobiphenyl (8OCB). A thorough review of surface effects and related transitions have been given by *Jérôme* [59].

Nematic Surface Ordering

For isotropic solutions, such as the rod-like structure of P85, it has been found from modeling that the rods will form a nematic phase at the surface with the director parallel to surface. The transition is driven by the excluded volume interactions between the rigid rods and the wall. The planar alignment of the rigid rods was found to be favoured [101]. From modeling of rigid-rod-like molecules adsorbed at an attracting wall including solvent, *Matsuyama et al.* [81, 82] found a transition from isotropic to nematic transition at the surface at very low concentrations before nematic ordering was observed in the bulk. The onset concentration was decreased and the adsorbed amount increased by a more unfavourable solvent-solute interaction. However, this study had the severe limitation that rods adsorbed normal to the surface were neglected. Experimentally, the growth of a nematic surface layer in a bulk isotropic phase has been observed in low molecular weight liquid crystals (4-cyano-4'-n-alkyl-biphenyls, nCB, $n = 5, 6, 7, 8$) [61].

5.3 Interaction Between Aggregates

For this study a 5 wt % solution of P85 in D_2O was chosen to ensure both a measurable amount for the reflectivity measurements and at the same time interacting rod-like aggregates which may align due to the presence of a surface.

Interaction Between Rod-like Polymers

Doi & Edwards [30] have provided a scheme to determine the interactions between rod-like polymers at finite concentration. The scheme can easily be extended to rod-like aggregates. The authors distinguish between three regimes of rod-like polymers depending on the number of molecules per volume, ν:

- The dilute solution; $\nu \leq 1/L^3$, where L is the length of the rod-like polymer. Here, each polymer can freely rotate without interference of other polymers.
- The semidilute solution; $\nu << 1/dL^2$, where d is the diameter of the rod-like polymer. In this region, the effect of intermolecular interaction can be neglected for static, but not for the dynamic properties.
- Concentrated (isotropic) solution; $\nu > 1/dL^2$. Here, excluded volume interactions among the polymers are important in both static and dynamic properties. Polymers will tend to orient themselves in the same orientation as their neighbours.

If this distinction is applied to the P85 aggregates we obtain the following: From Chapter 2 the relation between the weight fraction, w_p, and the ratio between the solvent volume and the solute volume, V_{P85}/V_{D_2O}, is given by

$$\frac{V_{D_2O}}{V_{P85}} = \left[\frac{1}{w_p} - 1\right] \frac{\rho^m_{P85}}{\rho^m_{D_2O}}. \tag{95}$$

The ratio of mass densities, $\rho^m_{P85}/\rho^m_{D_2O}$, is approximately 0.9, which for the weight fraction $w_p = 0.05$ gives a ratio of volumes $V_{P85}/V_{D_2O} = 17.1$. The number of triblock copolymers per volume is

$$\nu_{P85} = \left(\frac{\rho^m_{P85} N_A}{M_{P85}}\right)\left(\frac{V_{P85}}{V_{D_2O} + V_{P85}}\right) = \left(\frac{\rho^m_{P85} N_A}{M_{P85}}\right)\left(\frac{1}{V_{D_2O}/V_{P85} + 1}\right), \quad (96)$$

where $\rho^m_{P85} = 1.011$ g/cm^3 is the mass density of dry P85, $M_{P85} = 4500$ g/mole is the molecular weight, and N_A Avogadro's number. As the considerations by *Doi & Edwards* are based on purely geometrical considerations, the distinction between the different regimes must be equally valid for rod-like aggregates. Thus, we can use the scheme by introducing the number of aggregates per volume, defined as $\nu' = \nu_{P85}/N_{agg}$ where N_{agg} is the aggregation number, instead of using the number of polymers per volume. The aggregation number can for prolate ellipsoids be estimated as the ratio between the ellipsoidal volume and the triblock copolymer volume:

Interaction Between Aggregates

$$N_{agg} = \frac{\frac{\pi}{6} d^2 L}{V_{P85}}, \quad (97)$$

where $V_{P85} = 6938$ Å^3 (at 50 °C, see Chapter 2), and d is twice the minor axis of a prolate ellipsoid and L its total length. From the pair-correlation function a 4 wt % solution of P85 at temperature $T \approx 75$ °C [94], we obtain $d \approx 100$ Å and $L \approx 300$ Å. With these values the aggregation number N_{agg} is 226.

For the 4 wt % solution the values from *Doi & Edwards* scheme are $1/L^3 = 3.7 \times 10^{-8}$ Å^{-3} and $1/dL^2 = 1.1 \times 10^{-7}$ Å^{-3}. The number of aggregates per volume is calculated to be $\nu' = 3.3 \times 10^{-8}$ Å^{-3}, which is slightly below $1/L^3$. Hence, the 5 wt % solution, which will be used here, corresponds to an dilute solution, where the aggregates are free to rotate without interference. It is thus hoped that a surface enforces alignment of the aggregates.

5.4 Experimental Section

SPEAR

SPEAR - Time-of-Flight Reflectometer

The measurements for the present investigations were performed at the Manual Lujan Jr. Neutron Scattering Center (MLNSC), Los Alamos National Laboratory, USA, on the Surface ProfilE Analysis Reflectometer (SPEAR) time-of-flight instrument (see Figure 41). The work was performed in collaboration with the local instrument scientists Dr. Greg Smith and Dr. Jarek Majewski.

Reflectometer Set-up

At MNLSC, the neutrons are produced by spallation when a pulsed 800 MeV proton beam with a time structure of 270 ns impinges on a tungsten target. The generated neutrons are moderated by a liquid hydrogen moderator at a temperature of 20 K to increase the flux of the long wavelength neutrons. The neutron beam is subsequently collimated to an average angle of 1 or 1.5° to the horizontal plane and converges 8.87 m from the moderator at the sample position. The time-of-flight instrument uses choppers to condition the neutron beam (i.e. reduce the background). Firstly, the T_0-chopper removes the high-energy neutrons and γ-rays. Secondly, the frame overlap chopper defines which of the two available wavelength bands (1-16 Å and 16-32 Å) are to be used. Furthermore, this chopper intercepts most of the very slow neutrons generated at earlier pulses. A set of Ni mirrors placed after the choppers removes the last of undesired slow neutrons and functions as converging collimation. The neutrons can be further collimated by finely slitting the beam. The angle of incidence of the beam relative to the reflecting surface can be changed in order to reach higher scattering vectors. A linear He^3 detector with 2 mm resolution positioned 12.38 m from the moderator makes

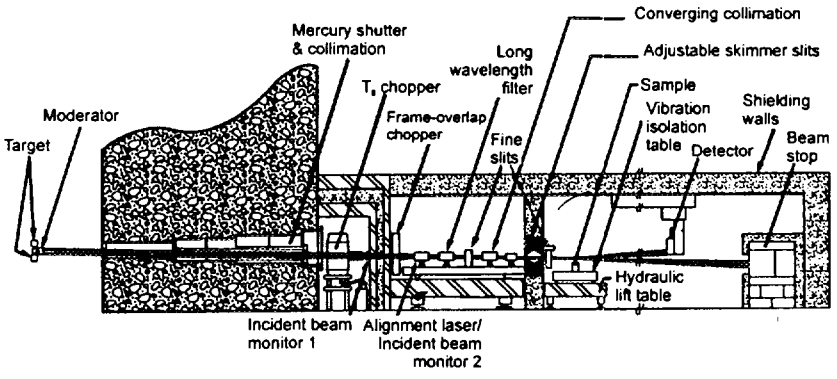

Figure 41. Schematic drawing of SPEAR.

it possible to detect both the specular and off-specular scattering. An advantage of this type of experiment is that there is no moving parts during measurements, hence omitting the possibility for misalignment.

The resolution of the instrument is given by *Q-Resolution*

$$\frac{\Delta Q}{Q} = \sqrt{\left(\frac{\Delta\lambda}{\lambda}\right)^2 + \left(\frac{\Delta\theta}{\theta}\right)^2} = \sqrt{\left(\frac{\Delta t}{t}\right)^2 + \left(\frac{\Delta\theta}{\theta}\right)^2}, \tag{98}$$

where the neutrons arrive at the detector in the time intervals of length Δt, θ is the angle of incidence of the neutrons on the surface, and Q is the length of the scattering vector. For the SPEAR instrument $\Delta Q/Q \approx 3\%$ (cf. p. 38 for the resolution ΔQ at the reflectometer TAS8).

The Shear Cell

The current shear cell allows flow across the quartz crystal in Pouseuille geometry, i.e. the solution is kept between to parallel plates (the quartz surface and the Teflon enclosure). It provides a flat solid-liquid interface ideal for reflectometry. Figure 42 and 43 shows the solid-liquid shear cell used for the measurements originally developed by *Baker et al.* [13] for reflectometry and "over-the-horizon" SANS investigations of the surface induced ordering of charged thread-like micelles of the cationic surfactant cetyl-trimethylammonium 3,5-dicholcrobenzoate (see *Hamilton et al.* [47, 48]). *Pouseuille Geometry*

A set of design criteria has been met with the present cell [13, 48]: Firstly, the flow is pulseless, laminar, and fully developed over the illuminated area. These requirements ensure steady shear in the illuminated part. It is particularly important for modeling purposes to ensure that turbulence is not encountered. Independent of the fluid is Newtonian or non-Newtonian[4] the shear rate can be controlled by the rate of fluid flow through the cell and the thickness of the "test section" through which the fluid flows. *Design Criteria*

The volume flow rate of the cell, Q_{flow}, is measured by circulating water through the cell at room temperature. For non-Newtonian fluids, the viscosity μ changes with shear rate (phenomena know as *shear-thinning* or *shear-thickening*), and thus leads to a complex relation between the two. Therefore, other studies only estimates the shear stress $\tau = \mu(du/dz)$, where u is the component of the velocity

[4]For a fluid in general the viscous stress is proportional to the rate of shearing strain (angular deformation rate): $\tau = k|du/dy|^{n-1}du/dy = \mu du/dy$, where k is called the consistency index, $\mu = k|du/dy|^{n-1}$ the apparent viscosity, and n the flow behaviour index. For a Newtonian fluid $n = 1$ and $k = \mu_{\text{abs}}$, where μ_{abs} is the absolute viscosity[38]

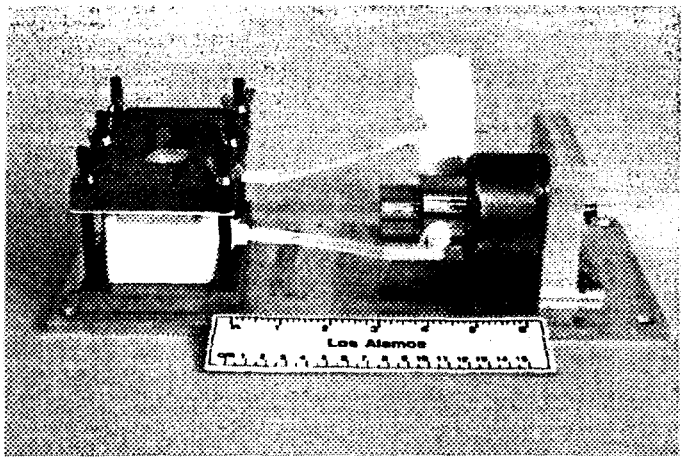

Figure 42. The shear cell. From the pulseless gear pump at the far right the solution is pumped to the cell via Teflon tubes. The fluid enters through the bottom tube and exit at the top after having passed the quartz crystal. A reservoir is connected to the inlet of the pump and effectively removes bubbles from the solution. The gear pump is connected to a motor controller (not shown), which makes it possible to control the flow rate. The whole arrangement is placed in a temperature controlled enclosure (not shown) for the measurements. The enclosure has two windows which allow the neutrons to enter and exit from the enclosure without attenuation.

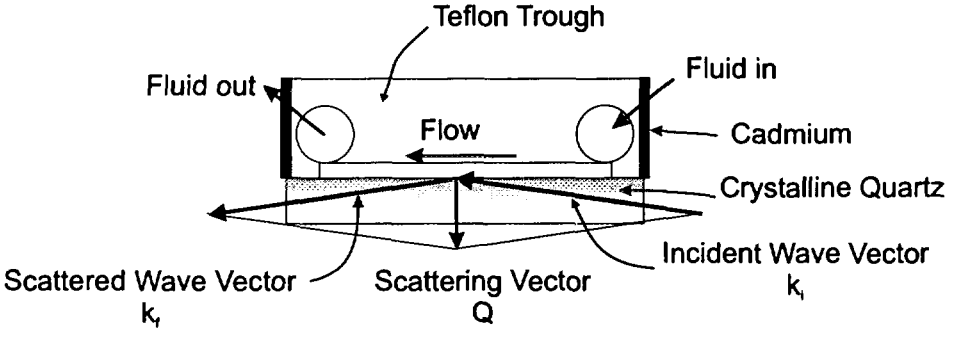

Figure 43. Schematic drawing of the shear cell with Pouiseuille geometry.

parallel to the surface. The surface normal is parallel to z. Matters become complicated by the fact that the flow velocity at the surface changes abruptly. The velocity profile is parabolic for Newtonian fluids, but attains a more square profile (*plug-motion*) for non-Newtonian fluids. Consequently, the flow is here characterized by the average flow rate, $\overline{v} = Q_{\text{flow}}/A$, where A is the cross sectional area of the flow in the channel above the quartz crystal. The flow cross sectional area is $A = 0.336$ cm^2 obtained from a height of $h = 3.05$ cm and depth $d = 0.11$ cm.

Average Flow Rate

5.5 Results

Micelle Formation

The 5 wt % solution of P85 in D_2O was injected into the shear flow cell at a temperature of 10°C, where P85 is present as unimers in solution to ensure no pre-alignment of the sample. The sample was heated at a rate of 0.12 °C/min in order to reach the micellar region of P85. Figure 44 shows two reflectivity profiles measured at temperatures of 47°C and 61°C.

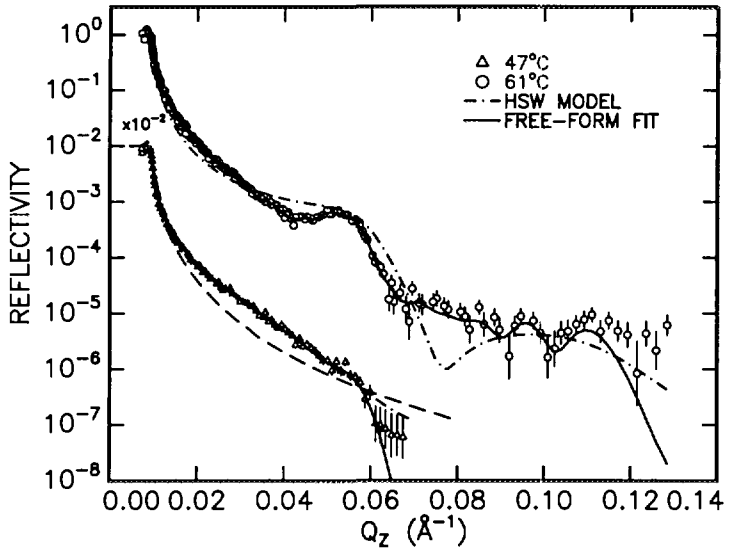

Figure 44. Comparison of the reflectivity scans for two temperatures (47° C and 61° C) in the micellar phase. The features in the 61° C scan already depart from the hard-sphere like ordering and indicate the onset of a more ordered phase at the surface of the quartz crystal. The 47° C scan is depicted along with the Fresnel reflectivity from a sharp interface (dashed curve). Also the fits from the hard-sphere-hard-wall (HSW) ordering and free-form analysis are shown.

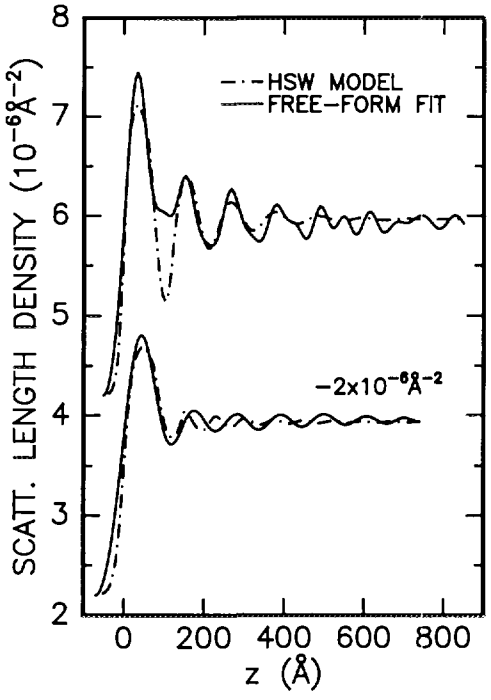

Figure 45. The corresponding scattering length density profiles obtained from the hard-sphere-hard-wall (HSW) (with tethered chains) and free-form fit. The lower and upper part depict the scattering length densities corresponding to the 47 ° C and the 61 ° C measurements, respectively. The lower curves has been displaced by 2×10^{-6} $Å^{-2}$.

The scattering pattern of the two scans deviates significantly. At 47°C, the broad peak, which can be interpreted as micellar hard-sphere ordering at the surface, is only slightly different from the Fresnel behaviour. This is expected since the density of micelles ordering like hard spheres at a hard wall only shows few low amplitude oscillations with respect to the bulk average value for a volume fraction $\eta \approx 0.1$, corresponding to a 5 wt % solution (cf. Figure 38 of Chapter 4). In contrast, the 61°C reflectivity profile shows a more distinct peak at $Q = 0.056$ Å^{-1}. Furthermore, there is an indication of a faint second order peak.

Distinct Peak at 61 °C

In order to gain more quantitative information of the ordering, the reflectivity profiles were fitted by the micellar model with tethered chains developed in Chapters 3 and 4. From Figure 45 it is evident that the model is not able to reproduce the distinct features of the 61°C scan. It is known from Chapter 3, that only a hard-sphere volume fraction close to the crystallization value is able to reproduce a profile reminiscent of the measured reflectivity profile. Therefore, the best fit to the profile has a hard-sphere volume fraction of $\eta = 0.38$. It appears that the structure is more well-ordered than can described by hard spheres at a hard wall. Hence, surface association corresponding to a higher concentration than the bulk is already initiated at 61°C.

Micellar Model

To further elucidate the discrepancy between the hard-sphere model and the data, free-form profiles with cubic b splines as basis functions were obtained according to the procedure outlined in Chapter 3. Figure 45 shows a comparison between the scattering length density profile of the best hard-sphere and the free-form fit for both temperatures. As with the micellar ordering the profiles can be interpreted as a D_2O rich inner layer with a subsequent layering. The decaying oscillations indicate increasing disorder with increasing distance from the quartz surface and the uniform level is representative of the bulk solution. The first oscillation of the both scattering length density profiles exceeds the scattering length density of D_2O ($\rho_{D_2O} = 6.4 \times 10^{-6}$Å^{-2}), the highest permissible value in the system. However, the profiles can be justified by noting that the free-form method can overestimate the scattering length density depending on the truncation of the scattering vectors and how sharp the features of the real density profile is.

Free-Form Profiles

Unphysical Values of the Scattering Length Density at 61° C

The slight difference between the 47°C reflectivity curve (the lower half of Figure 45) and the Fresnel behaviour results in a large uncertainty of the oscillations after the initial peak. Therefore, we see a discrepancy in the scattering density profiles of the hard-sphere model and the free-form determination.

In order to parameterize the free-form density profiles, a decaying oscillatory function were fitted to the data on the form:

Paramerization of the Free-Form Profiles

$$\rho(z) = 1 + \rho_0 \exp[(z - z_0)/\xi] \sin[\frac{2\pi(z - z_0)}{d}], \tag{99}$$

where ξ is the decay length, d the period, ρ_0 the initial amplitude of the oscillations, and z_0 the starting point of the oscillations. The starting point was chosen at the first maximum after the initial peak. In Table 12 the obtained results are summarized.

Despite the fact that no hard-sphere fit was obtained for 61°C and the reflectivity curve only had a small deviation from the Fresnel behaviour at 47°C, the periodicities ($d \approx 2R_{HS}$) in Table 12 agree within the resolution of the experiment. The repeat distance is close to the expected diameter of micellar aggregates, which enforces the hypothesis that the ordering is indeed caused by adsorbing aggregates and is not a lamellar ordering. The large uncertainty in the determination of the decay length is the main reason for the larger value at $T = 47$°C when compared to $T = 61$°C. The extent of the ordering can be estimated from the decay length to be approximately 2-3 ordered layers on the surface. The hard-sphere interaction radius, R_{HS}, increases with temperature as also seen in micellar ordering at higher concentrations (cf. Chapter 2).

Model HSW	T (°C)	η	R (Å)	R_{HS} (Å)	σ_{surf} (Å)
	47	0.10	32	52	12.5
	61	0.38	33	56	12
Free-Form	T (°C)	ρ_0 (10^{-6} Å^{-2})	z_0 (Å)	d (Å)	ξ (Å)
	47	0.115±0.004	248	107.1±0.2	290±14
	61	0.41±0.02	210	116.7±0.6	223±20

Table 12. Results from the micellar phase of the 5 wt % solution of P85 in aqueous solution. The obtained results from the micellar model consisting of solid spheres with tethered chains and the fitting of a damped harmonic function to the free-form scattering length density profiles at static conditions are compared.

These findings indicate, that the micelles already at 61°C are slightly anisotropic which causes the micelles to order strongly at the surface. From the free-form profile and the model of *Matsuyama et al.* [82] one could suggest that the found ordering correspond to that of rod-like micelles packing at the surface, i.e. similar to a nematic phase with the director parallel to the surface. From the decaying oscillations of the profile the nematic ordering at the surface gradually transforms into the isotropic state of the bulk.

Nematic Surface Ordering?

The High Temperature Phase

The peak close to $Q = 0.056$ Å^{-1} at 61°C sharpens additionally as the temperature exceeds the sphere-to-rod transition at 70°C [94, 122]. Figure 46 shows the neutron reflectivity data taken at 72°C. Both an intense first and a second order peak can be identified at $Q = 0.057$ Å^{-1} and $Q = 0.112$ Å^{-1}, respectively, revealing a well-ordered layering perpendicular to the surface. This result may imply that the ordering has transformed from anisotropic aggregates to a lamellar structure driven by the increased hydrophobicity of ethylene oxide chains. Consequently, the data have been analyzed using the free-form method of *Pedersen & Hamley* [106] with firstly sine/cosine and secondly cubic b spline functions as basis sets.

Free-Form Analysis: Sine-Cosine Functions. In this approach, the scattering length density profile can be expressed in terms of sine/cosine functions [106, 124]:

$$\rho(z) = a_0 + \sum_{j=1}^{N_{sin}} a_{sin,j} \sin(j2\pi z/z_{max}) + \sum_{j=1}^{N_{cos}} a_{cos,j} \cos(j2\pi z/z_{max}). \quad (100)$$

The method is known to produce reliable results for periodic or nearly periodic structures [106]. The procedure for this type of free-form determination is:

Fitting Procedure

1. From the observed Bragg peaks of the reflectivity curve, Q_{peak}^{obs}, the refraction-corrected positions are obtained from

$$Q_{peak} = \sqrt{(Q_{peak}^{obs})^2 - (Q_c)^2}, \quad (101)$$

where Q_c is the critical scattering vector. The periodicity, d, is obtained from $Q_{peak} = 2\pi n/d$, where n is an integer.

2. An initial value of the total thickness of the $\rho(z)$ profile, z_{max}, is then used to determine the number of terms in sine/cosine series

$$N = N_{cos} = N_{sin} \approx \frac{z_{max}}{d}. \quad (102)$$

3. To obtain an integer valued number of periods, P is rounded up to the nearest integer and z_{max} is adjusted accordingly; $z_{max} = Pd$.

4. Only the terms in the expansion $j' = jP$ should be considered in the sine/cosine expansion. Here, j is the order of the Bragg reflection.

The period, d, was for the 72°C data found to be 111 ± 1 Å. The total thickness was chosen to $z_{max} = 2673.6$ Å, which corresponds to $P = 24$. Note, that from the analysis it was found that more than 20 sine/cosine functions (20 layers) has to be used in order to give the right sharpness of the high-Q edge of the first Bragg reflection at 0.057 $Å^{-1}$. This number of functions gives, furthermore, the amplitude of the oscillations within acceptable physical limits. The determination of the total thickness, z_{max}, of the profile (see *Pedersen and Hamley* [106] and *Thomas* [133]) is an often occurring problem in the analysis of reflectivity data: The choice of z_{max} greatly affects the amplitude of the periodic oscillations in the profile. A large z_{max} gives a smaller amplitude. However, z_{max} can be constrained to a certain extent by looking at the width of the occurring peaks in the reflectivity profile as mentioned above. For the first step of the analysis, both sine and cosine terms were used with $j = 24, 48$, i.e. $N = N_{sin} = N_{cos} = 48$. The result is depicted in Figure 46.

Determination of the Total Thickness of the Profile

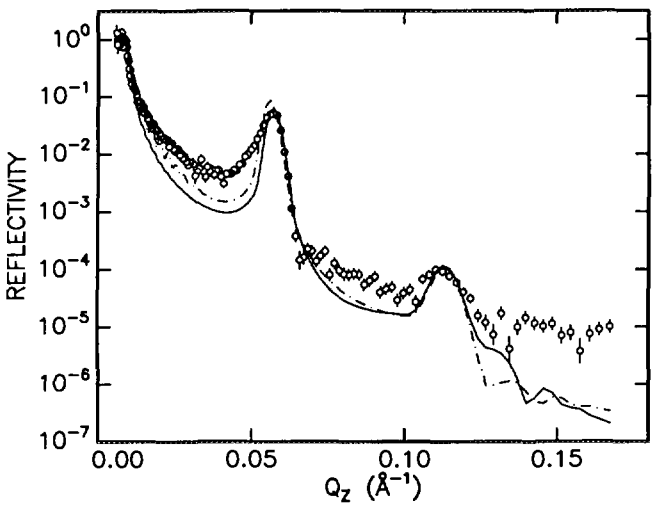

Figure 46. The sine/cosine free-form fits to the reflectivity profile at 72° C. Only two sines and two cosines are included in the series for $\rho(z)$. The dash-dotted curve correspond to the lower profile in Figure 47.

Two profiles reproduced the peak intensities depending on whether the initial average of $\rho(z)$ (a_0 in eqn. (100)) was set to unity or zero. Both profiles have plausible explanations. We remark that P85, PO, and EO has a scattering length density close to zero ($\rho \approx 0.4 \times 10^{-6}$ $Å^{-2}$) and that the scattering length density for D_2O is $\rho_{D_2O} \approx 6.4 \times 10^{-6}$ $Å^{-2}$. The upper profile of Figure 47 can thus represent a pure water layer at the surface of the quartz crystal with a subsequent layering of alternating pure water and copolymer layers. In contrast, the lower profile has an almost pure copolymer layer at the surface with alternating layers of a water rich and a copolymer rich part. The copolymer rich layer might contain only the PO block of the copolymer, whereas the water rich layer is likely to be a mixture of EO and water. The scattering length density of the upper profile is questionable since it does significantly exceed the scattering length density of water.

Two Interpretations of The Data

In both cases, a large part of the scattering is still missing in the fit to the

The Discrepancy in Intensity

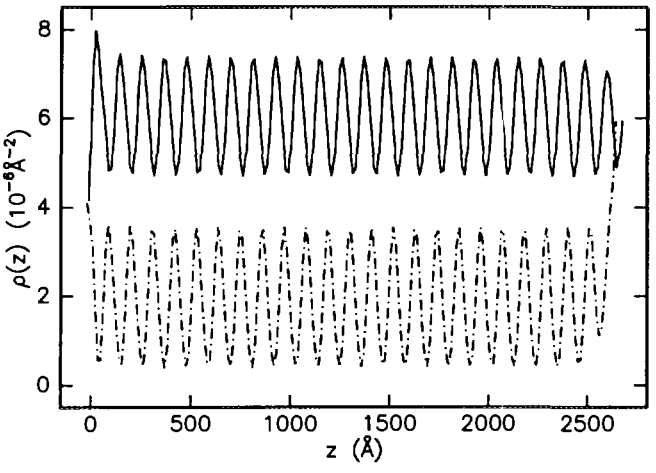

Figure 47. The sine/cosine free-form scattering length density profile $\rho(z)$ corresponding to the curves seen in Figure 46.

reflectivity data. This is a clear indication of the need for additional terms in the scattering length density expansion. The intensity hints at an additional decaying oscillatory component in the scattering length density profile analogous to what is seen for the hard-sphere ordering at a hard wall. Therefore, a second analysis was tried with splines as basis functions in the expansion of the scattering length density.

Free-Form Analysis: Cubic b Splines. A free-form analysis was performed of the data using splines as basic functions for the scattering length density $\rho(z)$. As with the periodic approach two types of profiles were found to appear. One type of profiles (not shown here), which all had an inner water-rich layer, showed a damped oscillatory behaviour of the scattering length density. However, the profiles did exceed by far the scattering length density of water. These profiles correspond to the upper solution of Figure 47.

Free-Form Profile with Plausible Interpretation

The full curve of Figure 48 shows a fit to reflectivity curve measured at 72°C and the insert the corresponding scattering length density profile. This profile corresponds to the lower solution of Figure 47 and has a plausible physical interpretation: A dense polymer layer forms close to the surface and the subsequent almost regular amplitudes signify a periodic layering of alternating highly ordered water-rich and polymer-rich layers as explained previously. As the distance from the surface of the quartz crystal increases, the layers gradually become disordered evident from the decreasing amplitudes of the profile and reach the corresponding value of the isotropic bulk solution at the highest z values. The ordering can arise from both a nematic ordering of rod-like micelles with the director parallel to the surface and a lamellar structure. We believe that the ordering is of the lamellar type, since ordering of rod-like aggregates would inherently be more disordered with more solvent interpenetrating, i.e. result in smaller amplitudes of the profile.

From the present findings, it can not be unambiguously determined whether the ordering arises from layering of anisotropic aggregates or a lamellar structure. Therefore, shear measurements were performed in order to obtain additional knowledge about the surface structure. From the shear alignment seen in the bulk, it was hoped that the surface ordering could be extended further out into the bulk by applying a shear field. Tentatively, this may explain the change to a nematic phase seen in the bulk as a surface mediated ordering.

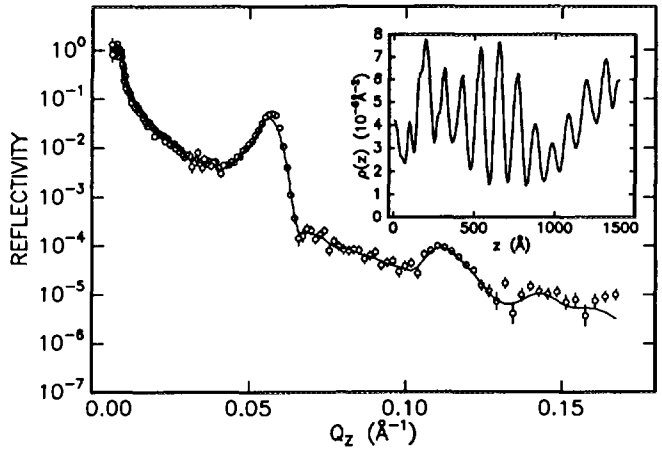

Figure 48. The reflectivity profile for P85 in a 5 wt % solution at 72° C. The insert shows the free-form fit to the reflectivity profile.

Shear Measurements

The next section concerns the attempts to further order the sample by applying a shear field with velocity gradient perpendicular to the surface. Figure 49 displays the response in the reflectivity to continuous shear at an average flow rate of approximately 60 mm/s. Surprisingly, the peaks have vanished and thereby the regular ordering perpendicular to the surface. The reflectivity response is hardly different from the Fresnel reflectivity of a sharp interface. To discern whether the static structure is composed of rod-like micelles or a lamellar structure, it is important to see whether the highly ordered phase reappears after cessation of the shear.

Featureless Response to Shear Field

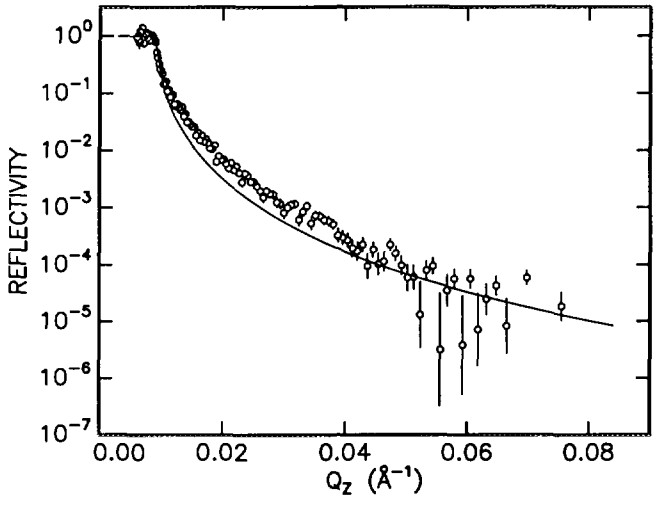

Figure 49. Reflectivity profile for the initial shear run at a temperature of 71 °C. The average flow rate is 60 mm/s.

If the order reappears almost instantly, it is likely that the disorder is caused by the tumbling instability occurring in nematic solutions of worm-like micelles, which has been reported for low shearing fields ($\dot{\gamma} \approx 1\ s^{-1}$) [15, 22, 119]. Tumbling arises when the director cannot find a preferred direction and is assumed to rotate

Tumbling Instability

indefinitely in the shear field. Director tumbling may destroy a nematic surface ordering.

Second Static Measurement at 71° C

The solution was subsequently cooled below the sphere-to-rod transition (66°C) and reheated. Figure 50 shows the reflectivity curve at 71°C after reentering the rod-like phase. The scattering pattern had changed shape with a peak of significantly decreased intensity compared to the initial 72°C reflectivity curve. The free-form profile shows the possible formation of a water rich layer closest to the quartz surface with subsequent slight oscillations rendering an intermixing between the water and the polymer layers. From the oscillations a period of $d = 108$ Å was obtained.

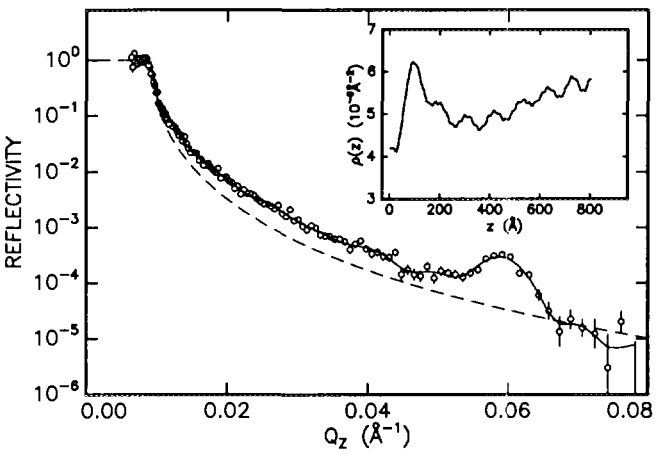

Figure 50. The reflectivity profile for P85 at 71° C after the initial shear run and cooling to 66° C. The insert shows the free-form fit to the reflectivity profile.

Measurements at Higher Flow Rates

Figure 51 shows attempts to shear align the sample at higher average flow rates of 160, 250, and 330 mm/s. No ordering reappears at any shear rate. Free-form analysis of the profiles (see Figure 53) shows that the profiles can be interpreted as water interpenetrating the surface ordering (upper profiles) or a collapse of polymers on the surface with the highest content of water at the surface of the quartz crystal. These measurements speak against the occurrence of a tumbling transition, but enforces the hypothesis of a lamellar (multilayered) structure. In case of a lamellar structure, the shear field might have transformed the triblock copolymers into a highly entangled layer not allowing water to penetrate through the destroyed structure to reform the well-ordered lamellar structure. It might form over time. For rod-like micelles, time effects can be ruled out due to the fast response seen in the SANS measurements. Furthermore, the rods are capable of withstanding higher shear stresses in Couette flow without breaking apart, so it is not likely that the rods are simply destroyed by the shear. These findings speak for an initial lamellar structure at 72°C.

In view of the SANS measurements, the bulk is expected to relax back to the isotropic phase seconds after the shear is discontinued. Consequently, if the nematic surface ordering is transformed into the isotropic phase by the shear field, a return of the nematic phase is expected in time. A last attempt to reproduce the highly ordered scattering pattern was tried by cooling the solution to approximately 5°C, where the triblock copolymers are present as unimers in solution. The solution was kept at 5°C several hours allowing the copolymers to desorb from the quartz surface before reheating to the rod-like phase.

Third Static Reflectivity Measurement after Cooling Cycle

The lower part of Figure 53 shows the reflectivity profile after reheating to 71°C. Apparent is the lack of intensity compared with the initial scan at 72°C.

The corresponding free-form profile (see Figure 54) show that the ordering has not fully recovered from the shear treatment due to the lower amplitudes of the density profile. The average period obtained from the peaks in the profile is $d = 106 \pm 3$ Å, which is significantly lower than the initial periodicity of $d = 111 \pm 1$ Å obtained at 72°C. The change between the two scans may be related to the amount of water in the PEO containing layers of a lamellar surface ordering. Depending on the heating rate, the amount of water in the lamellar structure may be different, thus resulting in a changed periodicity. The main result is that the triblock copolymer ordering appears to have recovered partially to the pristine appearance.

5.6 Discussion

In summary, the triblock copolymer P85 shows a strong surface-induced ordering, when the solution (5 wt %) is heated towards the sphere-to-rod transition occurring close to 70°C. Surface induced ordering is initiated already at 61°C in the bulk micellar phase, hence prior to the sphere-to-rod transition. As the sphere-to-rod transition is surpassed, both a first and second order peak appear in the reflectivity profile. Free-form analysis indicates a transition from spherical micelles to a lamellar ordering possibly with an intermediate surface association of anisotropic aggregates (see Figure 55). The application of shear destroys the surface ordering, which is only recovered partially when the solution is kept at 5°C for two hours and then reheated.

The micellar model revealed that even though it was capable of fitting the 61°C scan, the hard-sphere volume fraction was found to be considerably higher

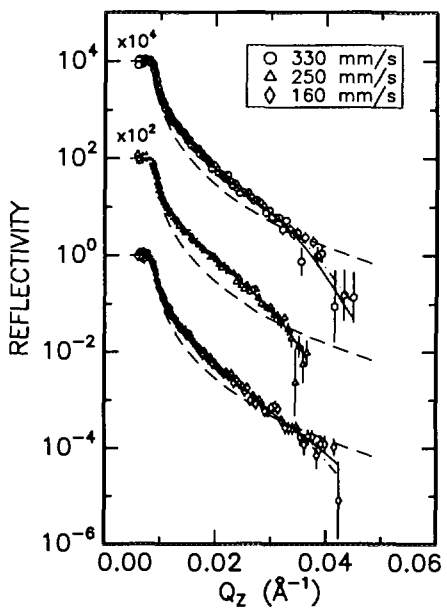

Figure 51. The response of the solution to shear at three different shear rates: 160, 250, and 330 mm/s as seen with reflectivity. Only a broad peak is observed marking the disorder of the sample. The dash-dotted curves correspond to the lower ρ-profiles in Figure 52 and the full curve the upper ρ-profiles.

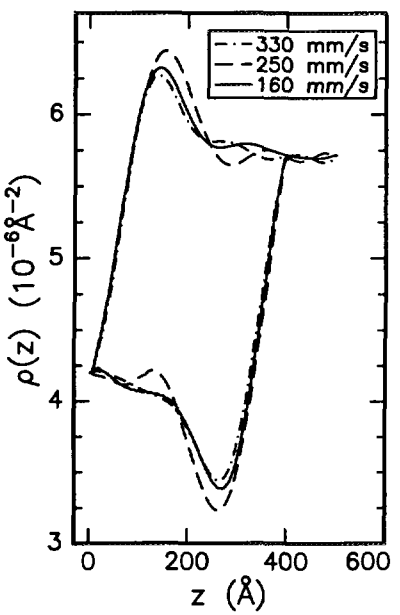

Figure 52. The free-form scattering length density profiles for the three different shear rates: 160, 250, and 330 mm/s.

(η = 0.38) than the expected bulk value (η = 0.1). Hence, a transition is occurring at the surface before the bulk changes happen. Assuming that the ordering is due to an elongated micellar shape, the modeling of *Matsuyama et al.* showed a transition from isotropic to nematic ordered rods at the surface at lower concentration than the bulk isotropic-nematic transition. Moreover, it was found that the more unfavourable the solute-solvent interaction became, the higher the surface concentration of the adsorbed rods. It does support the findings from the present chapter, since the very unfavourable solute-solvent interaction would favour a high concentration of copolymer at the surface. It is, therefore, likely that the surface adsorbed rods initiates growth of the subsequent layering. A decaying oscillatory function fitted to the free-form scattering length density profiles reveals a period of 116±1 Å at 61°C, which is close to twice hard-sphere radii seen in the micellar phase. This implies that the rods with a micellar core are packed parallel to the surface (see Figure 55).

As the temperature is increased, the ethylene oxide becomes increasingly hydrophobic and as the sphere-to-rod transition is approached no water molecules are any longer hydrogen bonded to the CH-segments of the ethylene oxide chain. *Linse et al.* [73] ascribed this change to a transition from a polar state to less polar state at higher temperatures (see the introductory chapter), thus making the solvent-solute contacts less favourable. The same change is seen in the SANS measurements by *Mortensen and Pedersen* [94], where a transition from micellar to a rod-like shape has been reported. In these measurements, the distance distribution function showed no region related to micellar-micellar interaction effects,

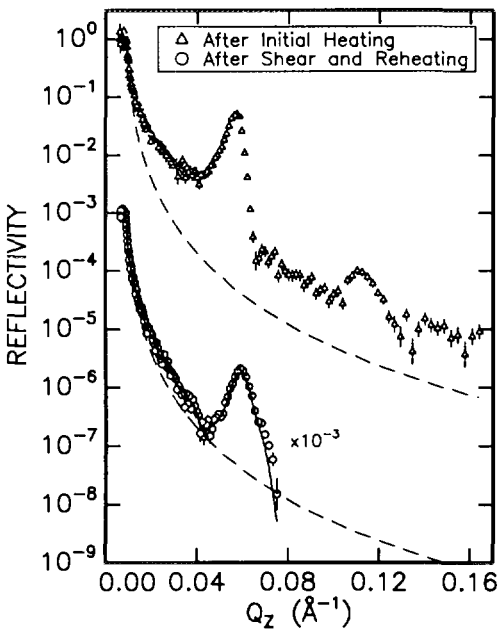

Figure 53. Comparison of the reflectivity profiles above the sphere-to-rod transition. The upper part depicts the initial scan and the lower part the profile after cooling at 10 °C. The full curve is the free-form fit depicted in Figure 54

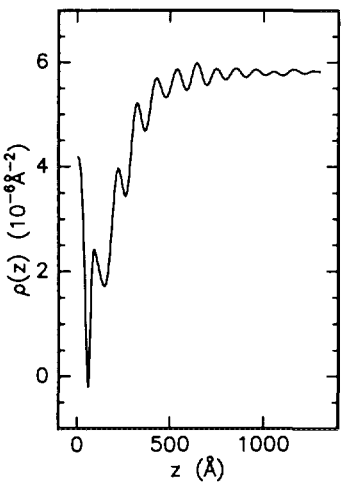

Figure 54. The free-form ρ profile to the lower reflectivity curve in Figure 53. The decaying oscillations imply a highly ordered surface layer with a subsequent increasing disorder. A lamellar structure is the more likely candidate for the surface ordering.

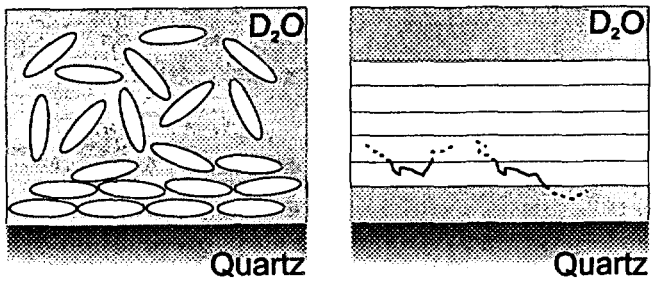

Figure 55. The two likely surface structures of the triblock copolymer in the high temperature phase. In the lamellar phase (right) the white areas signify propylene dense layers between layers of water and ethylene oxide. Two triblock copolymers are drawn; the dashed part is the ethylene oxide blocks and the full line the propylene oxide block.

when the sphere-to-rod transition was surpassed signifying a "collapse" of the PEO chains on the surface of the PO core. Because D_2O is not a good solvent for PEO at this temperature it would also introduce an attractive component in the micelle-micelle interaction. We suggest a transition from aggregates which surface associate to a "collapse" of the polymers on the quartz surface. It is plausible that the effect is driven by the decreased hydrophilicity of the ethylene oxide chains. The change in ordering is marked by a change from a water rich layer at the surface to a polymer dense layer.

The multilayered structure can result from the less favourable solute-solvent interaction which favours a smaller exposed area to the solute. Hence, in the limit where curvature $\kappa = 1/R$ tends to zero, a lamellar structure is formed. It appears to be favourable for the aggregate to decrease the surface area and thus decrease the contact with water. In the extreme limit, the structure favours zero curvature, a lamellar structure. In addition, a lamellar structure can be initiated by an enthalpic favourable adsorption of EO on the surface silanol groups. In bulk polymer solutions there exists a phase separation for temperatures below θ into two phases, one that contains almost pure solvent and the other that has the polymer solution [131]. The cosine/sine free-form analysis indicates that it is actually happening for this system. The highly hydrophobic chains collapse in other words to the surface with the innermost copolymers hydrogen bonded to the silanol groups of quartz. The SANS data in the region signifies the large changes in solvent quality of D_2O for the ethylene oxide. The depletion zone in the pair correlation function disappears, signifying a transition from a hard-core repulsion to an almost negligible interaction.

In view of the shear behaviour a surface segregation as lamellae is likely. Furthermore, the surface ordering of rods does not agree with the consistent disappearance of order when continuous shear is applied. A 4 wt % solution in the rod-like phase had a response time of seconds after the shear was discontinued changing the order from nematic to isotropic. Moreover, the aggregates did not break apart for shear rates up to 1000 s^{-1}. After cessation of the shear it is expected that the surface ordering of the rods will reappear, unless the adsorbed structure of adsorbed copolymer/aggregates have changed significantly. The response to continuous shear was a featureless scattering pattern which only showed a slight departure from the Fresnel reflectivity from a sharp interface. Effects like tumbling instability, seen at low shear rates, would explain the observed behaviour, but also imply a recurrence of the initial reflectivity profile. Higher shear rates did not produce a higher degree of ordering. Only after a prolonged cooling at 5°C did peaks reappear in the scattering pattern when the sample was reheated to the rod-like phase. This strongly suggest an incipient phase separation in form

of a multilayered structure (lamellar) which by the shear is destroyed and transformed into strongly entangled triblock copolymers. However, since the triblock copolymers are mobile a restraint on the movement must be implied.

The bulk and the surface response to shear disagrees. The *log-rolling* of the rods are consistent with both measurements. This type of response have recently been seen in a hexagonal phase under shear [117]. The director of the aggregates should then change from parallel to perpendicular to the surface.

6 The Crystalline Phases

From the presented micellar model it is evident that a close relation exists between the ordering of P85 micelles and hard spheres. The volume fraction of the hard spheres effectively determines the structure of the ordering. Low volume fractions have a classical liquid ordering, but as the hard-sphere volume fraction surpasses a threshold value, η_c, a disorder-to-order (*Kirkwood-Alder* [2]) transition occurs ordering the hard spheres into face-centered cubic (FCC) arrays. The transition was first observed by computer simulation by *Alder et al.* [2] and experimentally in colloid systems by *Pusey et al.* [111]. In general, the order-to-disorder transition has been found to occur for spherical systems with purely repulsive interactions. Both FCC and body-centered cubic (BCC) orderings have been observed for di-block copolymer systems [39, 84] depending on whether the repulsive interactions are short or long range, respectively.

Hard-Sphere Disorder-to-Order Transition

From SANS measurements of P85 micelles in aqueous solution *Mortensen et al.* [89, 95] and *Mortensen & Pedersen* [94] found, that the micellar liquid undergoes a first-order transition into a body centered cubic crystal as the micellar volume fraction exceeds a critical value of η_c=0.53. By shearing the polycrystalline sample in a Couette type shear cell [88], a single crystal was formed with true long range order in the "bond-angle" correlation, but had only liquid-like "bond-length" correlation. The former had a magnitude of the sample size, but the latter was found to be approximately 400 Å, a few cubic lattice constants. The Bragg reflections from the cubic crystal, as observed with SANS measurements, had a Lorentzian rather than a Gaussian line shape. The BCC structure of the micelles occurs due to relatively soft part of the potential arising from the dissolved ethylene oxide chains of the micelle. This structure does not change with temperature. A transition to a FCC structure could be expected as the potential becomes steeper, more hard-sphere like, with an increase in the hydrophobicity of the ethylene oxide. This is due to the fact that the ethylene oxide effectively contracts as the solvent quality becomes poorer with temperature.

BCC Micellar Crystal

The BCC micellar phase transforms by another first order transformation into a liquid-like phase of more elongated shaped micelles (rods) around 60 °C depending on concentration. The liquid phase is only present in a temperature range of a few degrees, where-after the rods order in a highly viscous hexagonal lattice, which likewise can be transformed into a single crystal by application of shear [88].

Hexagonal Lattice

In light of the interesting shear induced long range order of the aggregates at higher concentrations, the effect of the presence of a surface on the ordering is investigated in this chapter. *Groot et al.* [45] found from Monte Carlo simulations that hard spheres show indications of crystallization in hexagonal pattern at a hard surface before the bulk crystallizes. Speculatively, the crystalline order could be mediated from the surface and into the bulk solution. The P85 system is ideal for this type of investigations as the temperature provides a handle on the bulk phase and the interaction potential between aggregates by the changing hydrophobicity of ethylene oxide with temperature. The aim of the present chapter is to investigate the surface induced ordering of the micellar cubic phase of P85 at the hydrophilic surface of single crystalline quartz.

The Effect of the Presence of a Surface

6.1 Experimental

Sample preparation

The Pluronic P85 (30 wt %) was dissolved in D_2O at a temperature of 5°C. The solution was left to equilibrate at the same temperature for at least two days before

the measurements because of the high viscosity of the large weight fraction of the copolymer in solution. Prior to injection of the triblock copolymer solution a run with D_2O at room temperature was performed to check that the surface of the quartz single crystal was clean and to check the purity of the solvent. The triblock copolymer was injected at 10°C, where P85 is present as unimers in solution. This treatment should ensure that no preshearing and thus alignment of the sample occurred. Subsequently, the heating was started at a typical rate of 0.3 °C/min and scans performed when the temperature had stabilized to be within ±0.1°C of the desired temperature.

Neutron Reflectivity

As specular reflectivity probes the ordering along the surface normal, the technique is highly sensitive to periodic arrangements originating from e.g. lamellae, BCC, FCC or Hexagonal Closed Packed (HCP) lattice planes ordering parallel to the surface. A drawback in general for specular reflectivity is the limited knowledge which can be gained on the in-plane ordering. To obtain this type of information grazing-incidence-diffraction has been used as e.g. in the study of lipids at the air-liquid interface [10, 52, 112]. The current solid-liquid cell and the inability to move the used single detector out of the scattering plane prohibits this type of measurements. Knowledge of the in-plane ordering can be obtained from the off-specular scans which only probe a narrow region around the specular direction. However, quantitative information is hard to obtain from the diffuse scattering from many-component systems.

Limited Knowledge of the In-plane Ordering

For the reflectivity measurements at the reflectometer TAS8 (see Chapter 3) three different symmetrical aperture settings (0.3, 0.5, 1.0 mm) were used to allow for larger flux at higher scattering vectors. As with the micellar liquid phase the background was found to be highly structured and its subtraction had to be performed with caution; between the Bragg peaks the specular signal could hardly be discerned from the background level. The reproducibility of the reflectivity measurements was investigated by performing independent runs with a shallow (5 ml) and a deep (15 ml) cell with a depth perpendicular to the quartz surface of 1 and 3 mm, respectively. Furthermore, both pure D_2O and a D_2O/H_2O-mixture contrast matched to quartz were used to provide additional information.

Structured Background

6.2 Results

Figure 56 shows a series of reflectivity measurements performed at temperatures representative of the bulk disordered (20°C), BCC (30 and 45°C), and hexagonal (75°C) phases. Except for the lowest temperature, equidistant narrow Bragg-like reflections can be identified indicative of a high degree of order along the surface normal. The scattering patterns are in all cases characterized by an intense and a weak set of reflections.

A transverse scan (rocking curve) through the most intense Bragg reflection at 0.056 $Å^{-1}$ at temperature $T = 45°C$ is depicted in Figure 57. The rocking angle, ω, has been transformed into the in-plane scattering vector, Q_x, by

Transverse Scan

$$Q_x = k[\cos(2\theta - \omega) - \cos(\omega)], \tag{103}$$

where k is the wave number and 2θ the scattering angle. For this transverse scan the Q_z component is constant: $Q_z = 0.056$ $Å^{-1}$. The peak follows a Gaussian line shape with Lorentzian tails. Consequently, it is different from the micellar liquid phase, where a broad diffuse component is superimposed on the specular signal. The Lorentzian tails are likely to be either a diffuse component from roughness in the system and/or it is representative of the bulk order. A Lorentzian line

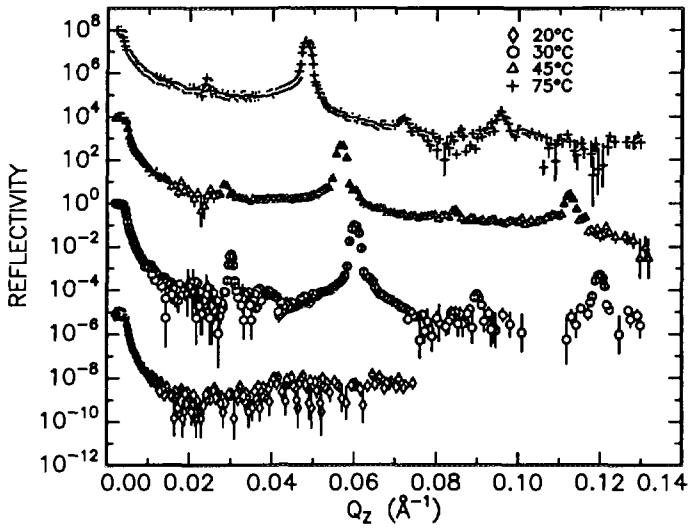

Figure 56. Reflectivity scans at 20, 30, 45, and 75 °C of a 30 wt% P85 solution. Very intense peaks reveal a long range ordering with Bragg like peaks close to being resolution limited. The 20° C scan is below the temperature of the first order bulk transition, where the micellar liquid transforms into a well-ordered BCC bulk structure.

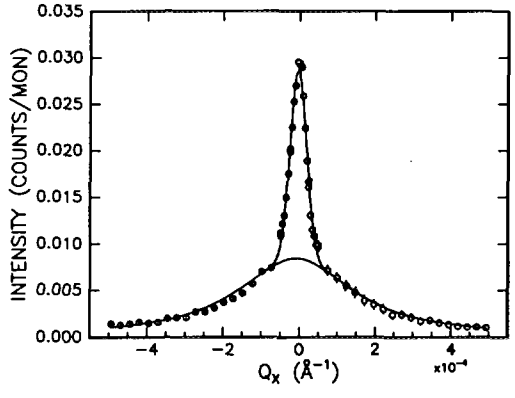

Figure 57. Off-specular scan at the most intense peak at 45 °C.

shape is the result from an exponentially decaying pair correlation function and can thus give information on the in-plane correlation length, $\xi_{\perp}$. The Lorentzian line shape gives a minimum correlation length of 5400 Å ±200 Å. The specular component of the off-specular scan, represented by the Gaussian, represents an even larger correlation length than 5400 Å, because the Gaussian is narrower than the Lorentzian function.

Minimum Correlation Length

Periodicity and Out-of-Plane Correlation Length

Without assumptions concerning the ordering of the triblock copolymer in solution, an estimate for the periodicity and the correlation length can be obtained directly from the scans. The periodicity d is obtained from the positions of the refraction corrected scattering vectors of the Bragg peaks by

Periodicity

$$d = n\frac{2\pi}{Q_n^{\mathrm{cor}}}. \tag{104}$$

In the equation, the refraction corrected scattering vector Q_{cor} is given by $Q_{\mathrm{cor}} = \sqrt{Q_{\mathrm{peak}}^2 - Q_c^2}$, where Q_{peak} is the center of fit to a Gaussian function and Q_c the critical scattering vector. Likewise, an estimate for the correlation length ξ can be calculated from the deconvoluted Full-Width-at-Half-Maximum (FWHM) obtained from the fit according to the formula $\xi = 2\pi/\sqrt{\Delta Q_{peak}^2 - \Delta Q_{res}^2}$. Here, ΔQ_{peak} is the measured FWHM and ΔQ_{res} the resolution FWHM calculated from eqn. 53 of Chapter 3. In Table 13 the averaged value of the periodicity from three independent runs and the estimate of the out-of-plane correlation length are tabulated. The correlation length is close to being resolution limited and varies somewhat for the different peaks of a scan. Consequently, the values given in the table are the average for d and ξ of the most intense and thus well-defined peak. It corresponds in this determination to $n = 2$, but is denoted the first fundamental or main peak as will be explained subsequently.

Correlation Length

Values of the Most Intense Peak

T (°C)	d (Å)	ξ (Å)
30	210±1	11000[5]
45	224±1	8000±1300
75	262±2.5	8000±2000

[5]Only a single scan was performed at this temperature.

Table 13. Periodicities and correlation lengths of the Bragg peaks.

From Table 13 the increasing period with temperature signifies either larger aggregates or more swollen bilayers. The out-of-plane correlation length is on the same order of magnitude as the in-plane correlation length. The correlation length, which for all the scans is beyond approximately 7000 Å, is thus comparable to the "bond angle" correlation length from the bulk SANS measurements [88].

Increasing Period with Increasing Temperature

To gain more insight into the origin of the order, the main peak was measured continuously as the temperature was changed between reflectivity scans. The temperature dependence might give indications of transitions and thus changes in the structure of the triblock copolymer ordering.

Temperature Dependence of the First Fundamental Peak

For each temperature a Gaussian line shape was fitted to the main peak. Figure 58(a) shows the periodicity ($2\pi/Q_{\mathrm{peak}} = 2\pi/Q_{\mathrm{cor}}$ for $Q \gg Q_c$) obtained for the initial heating-cooling circle starting with temperatures in the range from 45 to 75°C at an average rate of 0.3°C/min and subsequent cooling from 75 to 16°C at an average rate of 0.45°C/min. The different symbols indicate separate runs. No difference between the two depths of the polymer enclosures was observed. The hysteresis between the cooling and the heating scan indicates that the polymer solution does not reach equilibrium for each scan with the used heating and cooling rates.

Gaussian Line Shape

Two linear regions are observed in the periodicity for both the heating and cooling between an abrupt transition occurring approximately at 68°C (heating) and 50°C (cooling). The abrupt transition could correspond to the 1. order bulk transition from BCC micellar crystal to the hexagonal ordered rods seen by SANS [88]. However, it is not evident from the periodicity whether or not a region of disordered rods exits. The signature of the liquid of disordered rods is observed

Abrupt Transition

Signature of Liquid Phase

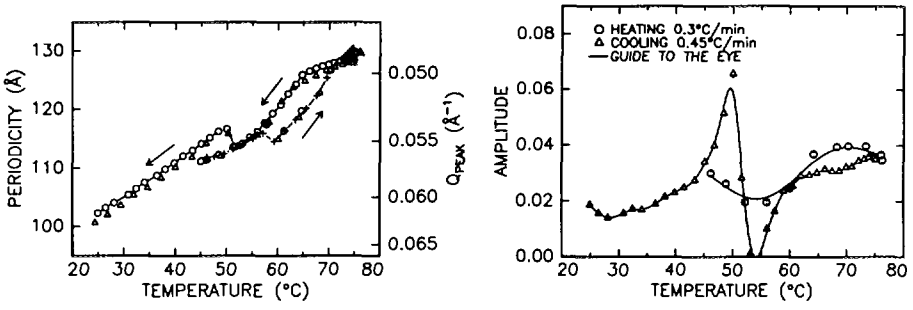

(a) Periodicity ($2\pi/Q_{\text{peak}}$)

(b) Gaussian Amplitude

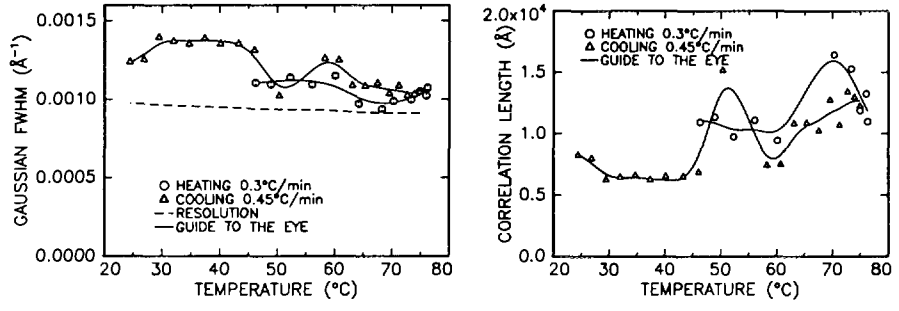

(c) Gaussian Full-Width-at-Half-Maximum

(d) Correlation Length

Figure 58. The periodicity, amplitude, and correlation length as obtained from a Gaussian fit to the main Bragg like reflection as a function of temperature.

in the amplitude of the Gaussian line shape (see Figure 58(b)), which is seen to almost vanish in the vicinity of 53°C. Surprisingly, the trace of the intermediate liquid phase is only seen when the sample is cooled across the transition in spite of the higher cooling than heating rate. The heating of the sample across the transition only shows a slight decrease in intensity. Furthermore, the intensity of the main peak abruptly disappears between 23 and 24 °C in correspondence with the first order bulk transition between the micellar crystal and micelles and unimers in solution.

The measured FWHM, ΔQ_{peak}, from a cooling-heating cycle using the shallow cell, is shown in Figure 58(c) and the corresponding correlation length in Figure 58(d). If the abrupt shift in periodicity is assumed to be due to a phase transition from a micellar crystal to hexagonal ordered rods, then in each of these phases the correlation length is seen to increase (i.e. decrease in FWHM of the main peak) with temperature. In the following section the different possibilities for ordering are analyzed in detail.

6.3 Analysis

Possibilities of Surface Ordering

In brief, the different possibilities of ordering and possible coexistence are:

1. Body-centered cubic, face-centered cubic, or hexagonal close-packed micellar crystals
2. Hexagonal ordered rods
3. Lamellae

The occurrence of the phases are of course temperature dependent and can be different for the surface and the bulk.

Micellar Crystals

Between approximately 24°C and 60°C the most likely structure is ordered micelles in light of the earlier SANS bulk measurement [88, 94]. If at first the low intensity peaks are disregarded, the main peak can originate from either a BCC, a FCC, or a HCP ordering of micelles with either (110), (111), or (002) planes parallel to the surface, respectively. These planes are assumed to have their first allowed reflection at the main peak, Q_{peak}. If the micelles are treated as "giant atoms" with a radius equal to the hard-sphere interaction radius R_{HS}, the radius will in all three cases be given by

Hard-Sphere Interaction Radius

$$R_{\text{HS}} = \sqrt{\frac{3}{2}}\frac{\pi}{Q_{\text{peak}}}. \tag{105}$$

Only the HCP(002) and the FCC(111) are close-packed planes with lattice parameters $c^{\text{HCP}} = 4\pi/Q_{\text{peak}}$ and $a^{\text{HCP}} = \sqrt{3/8}c^{\text{HCP}}$ and $a^{\text{FCC}}_{(111)} = 2\sqrt{3}\pi/Q_{\text{peak}}$, respectively. The more open BCC structure will have a cubic lattice parameter of $a^{\text{BCC}}_{(110)} = 2\sqrt{2}\pi/Q_{\text{peak}}$.

Usually in crystallography, a search for distinct reflections are performed to distinguish between the different structures. However, the solid-liquid cell is constructed for reflection of low angle neutrons to the interface and not for performing crystallography: As only FCC will have an extinct (10l) reflection, a distinction can be made by measuring this reflection. If the FCC(111) planes is assumed to be parallel to the surface of the quartz crystal, the (101) reflection is reached by a least a rotation of 45° of the solid-liquid cell with respect to the incoming neutrons. Unfortunately, the geometry of the solid-liquid cell does not allow neutrons to enter at this angle because of the width of the entrance hole in the thermo-shielding and the thickness of the quartz crystal.

Extinct Reflections

Hexagonal Rods

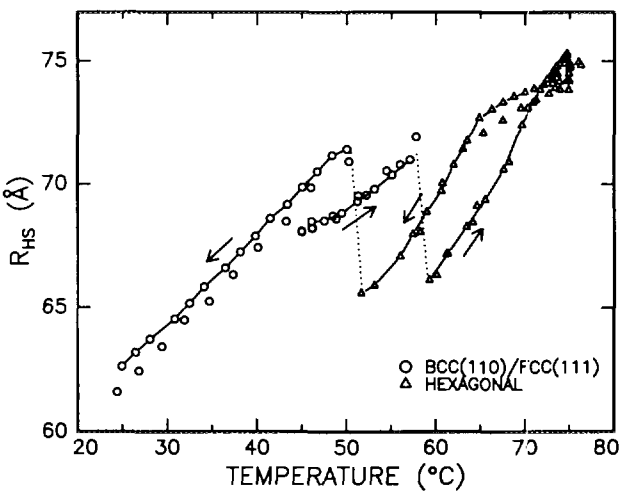

Figure 59. The hard-sphere interaction radius, R_{HS}, as a function of the temperature. Below the discontinuity a micellar crystal has been assumed and above hexagonally ordered rods.

As the temperature is increased a kink is seen in the periodicity in both the heating and the cooling scans (cf. 58(a)). Figure 59 shows the hard-sphere radius calculated from the main peak position as a function of temperature. Micellar crystalline ordering and hexagonal ordering of rod-like micelles have been assumed below and above the kink, respectively. The rods are assumed to pack in a hexagonal array with (11) planes parallel to the quartz surface. Consequently, the hard-sphere radius of the cross-section for the hexagonal packed rods is obtained from the main peak position as

Micellar Crystal Followed by Hexagonal Ordering of Rods

$$R_{\mathrm{HS}} = \frac{\sqrt{3}}{2}\frac{\pi}{Q_{\mathrm{peak}}}. \tag{106}$$

The figure does offer an explanation for the phase transition. As the temperature is risen, the micelles increase in size as also seen in the micellar liquid phase. If the central propylene oxide chain is fully stretched at approximately 53°C, it would be favourable for the micelles to attain an elongated shape. It appears as if the anisotropic micelles disfavour the BCC packing and therefore transform into a more closely packed hexagonal ordering after having passed a liquid-like phase. The transformation can be understood in terms of the decreased hydration of ethylene oxide with increasing temperature. As the temperature rises, the ethylene oxide block contracts correspondingly and is suggested to collapse on the surface of the propylene core at higher temperature. The rods can due to the more attractive interaction between the ethylene oxide chains pack more densely. The reduction in interaction radius R_{HS} at the transition to hexagonal rods is in good agreement with this interpretation. For the rods, the interaction radius R_{HS} of the cross section continues to increase after the transition. The maximum value of the hard-sphere radius obtained for BCC/FCC/HCP phase is exceeded in the hexagonal rod-like phase.

Tentative Explanation of the Kink

Lamellae

A last possibility for the ordering is the formation of a lamellar structure. In effect this formation would be similar to a phase separation between PO and EO. The ordering is seen for higher concentrations of P85 in aqueous solution [93]. In the pristine P85 it was suggested that the formation of lamellae with a 230 Å repeat distance was caused by the crystallization of EO. As 10-20 wt % water was added to the system, the lamellae were found to swell at temperatures below approximately 20°C depending on the concentration. A different type of lamellar ordering is observed for concentrations above 50 wt %, where the hydrophobic PO drives the formation. The repeat distance of the type of lamellae was found to be on the order of 90 Å with a weak concentration and temperature dependence [93]. Tentatively, the presence of a surface gives rise to a higher local concentration of copolymer at the interface initiating formation of the lamellae. Furthermore, the formation of the bulk crystals effectively "binds" water in the structure dehydrating the surface region. This will consequently cause formation of lamellar at the surface.

Two Types of Lamellar Structures

The kink in the periodicity observed in the heating and cooling scans speaks against the formation of only a single, persistent lamellar phase. However, changes in the bulk might have an influence on the surface ordering.

The "Half-order" Peaks

The appearance of a set of "half-order" peaks may indicate a structural component with the double period or may simply be a shadow of the main peak originating from scattered neutrons with wavelength $\lambda/2$. The beryllium filter does allow

$\lambda/2$ Neutrons

up to approximately 1 % of mainly second order reflections through from the pyrolytic graphite monochromator crystal. However, the "half-order" reflections must have an intensity which is a constant fraction of the corresponding main reflections. No strong reflections could be measured at the double scattering vector corresponding to the faint peaks occurring between $Q = 0.07$ and 0.1 Å^{-1} (cf. Figure 56). Moreover, the intensity of the alleged "half-order" peak occurring between $Q = 0.02$ and 0.04 Å^{-1} is temperature dependent and is a varying fraction of the fundamental peak. Consequently, there exists ordering with twice the period, but still intensity from the $\lambda/2$ neutrons cannot be totally neglected at the peak with lowest scattering vector.

To resolve the ambiguous interpretations of the data, detailed modeling is necessary to obtain additional information. Packed planes of micelles with interpenetrating water and lamellae can be regarded as a repeated bilayered stack. Since the total ordering exceeds a thickness of 7000 Å with a repeated layering on the order of hundreds of Ångströms it is advantageous to use the matrix scheme for calculation of the reflectivity commonly used in optics [17]. The matrix formalism is in principle identical to *Parratt*'s method [102]. However, for periodically stratified multilayers of large extent it offers a more convenient way of exact calculating the reflectivity. In the following this method is used for analysis of the reflectivity curves and in a more detailed investigation of the origin of "half-order" peaks.

Matrix Formalism

The Matrix Formalism

In the present section the reflectivity of a layered sequence with N repeats is calculated following *Born & Wulf* [17]. The reflectivity is convoluted with the resolution function described in Chapter 3.

The matrix formulation provides a simple way of calculating the reflectivity from many bilayers. A characteristic matrix is written for each layer i in the repeated unit,

Characteristic Matrix

$$\mathbf{M_i} = \begin{pmatrix} \cos\beta_i & -\frac{\mathrm{i}}{p}\sin\beta_i \\ -\mathrm{i}p\sin\beta_i & \cos\beta_i \end{pmatrix}, \; i = 1, 2, \ldots N_{\text{layer}} \tag{107}$$

where $\beta_i = 2\pi n_i h_i \sin\theta_i/\lambda$, $p_i = n_i \sin\theta_i$, and i is the imaginary unit. Here, n_i is the refractive index of layer i with thickness h_i, θ_i is angle of incidence, and N_{layer} the number of layers . The matrices for the layers in a single unit are multiplied and the result can on account of the periodicity be expressed as

$$(\mathbf{M^{tot}})_\mathbf{N} = \begin{pmatrix} M^{\text{tot}}_{1,1}U_{N-1}(a) - U_{N-2} & M^{\text{tot}}_{1,2}U_{N-1}(a) \\ M^{\text{tot}}_{2,1}U_{N-1}(a) & M^{\text{tot}}_{2,2}U_{N-1}(a) - U_{N-2} \end{pmatrix}, \tag{108}$$

where $U_N(x) = \sin((N+1)\arccos(x))/\sqrt{1-x^2}$ are Chebyshev Polynomials of the second kind, N the number of the repeats of layer sequence, $a = 1/2(M^{\text{tot}}_{1,1} + M^{\text{tot}}_{2,2})$, and $M^{\text{tot}}_{i,j}$ matrix element (i,j) of $\mathbf{M^{tot}} = \prod_{i=1}^{N_{\text{layer}}} \mathbf{M_i}$. The reflectivity R is finally obtained from the reflection coefficient

Reflectivity

$$r = \frac{[(M^{\text{tot}}_{1,2})_N + (M^{\text{tot}}_{1,2})_N p_{N+1}]p_0 - [(M^{\text{tot}}_{1,2})_N + (M^{\text{tot}}_{1,2})_N p_{N+1}]}{[(M^{\text{tot}}_{1,2})_N + (M^{\text{tot}}_{1,2})_N p_{N+1}]p_0 + [(M^{\text{tot}}_{1,2})_N + (M^{\text{tot}}_{1,2})_N p_{N+1}]} \tag{109}$$

as $R = |r|^2$.

Roughness in the system has been incorporated in a crude way by multiplying the reflectivity R with a Debye-Waller-like factor:

Roughness

$$R_f(Q) = R(Q)\exp(-Q^2\sigma_r^2), \tag{110}$$

where σ_r is the root-mean-square roughness and $R_f(Q)$ is the final reflectivity. The factor is a good approximation for small critical scattering vectors Q_c of the original factor developed by *Nevot and Croce* [99] for the reduction of the intensity scattered from a surface.

Results of the Repeated Bilayer Approach. Firstly, the fundamental peaks were fitted with the repeated bilayer. The layer thicknesses of the bilayer are denoted d_1 and d_2 and the corresponding scattering length densities as ρ_1 and ρ_2, respectively. Together with these parameters, the total thickness of the bilayer, $d_{\text{total}} = d_1 + d_2$, and the scattering length density difference, $\Delta\rho = |\rho_2 - \rho_1|$ are given in Table 14. The scattering length density profiles of the bilayer are depicted schematically in Figure 60(a) and (b) for $T = 45°C$ and $T = 75°C$, respectively.

Parameters in the Model

T (°C)	N	d_1 (Å)	d_2 (Å)	d_{total} (Å)	ρ_1 (10^{-6}Å^{-2})	ρ_2 (10^{-6}Å^{-2})	$\Delta\rho$ 10^{-6}Å^{-2}
30	200	46.4	58.1	104.5	4.62	3.94	0.68
45	200	61.5	49.2	110.7	4.19	3.74	0.45
	150	52.2	59.5	111.7	4.95	4.33	0.62
	150	53.7	57.6	111.3	4.25	3.77	0.48
	150	59.4	52.6	112.0	3.31	2.88	0.42
75	100	60.2	68.8	129.0	4.00	3.31	0.69
	100	64.5	62.7	127.1	4.28	3.62	0.67
	200	66.4	63.5	129.8	4.35	3.17	1.18
	200	61.3	68.3	129.6	3.32	2.55	0.77

Table 14. Results from fitting a repeated bilayer sequence to the reflectivity data of a 30 wt % P85 solution. For T =45 and 75°C, the first two sets of values are for the shallow cell of 5 ml, the next for the 15 ml cell, and the last set is for the scan with the solvent contrast-matched to quartz.

Factors Determining the Model Parameters

Several factors come into play in the determination of the model parameters.

The relative values of thicknesses and scattering length densities in the bilayer are dependent on the intensity difference between the two fundamental peaks. Since the roughness reduces the intensity and enhances the difference between the main order peaks in the calculation, it will influence how the total thickness of the bilayer is divided between each of the two layers and likewise the scattering length density difference between the two layers. A large difference in the intensities will make the layer thicknesses almost equal. As the thicknesses, the scattering length densities, and the roughness are correlated, a single value of the roughness $\sigma_r = 7$ Å was chosen for the fits. Larger values of the roughness makes it impossible to attain the intensity of the higher order peaks occurring at large scattering vectors.

Roughness

A related problem in determination of the parameters is the estimation of the background. It has the same influence on the thicknesses and scattering length densities of the bilayer as the roughness. As can be seen from Figure 57 the Lorentzian, taken as the bulk contribution to the total scattering, has to be subtracted from the measured intensity to arrive at the specularly reflected neutrons. However, the Q dependence of the Lorentzian is time consuming to measure at each point with a single detector. Therefore, off-specular scans were performed at several Q values. The background was found to be highly structured. Between the peaks the specular intensity is almost indistinguishable from the background which further complicate matters. The background was higher for both the 15 ml enclosure and for the contrast matched quartz solvent than for the 5 ml enclosure. The background level is different for the two cells due to the difference in volume of the bulk solution. The second occurring low intense peak was not seen in case of the 15 ml cell and the solvent containing H_2O because of the higher background. The estimation of the background is a key factor in the the differences in the values obtained for the same temperature.

Background

The total bilayer thickness, d_{total}, in Table 14 is found to be in agreement with the values found in Table 13.

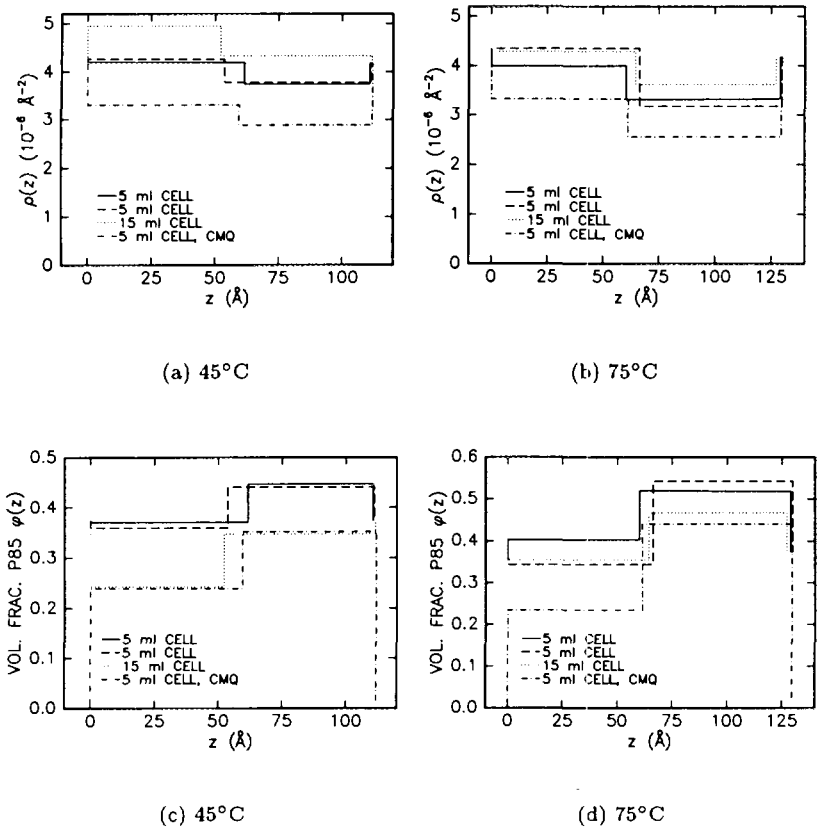

(a) 45°C (b) 75°C

(c) 45°C (d) 75°C

Figure 60. A schematic view of the scattering length density and the volume fraction of P85 of a single bilayer. The bilayer is depicted without roughness at the interfaces. The discrepancy is mainly due to the estimation of the background for the different enclosures and mixtures of solvents (see text).

Volume Fraction of P85 in the Bilayer

From the scattering length densities of the bilayer the volume fraction ϕ of P85 can be determined from $\rho = \phi\rho_{\text{P85}} + (1-\phi)\rho_{\text{solv}}$, where ρ_{solv} is the scattering length density of the solvent. Figure 60(c) and (d) show the volume fraction profile of a bilayer for a temperature of 45 and 75°C. Both the solvent contrasts show the same type of structure despite the lack of close agreement of the volume fractions of P85. In general, the bilayer appears to have a large degree of solvent penetration. This is in clear contrast to the bulk lamellar structure [93], which is suggested to consist of a *pure* PO and a more swollen EO layer. The bilayer structure can as mentioned be interpreted as planes in a cubic structure. The middle of the layer with high volume fraction of P85 is then the position of the (almost) close-packed planes which is then separated by more water dense regions. Cubic structures do allow solvent in between the aggregates. Furthermore, from the "small" contrast $\Delta\rho$ between the layers it appears as a likely possibility.

"Half-Order Peaks"

Still, the "half-order" peaks in the reflectivity profiles need to be explained. Their appearance mid between the main order peaks indicate a periodic perturbation of the structure giving rise to double the period arising from the main order peaks. The large polydispersity of aggregates can not explain the occurrence of the "half-order" peaks due to the fact, that it is a random component. In magnetism, low intense reflections of the double period occur when the magnetic moments are ferro-magnetically ordered along the c-axis with a small component in the basal plane, which is anti-ferromagnetically ordered. In analogy, a repeated stack of four (ABA'B) layers gives the double period needed to obtain the low intensity peaks.

The repeated unit (ABA'B) consists of two bilayers, AB and A'B, with obtained values from the main peak analysis but only allowing the scattering length density of the first layer of the second bilayer (A') to change. This approach was able to reproduce the "half-order" peaks with only approximately 2% difference in the scattering length density between layer A and A'.

Differing Bulk and Surface Structure

Another approach is to assume a different surface structure than the one occurring in the bulk. If both the surface and bulk are ordered, the distinction is problematic as it is impossible to determine exactly where the structure becomes bulk ordered. The regular periodicity of all the peaks makes it unlikely that the "half-order" peaks should arise from a structure with almost exactly twice the period. As mentioned in the introductory remarks, bulk measurements [93] have suggested the existence of lamellar phase with a period in the close proximity of 230 Å in P85 melts and in solutions with 0-20 wt % water content. The repeat distance is close to the value we observe for the periodicity of the "half-order" peaks. Both to quantify the "half-order" peaks and to follow the twin structure approach the following approach was attempted:

Two Structure Model

A model consisting of N_{surf} layers with the double period of the subsequent N_{bulk} bilayers was fitted to the reflectivity curves. The former modeling lamellar ordering at the solid-liquid interface and the latter the bulk crystalline phase. The characteristic matrix for the whole system is

$$\mathbf{M}^{\text{res}} = \mathbf{M}^{N_{\text{surf}}}\mathbf{M}^{N_{\text{bulk}}}. \tag{111}$$

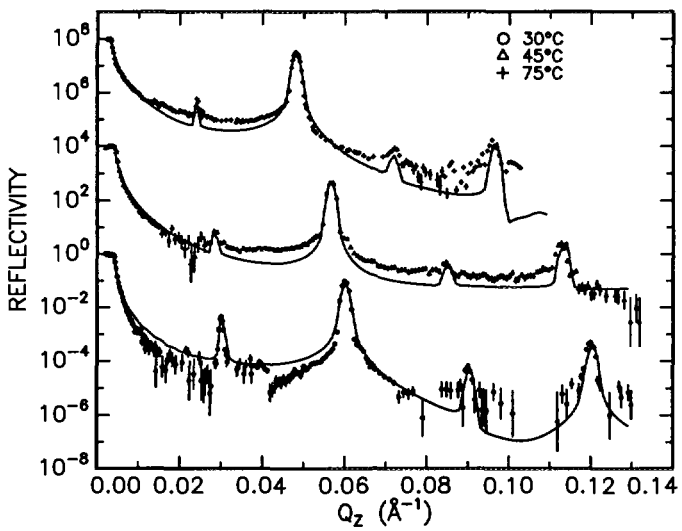

Figure 61. The comparison between the reflectivity curves at 30, 45, and 75°C at 30 wt % and the "two-phase" model. The latter consists of N_{surf} layers with the double period of the subsequent N_{bulk} bilayers.

This approach gives a good representation of the data (see Figure 61). The peaks at 30°C appears to be more narrow in comparison to the peaks at higher temperatures. The values are summarized in Table 15 below. We see, that the thickness of the bulk bilayers are only slightly less than half the value for the corresponding surface structure value for all temperatures. However, the difference is not profound and is probably due to the poor statistics of the "half-order" peaks. Consequently, all the peaks are related to a single structure and not separate structures at the surface and in the bulk. The origin of the "half-order" peaks can suggestively be due to anisotropic micelles distorting the lattice periodically to give the double period. A possibility is a herringbone structure of slightly anisotropic micelles (the particles "zig-zag" along the surface normal). A slight periodic change

in the angle between the director of these micelles and the surface normal might create the double period.

T (°C)	N_{surf}	$d_{surf,1}$ (Å)	$d_{surf,2}$ (Å)	d^{tot}_{surf} (Å)	$\rho_{surf,1}$ (10^{-6}Å^{-2})	$\rho_{surf,2}$ (10^{-6}Å^{-2})
30	100	160	48	209	4.31	4.22
45	50	205	20	224	4.03	3.93
75	100	211	52	264	3.65	3.58
T (°C)	N_{bulk}	$d_{bulk,1}$ (Å)	$d_{bulk,2}$ (Å)	d^{tot}_{surf} (Å)	$\rho_{bulk,1}$ (10^{-6}Å^{-2})	$\rho_{bulk,2}$ (10^{-6}Å^{-2})
30	100	46	58	104	4.72	3.84
45	150	62	50	111	4.80	4.29
75	200	66	64	130	4.37	3.16

Table 15. Representative values for the different temperatures obtained from fitting to the "two-phase" model.

6.4 Discussion

The main result of this chapter is the strong surface induced ordering of the triblock copolymer in solution in a well-order layering parallel to the quartz surface. The correlation length obtained from the Bragg peaks exceeds 7000 Å and the periodicity perpendicular to the surface was for 30, 45 and 75°C found to be 104 ± 1 Å, 111 ± 1 Å, and 130 ± 1 Å, respectively. The structure of the triblock copolymer is ambiguous and cannot be determined solely from reflectometry. However, the layering is seen to vanish at about 23°C and the periodicity obtained from the strongest reflection does show a discontinuity close to 58°C when the sample is heated and at 55°C as the sample is cooled. This is a strong indication of a *bulk* related behaviour which has been seen in SANS measurements. In the bulk, the first appearance of ordering is due to the formation of BCC micellar crystals, which transform into hexagonally ordered rods around 60°C after an intermediate liquid phase of disordered rods. It is not possible with specular reflectivity to distinguish between BCC(110), FCC(111), or HCP(002) ordered layers parallel to the surface. However, it is unlikely that the micelles order in the most densely packed HCP structure due to the soft interaction potential of the micelles and the considerable polydispersity.

Another problem encountered is the separation of the bulk from surface related ordering. Since both the surface and the bulk aggregation appear to have long-range order, no clear distinction between the surface and the bulk related ordering can be made.

From the reflectivity measurements low intensity temperature dependent "half-order" peaks appear giving an indication of an additional component to the ordering of the aggregates. Suggestively, a lamellar surface ordering, seen in the pristine material and solutions containing less than 20 wt % water, can explain this ordering. However, this type of ordering is not likely since the period of the tentative lamellar ordering is almost exactly twice the period of the bulk layering. The likely physical explanation for this ordering is a dehydration of the triblock copolymer at the surface due to the binding of the water in the micellar crystal.

One should, however, bear in mind that the incoming neutrons do contain neutrons with half the desired wavelength. Since this intensity is not temperature dependent it justifies the additional temperature dependent surface component in the structure.

The response by the triblock copolymer to the presence of a surface is similar to shear orienting the sample. Tentatively, the application of shear in bulk samples effectively extends the already surface ordered crystals.

To remove the ambiguity of the interpretation of the ordering additional measurements has to be performed, e.g. "near-horizon" SANS [47]. Here, the neutrons has an angle of incidence just above the critical edge and will consequently only probe the near-surface region. All the neutrons scattered back from the solution in addition to the specularly reflected neutrons are detected. This technique has been successful in the determination of the shear induced hexagonal surface ordering of charged thread-like micelles of the cationic surfactant cetyltrimethylammonium 3,5 -dicholorobenzoate (see *Hamilton et al.* [47, 48]). Another technique that might be able to resolve the ambiguity of the structure is X-ray grazing-incidence-diffraction, where the in-plane ordering can be probed.

7 Conclusion and Outlook

In the present thesis the main emphasis has been paid to the ordering of the micellar liquid phase of the triblock copolymer P85 in aqueous solution. Ordering both in the bulk and at the hydrophilic surface of quartz has been investigated.

The traditional model of the micelle as solid spheres has been extended by treating the corona of the micelle as tethered Gaussian chains. For this particular case it is possible to calculate an analytical expression for the form factor (Chapter 2). This form factor was tested against Monte Carlo (MC) simulations of chains generated as three dimensional random walks attached to a spherical core. Good agreement was found in the range from small to large radius-to-chain length ratios. Initially, no excluded volume interactions were taken into consideration. To avoid the unphysical penetration of the tethered chains into the core, the volume of the core was excluded from the tethered chains. The effect could be mimicked by a translation of the attachment of the tethered chains in the model from R to approximately $R + R_g$. The corresponding form factor fitted the scattering curves obtained from SANS measurements of P85 in low concentration aqueous solution ($c < 0.5$ wt %). At higher concentrations, where the inter micellar interaction comes into play, the model showed slight deviations from the data. This might be caused by the assumption of hard-sphere interaction between micelles which was chosen because of the analytic structure factor in the *Percus-Yevick* approximation. Consequently, an improvement would be to use a more suitable potential. However, it would introduce additional parameters to an already many parameter model. Deviations from the model were observed in the high temperature region of the micellar liquid phase. The discrepancy is probably caused by an elongation of the micelles starting close to the transition into rod-like micelles.

The main limitation of the model is the neglect of excluded volume interactions between the chains and inside the chain itself. Therefore, the conformation of the chains in the model corresponds to the mushroom regime of non-interacting polymers grafted at a flat surface. The next step would be to perform MC simulations with excluded volume interactions in full and investigate whether the analytical form factor maintain its validity.

After establishing a suitable model for the structure of the micelle, the micellar ordering at the solid-liquid interface was investigated. Free-form analysis of the neutron reflectivity measured at the interface between an aqueous solution of P85 and a quartz single crystal revealed decaying oscillations of the scattering length density away from the surface. The profiles hinted toward a micellar layering at the surface with a decreasing order away from the solid-liquid interface. Attempts to parameterize the scattering length density profile with a single periodic decaying function failed to reproduce the reflectivity curves. Therefore, a scheme was set up incorporating the micellar model and the distribution of hard spheres at a hard wall. The latter was obtained from MC simulations of hard spheres at hard wall performed for a range of volume fractions, η, below the freezing transition at $\eta = 0.49$. The density of hard spheres was taken as representative of the center distribution of the micelles. It was justified since the hard-sphere interaction is valid for the micelles in the bulk. As specular reflectivity measurements only reflect the averaged scattering length density profile along the normal to the surface it was necessary to project the scattering length density of the micelle taken as either a solid sphere or a solid sphere with tethered chains following Gaussian statistics. The final numerical expression, which can be fitted directly to the reflectivity data, results from a convolution of the projected profile of a micelle and the center distribution of the micelles. The model parameters were the hard-sphere volume fraction, the radius of the core, the hard-sphere interaction radius, the scattering

length density of the inner most fluid layer, and the roughness at the solid-liquid interface.

Experimentally, the neutron reflectivity curves were measured at three concentrations, 15, 20, and 25 wt %, in the temperature region between 30°C and 60°C. Both the solid sphere model with and without tethered chains showed excellent agreement for the 15 and 20 wt % solutions, whereas the model showed an increasing discrepancy with the 25 wt % data with increasing temperatures. From the free-form profiles it was evident that the discrepancy was caused by larger amplitudes in the ρ profile at large distances from the quartz surface than the model is able to reproduce. A likely explanation is a larger precrystallization than the model is able to describe in the inner micellar layers closest to the quartz surface. Another explanation could have been surface order of BCC micellar crystallites, but this possibility was ruled out by shearing the solution which should have provoked alignment of the crystallites as previously seen in SANS measuremens [92].

The volume fraction and hard-sphere interaction radius showed a systematic variation with concentration and temperature, whereas for the radius of the core no clear trend could be identified. This is due to the only slight influence of the radius of the core on the shape of the scattering length density profile because of the convolution between the projected density of the micelle and the center distribution. The volume fraction was found to increase with concentration. The hard-sphere interaction radius was found to decrease with concentration and increase with temperature. These findings are in good correspondence with the bulk behaviour [94].

The scattering length density profiles showed a depletion zone on the quartz surface with a polymer concentration approximately one third of the expected bulk value. A surprising result, since EO adsorbs to SiOH groups of hydrophilic quartz in aqueous solution. However, with the limited resolution of the reflectivity experiment (20-25 Å) an adsorbed layer on the surface layer with a subsequent pure solvent layer would give the same average density. Simulations of surfactants at the oil-water interface have shown that the presence of a monolayer at the oil-water interface gives rise to repulsion between the monolayer and the bulk micelles resulting in a depletion zone [126]. The concentration of P85 at the surface showed no systematic variation with temperature.

For temperatures close to 70°C anisotropic aggregates appear as the spherical micelles elongate into a rod-like shape. *Mortensen & Pedersen* have suggested that the spherical shape initially transforms into prolate ellipsoids. Reflectivity measurements of a 5 wt % solution surprisingly showed a comparatively narrow peak and thus implied a strong surface association already at 60°C. However, for concentrations $c > 15$ wt % no departure from the broad peak were seen at 60°C. The reflectivity of the 5 wt % could not be fitted by the micellar model, but the fitting did indicate a larger volume fraction ($\eta = 0.38$) of the micelles than expected ($\eta \approx 0.10$ from the bulk solution). As the temperature was increased, the peak narrowed, and the reflectivity show both first and second order peaks at 72°C with a periodicity of 111 ± 1 Å perpendicular to the surface. The reflectivity could be fitted by an ordering with a dense polymer layer closest to the surface instead of a water rich layer. This type of ordering is physically plausible because the increasing hydrophobicity of ethylene oxide with temperature makes it favourable for the polymer to surface associate more strongly than seen in the liquid micellar phase.

The analysis of the reflectivity data can not distinguish between aggregates or lamellar ordering at the surface. The temperature dependency strongly suggests a transformation from isotropic over anisotropic aggregates to a lamellar phase. When the solution was sheared at 72°C, the peaks disappeared. An indication that one does not have rod-like objects as these have been observed to order with

applied shear in the bulk solution [89]. The ambiguity can possibly be resolved by performing experiments with different contrast between the P85 and the solvent (by using e.g. H_2O, contrast matched quartz, and D_2O).

Finally, the surface induced ordering of the cubic micellar and hexagonal ordered rod phase was investigated by looking at the temperature dependence at a single concentration (c = 30 wt %). As the BCC ordering temperature was surpassed almost resolution limited peaks appeared. The temperature dependence of the most intense peak closely followed the expected bulk behaviour and the transition from cubic to hexagonal ordering was clearly observed in the amplitude and period of the peak. However, since it is not possible to measure the in-plane ordering with specular reflectivity, no distinctions can be made between body-centered cubic, face-centered cubic, or hexagonal ordered micelles. A set of faint "half-order" peaks appeared in the profile indicating a structural component with twice the period. No definite conclusions can be made from this observation however.

The work of this thesis has almost exclusively used neutron scattering techniques. For this study of the solid-liquid interface it has been shown with clarity that in order to unambiguously determine the surface ordering it is necessary to perform detailed modeling or include knowledge from other complementary techniques. Specular reflectivity often gives ambiguous possibilities for surface structures since it only probes the scattering length density along the surface normal. It would in many cases benefit from knowledge of the in-plane ordering by e.g. performing grazing-incidence-diffraction.

A Reflectivity Measurements: Resolution and Uniqueness

Different issues can be raised in connection with the modeling of surface ordering of micelles based on neutron reflectivity measurements. Key problems related to the neutron reflectivity measurements in this thesis are that the experimental data covers "only" four-five orders of magnitude and a limited Q-range, which can lead to an ambiguous scattering length density profile. Furthermore, in view of the resolution of the experiment it is important to determine whether too detailed information is extracted from the present data. Specifically, the method of analysis gives rise to the following questions:

(I) Throughout the thesis the free-form method have mainly been used to obtain ideas on which explicit modeling can be based. The free-form method uses expansions of the scattering length density with either cubic b splines or sines/cosines as basis functions. Is the large number of free parameters in the free-form method too large to give meaningful scattering length density profiles?

(II) Is the five parameters of the micellar model, which is extracted from the reflectivity data, too many?

(III) What is the "real space resolution" of the experiment?

(IV) Are the profiles obtained from the free-form method and the modeling unique and do they lead to a unique interpretation of the data?

In the next sections these points will be investigated thoroughly to provide support for the interpretation of the reflectivity data.

Number of Parameters

ad (I): The number of parameters, which is the same as the number of cubic b splines, in the free-form determination of the scattering length density profile has a lower but no upper limit. The lower limit is crucial, since the number of functions has to be large enough to allow sharp features in the profile to be described. The maximum number of parameters N for the cubic b-splines can be estimated from the **Sampling Theorem for Fourier transforms**. Following *Pedersen & Hamley* [49] $N = z_{\max} Q_{\max}/\pi - 2$, where the scattering length density profile is defined in the region $[0, z_{\max}]$ and the scattering vectors in $[0, Q_{\max}]$. However, sharp features in the real density profile gives rise to ringing, i.e. fast oscillations in the free-form profile, which can be overcome by an increasing number of splines. To avoid unphysical fast oscillations in the reflectivity profile arising from the numerical instability, a smoothness constraint on the amplitude of the splines then has to be applied as described by *Pedersen & Hamley*. Hence, the number of splines was increased until no difference in the density profile was seen. In practice, this means that above 80 splines are used, however, the effective number of free parameters are significantly lower due to the application of the smoothness constraint.

ad (II): According to the above mentioned sampling theorem the number of model parameters, which can be drawn from the reflectivity data, is $N = 500$ Å 0.06 Å^{-1} $/\pi - 2 \approx 7$. Furthermore, for a single peak on a sloping background three (symmetric peak) to four (asymmetric peak) parameters are needed to describe the form and at least two to three parameters to describe a linear or parabolic background, respectively. A total of five to seven parameters. Since five parameters of the model of the surface ordering of micelle are the same or less than a primitive estimation of a peak and are within the limit of the sampling theorem, they are fully justified.

ad (III): A detailed analysis have performed of the "real-space resolution" which can be obtained from a reflectivity experiment. The following examples support a better resolution than the commonly used $2\pi/Q_{max}$, and thus sensitivity to the detailed model:

"Real Space Resolution"

(a) Free-form determination of the multilayer profiles as a function of the reflectivity truncation.

(b) Recovering the profile with free-form method after various degrees of truncation of the reflectivity profile.

(c) Recovering the parameters of the model after truncation at 0.065 $Å^{-1}$ of the reflectivity profile.

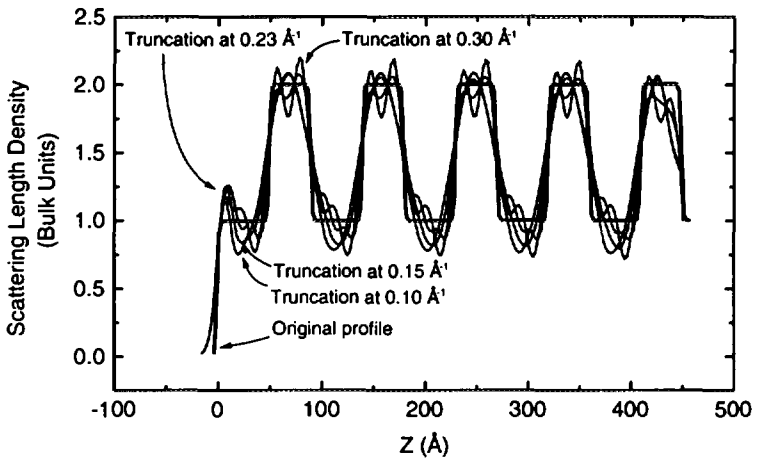

Figure 62. Comparison between the scattering length density profiles obtained from the Fourier-Synthesis Method for various truncation and the original profile.

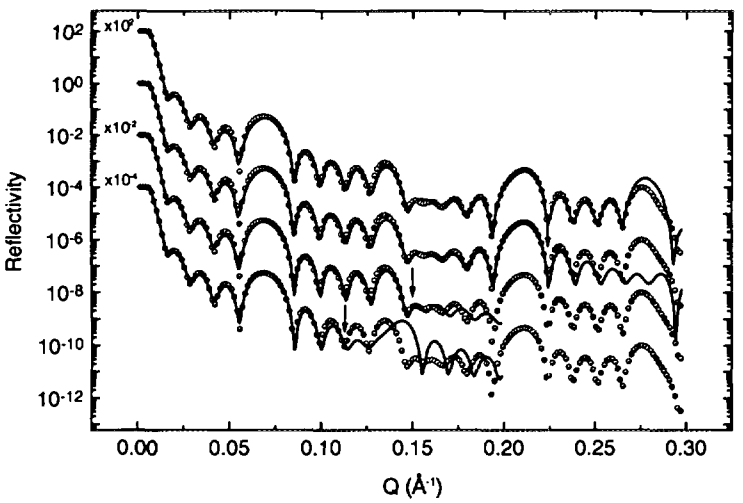

Figure 63. The reflectivity from the multilayer profile and the fits at various truncations indicated by the arrows.

ad (a): The reflectivity have been calculated dynamically from 5 repeats of a bilayer consisting of a 40 Å and a 50 Å thick layer with a scattering length density of 1 and 2 bulk units, respectively. The standard deviation on each point of the reflectivity curve was taken to be 1 %. The dimensions of the bilayer are comparable to the dimensions of the P85 micelle. Figure 62 shows the original scattering length density profile and four examples of the obtained profiles obtained with the Fourier-Synthesis Method (*Singh et al.* [124] and *Pedersen and Hamley* [106]) for various

Interfacial Width as a Function of Truncation

truncations. The reflectivity data and the fits are shown in Figure 63. The truncations, 0.1, 0.15, 0.23, and 0.3 $Å^{-1}$ indicated by the arrows in Figure 63, correspond to accepting data below the 1st, 2nd, 3rd, and 4th order Bragg reflections.

The width of the interface of the found profile is determined by fitting a Gaussian with standard deviation σ to the differentiated profile close to each interface. The standard deviation σ will be comparable to the standard deviation of an error function representing the interface and is thus a measure of the resolution of the experiment.

It was found that the standard deviation $\sigma \approx 1.5/Q_{max}$, where Q_{max} is the truncation scattering vector.

If $Q_{max} = 0.06$ $Å^{-1}$, we will thus obtain a resolution of 25 Å, which is 4 times better than the $2\pi/Q_{max}$ estimate. However, it does imply that the roughness of 5 Å of the solid-liquid is too small to be well-determined from the Q_{max} of the reflectivity experiments and consequently has to be related more to the actual shape of the profile than as a true value of the roughness.

ad (b): *Zhou et al.* [141] have investigated specular neutron reflectivity data from surface-induced layering in bicontinuous microemulsions which display the same broad peak as our micellar ordering. The authors found that truncation gives rise to a lowering of the initial peak in the scattering length density profile. Only when the truncation is below the broad peak the periodicity of the profile is affected.

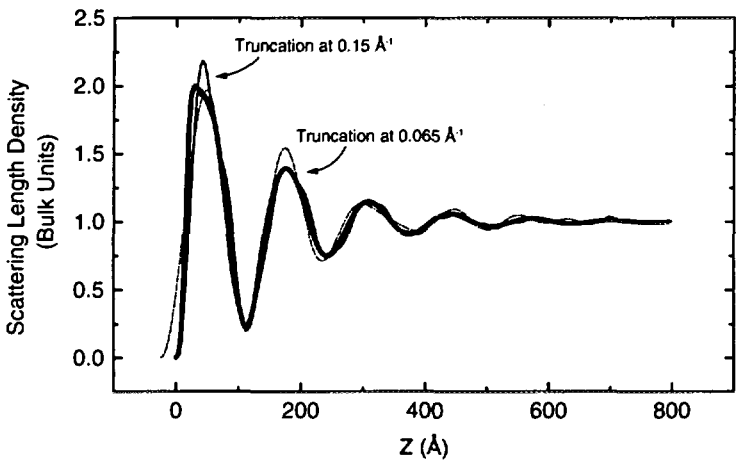

Figure 64. Free-Form profiles obtained for three truncations. The truncation at 0.30 $Å^{-1}$ cannot be distinguished from the original full-drawn profile.

Effect of Truncation on the Free-form Profile

In line with these investigations a series of free-form profiles (71 cubic b splines over a total of 700 Å) was obtained from a simulated reflectivity curve (see parameters below) at various truncations. In Figure 64 the scattering length density profiles are shown for various truncations. The original profile is plotted as the full-drawn line. The corresponding reflectivity profiles are not shown due to the fact that they do not differ from the original curve (they are all similar to the simulated profile of Figure 65).

The *unbiased* free-form method produces the same type of profile as the original profile. Even at the lowest Q_{max} no evidence was found for other profiles that would fit the reflectivity data equally well. In accordance with *Zhou et al.*, even for the lowest Q_{max} the period is in

acceptable correspondence with the original profile. The amplitude of the oscillations are exaggerated for larger truncations.

Model Fit to the Free-form Profiles

The micellar model was thereafter fitted to the free-form profiles. Below are the parameters obtained from the micellar model fits to the free-form profiles. Here, R_{HS} is the hard-sphere interaction radius, η the volume fraction, ρ_{fluid} the scattering length density of the innermost layer, σ_{erf}, the standard deviation of the error function used for the solid-liquid interface, and R is the core radius in the micellar model.

Parameter	Initial value	Truncation Q_{max}	
		0.065Å^{-1}	0.15Å^{-1}
R_{HS}/Å	68	69	66
η	0.39	0.42	0.43
ρ_{fluid}/Å^{-2}	2x10^{-6}	2x10^{-6}	1.8x10^{-6}
σ_{erf}/Å	5	9.6	7.3
R/Å	36	36	28

Evident from the above table is the good agreement and sensitivity to the parameters for both examples. It is natural for the micellar core radius R to show the largest variation, since it enters the model via a convolution. The value for the roughness is too high, but is related to the truncation and thus the "real space resolution" of the experiments.

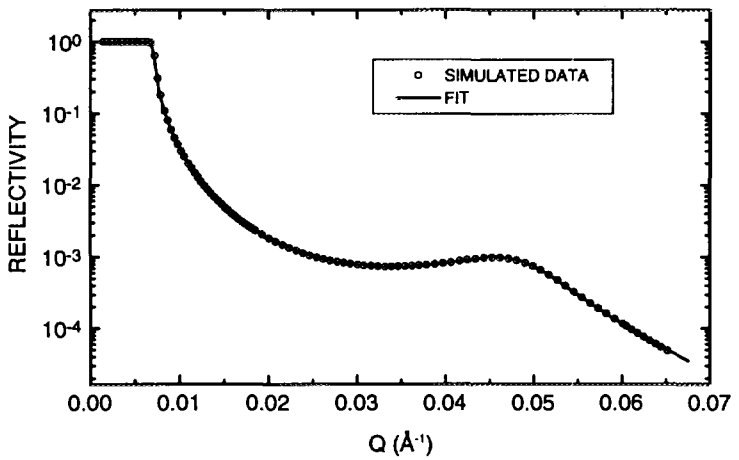

Figure 65. Simulated and model fit to the reflectivity curve

Recovery of the Model Parameters after Truncation

ad (c): A reflectivity curve was simulated with the same initial parameters as in (IIIb) and truncated at 0.065 Å^{-1}. The model fit to the reflectivity data gave the values R_{HS}= 68 Å, η= 0.39, ρ_{fluid} = 2.05 × 10^{-6}Å^{-2}, σ_{erf}=4.9 Å, R= 38 Å, which are close to the initial parameters. The reflectivity data and the corresponding density profiles are shown in Figures 65 and 66. The original parameters can thus be retrieved from the truncated reflectivity curve.

ad (IV): The problem of uniqueness of the solutions determined by model-independent methods is a central problem in the analysis of reflectivity data. For the profiles of micelles at the surface of quartz the main jump in the density profile concerning both sharpness and height is at the quartz-liquid interface. The model-independent method is the *phasing* of the rest of the profile with

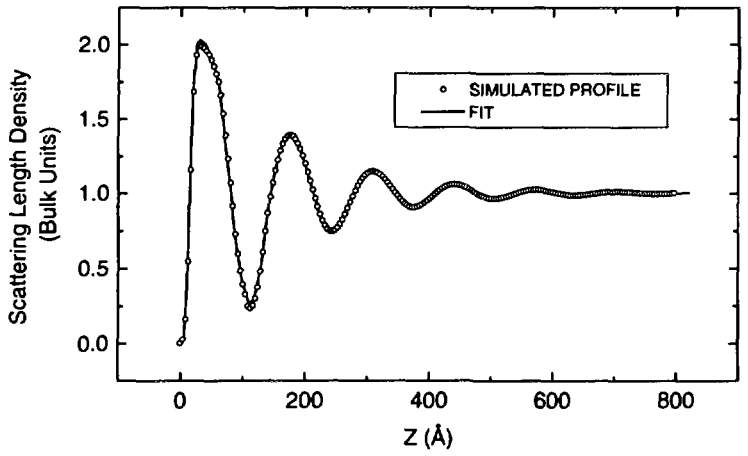

Figure 66. The found scattering length density profile from model fit to the simulated reflectivity curve.

respect to this interface. The situation has some analogy to the *heavy-atom* method in crystallography. As it is known that the main interface (the heavy atom) is the quartz-liquid interface, it is believed that we can consider the profiles to be unique for this system. In addition it has been found that the profiles, which are determined are very stable to the noise in the experimental data. The method never finds a false minima. As an example, the 20 wt % P85 data at 40 °C was analyzed according to the procedure outlined by *Svergun & Pedersen* [130]: Several data sets were generated from the original profile by randomly choosing each point in the new profile from a Gaussian distribution centered at and with the standard deviation of the original point. The generated scattering length density profiles are shown in Figure 67. One sees, that the large oscillations are nicely reproduced in all profiles whereas the oscillations at high z-values are smeared out.

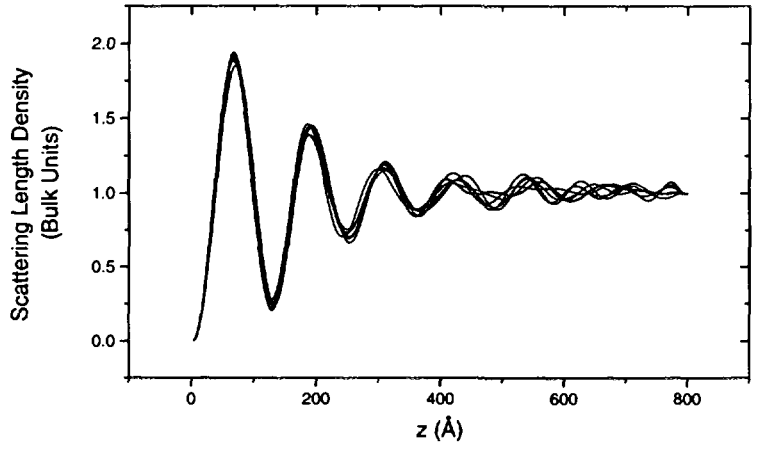

Figure 67. The scattering length density profiles generated from reflectivity data of 20 wt % P85 solution.

The above outlined approach is the one used for obtaining the results in the paper. In conclusion, these examples show that the resolution is approximately $1.5/Q_{\max}$, which is smaller than the commonly used $2\pi/Q_{\max}$. It is our firm belief that the 5 parameter model is fully justified with the reflectivity measurements at hand.

It is perhaps in place to mention additionally that it is experimentally almost impossible to obtain better data than those we present in our paper for systems

with both surface and bulk order. The bulk scattering form the micelles gives rise to a very broad peak and the surface signal, a sharp specular reflectivity peak, is superimposed on this signal. It is therefore extremely difficult to separate these two signals when the surface signal is reduced by four orders of magnitude at high Q.

Acknowledgments

It would have been an impossible task to have finished this thesis without the support I have received the past three and a half years.

First of all, I want to thank my beloved Benedikte Rindom, who has stood by me through it all and who has accepted that the reactor is running, even in the week-ends. I will always be indebted to the special and tender care I have been given not the least in the final stages of the writing up.

I want to express my utmost gratitude for all who has opened their homes to me, letting me feel at home in a stressed period of time: Iben and Bent Rindom, my sister Christina, Max, Tobias, and Mads Jacobsen and Esben Henrichsen.

My warm thanks to the life long support I have gotten from my parents, Bente and Thomas, and not the least my grandmother Else Gerstenberg. I also greatly appreciate the help of Benedikte's family.

My supervisor Jan Skov Pedersen has given me a whole new perspective on physics with his insight in data analysis and simulations. I have greatly benefited from the ideas and inspiration risen from our discussions. I thank Jan for his patience, support, and supervision during the past three years. I also thank my supervisor Stig Steenstrup for his continuous support and encouragement during this work.

Steen Aagaard Sørensen, Morten Jagd Christensen, my office mates, are acknowledged for their pleasant company and always helpful attitude. I'm especially grateful for their help with computational matters.

In particular, I want to thank the Post. Doc.'s Niels B. Larsen and Christine Papadakis for the careful and thorough review of most of this work and the many suggestions for improvements in the manuscript and Esben Henrichsen for the English corrections. Prof. Jens Als-Nielsen is acknowlegded for useful suggestions and corrections to the manuscript before the thesis was finally printed.

I have greatly benefited from the support of the skilled staff at Risø. I especially want to thank Steen Nielsen, Keld Theodor, Finn Saxild, Bjarne Breiting, and Morits Lund for their readiness to help especially with the last minute adjustments. Lajla Frederiksen and Ca Studinski are also acknowledged for their smooth way of handling many practical problems. Furthermore, I have highly appreciated the daily company of my fellow students, Post.Doc.'s and colleagues at the Solid State Physics Department.

During the three months I have stayed at the Los Alamos National Laboratory in New Mexico, USA, I have gained invaluable knowledge about neutron scattering of soft materials from Greg Smith and Jarek Majewski. Ross Sanchez is acknowledged for his technical assistance. I'm very thankful for the great effort they have shown in making my trip to New Mexico a success.

I'm grateful for the financial support given to me by the Department in the late stages of the study. Especially, I thank for the encouragement given to me by Kurt N. Clausen, the neutron section leader.

Finally, I want to thank all my friends for their understanding trough the duration of this work. They have many times accepted the preoccupation of mind of this "rocket" scientist.

Roskilde, July 1997

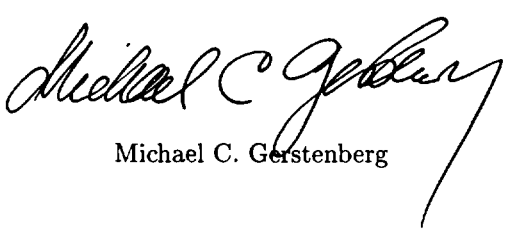

Michael C. Gerstenberg

References

[1] S.M. Aharoni. On entanglements of flexible and rodlike polymers. *Macromolecules*, 16:1722, 1983.

[2] B. Alder, W. Hoover, and D. Young. Studies in molecular dynamics. v. high-density equation of state and entropy for hard disks and spheres. *J. Chem. Phys.*, 49:3688, 1968.

[3] S. Alexander. Adsorption of chain molecules with a polar head. A scaling description. *J. Phys. (Paris)*, 38:983–987, 1977.

[4] P. Alexandridis and T.A. Hatton. Poly(ethylene oxide)-poly(propylene oxide)-poly(ethylene oxide) block copolymer surfactants in aqueous solutions and at interfaces: Thermodynamics, structure, dynamics, and modeling. *Colloids Surf. A*, 96:1–46, 1995.

[5] P. Alexandridis, J.F. Holzwarth, and T.A. Hatton. Micellization of poly(ethylene oxide)-poly(propylene oxide) triblock copolymers in aqueous solutions: Thermodynamics of copolymer association. *Macromolecules*, 27:2414–2425, 1994.

[6] M. Almgren, W. Brown, and S. Hvidt. Self-aggregation and phase behaviour of poly(ethylene oxide)-poly(propylene oxide)-poly(ethylene oxide) block copolymers in aqueous solution. *Colloid Polym. Sci.*, 273:2–15, 1995.

[7] J. Als-Nielsen. X-ray reflectivity studies of liquid surfaces. In G. Brown and D.E. Moncton, editors, *Handbook on Synchrotron Radiation*, volume 3, pages 471–503. Elsevier Science Publishers, 1991.

[8] J. Als-Nielsen. Diffraction, refraction and absorption of x-rays and neutrons: A comparative exposition. In J. Baruchel, J.L. Hodeau, M.S. Lehmann, J.R. Regnard, and C. Schlenker, editors, *Neutron and synchrotron radiation for condensed matter studies.* Springer-Verlag, 1993.

[9] J. Als-Nielsen, F. Christensen, and P.S. Pershan. Smectic-A order at the surface of a nematic liquid crystal: Synchrotron x-ray diffraction. *Phys. Rev. Lett.*, 48(16):1107–1110, 1982.

[10] J. Als-Nielsen, D. Jacquemain, K. Kjær, F. Leveiller, M. Lahav, and L. Leiserowitz. Principles and applications of grazing incidence x-ray and neutron scattering from ordered molecular monolayers at the air-water interface. *Phys. Rep.*, 246:251–313, 1994.

[11] J. Als-Nielsen and K. Kjær. X-ray reflectivity and diffraction studies of liquid surfaces and surfactant monolayers. In T. Riste and D. Sherrington, editors, *Phase Transitions in Soft Condensed Matter*, pages 113–138, New York, 1989. Plenum Press.

[12] J.K Armstrong, J. Parsonage, B. Chowdhry, S. Leharne, K. Löhner, and P. Laggner. Scanning densitometric and calorimetric studies of poly(ethylene oxide)/poly(propylene oxide)/poly(ethylene oxide) triblock copolymers (polyxamers) in dilute aqueous solution. *J. Chem. Phys.*, 97:3904, 1993.

[13] S.M. Baker, G. Smith, R. Pynn, P. Butler, J. Hayter, W. Hamilton, and L. Magid. Shear cell for the study of liquid-solid interfaces by neutron scattering. *Rev. Sci. Instrum.*, 65(2):412–416, 1994.

[14] H. Benoit. The effect of branching and polydispersity on the angular distribution of the light scattered by gaussian coils. *J. Polym. Sci.*, 11:507, 1953.

[15] J.-F. Berret, D.C. Roux, G. Porte, and P. Lindner. Tumbling behaviour of nematic worm-like micelles under shear flow. *Europhys. Lett.*, 32(2):137–142, 1995.

[16] P.R. Bevington and D.K. Robinson. *Data reduction and error analysis for the physical sciences.* McGraw-Hill, Inc., 2nd edition, 1992.

[17] M. Born and E. Wolf. *Principles of optics. Electromagnetic theory of propagation interference and diffraction of light.* Pergamon Press, 6th edition, 1980.

[18] W.G. Bouwman and J.S. Pedersen. Resolution function for two-axis specular neutron reflectivity. *J. Appl. Cryst.*, 29:152–158, 1996.

[19] W.G. Bouwman, M. Vigild, E. Findeisen, K. Kjær, R. Feidenhans'l, and E.A.L. Mol. Two-axis neutron and x-ray reflectivity: How to avoid alignment pitfalls and how to correct for them. *J. Neutron Res.*, 5:133–146, 1997.

[20] J. Brandrup and E.H. Immergut. *Polymer Handbook.* Wiley-Interscience, New York, 1975.

[21] W. Brown, K. Schillén, M. Almgren, S. Hvidt, and P. Bahadur. Micelle and gel formation in a poly(ethylene oxide)/poly(propylene oxide)/poly(ethylene oxide) triblock copolymer in water solution. dynamic and static light scattering and oscillatory shear measurements. *J. Phys. Chem.*, 95:1850, 1991.

[22] W.R. Burghardt and G.G. Fuller. Role of director tumbling in the rheology of polymer liquid crystal solutions. *Macromolecules*, 24:2546–2555, 1991.

[23] B. Chu. Structure and dynamics of block copolymer colloids. *Langmuir*, 11:414–421, 1995.

[24] T. Cosgrove, J.S. Phipps, and R.M. Richardson. Neutron reflection from polymers adsorbed at the solid/liquid interface. In H. Zabel and I.K. Robinson, editors, *Surface X-ray and Neutron Scattering*, volume 61 of *Springer Proceedings in Physics.* Springer-Verlag, 1991.

[25] M. Daoud and J.P. Cotton. Star shaped polymers: A model for the conformation and its concentration dependence. *J. Phys. (Paris)*, 38:983, 1977.

[26] P.G. de Gennes. *The physics of liquid crystals.* Clarendon Press, Oxford, 1975.

[27] P.G. de Gennes. Conformations of polymers attached to an interface. *Macromolecules*, 13:1069–1075, 1980.

[28] P. Debye. Scattering of x-rays. *Ann. Phys. Leipzig*, 46:809, 1915.

[29] P. Debye. Molecular-weight determination by light scattering. *J. Phys. Colloid. Chem.*, 51:18, 1947.

[30] M. Doi and S.F. Edwards. *The theory of polymer dynamics.* Clarendon Press, Oxford, 1986.

[31] H. Dosch. *Critical phenomena at surfaces and interfaces: Evanescent x-ray and neutron scattering*, volume 126 of *Springer tracts in modern physics.* Springer-Verlag, 1992.

[32] B. Farago, M. Monkenbusch, D. Richter, J.S. Huang, L.J. Fetters, and A.P. Gast. Collective dynamics of tethered chains: Breathing modes. *Phys. Rev. Lett.*, 71:1015, 1993.

[33] J.B. Field, C. Toprakcioglu, R.C. Ball, H.B. Stanley, L. Dai, W. Barford, J. Penfold, G. Smith, and W. Hamilton. Determination of end-adsorbed polymer density profiles by neutron reflectometry. *Macromolecules*, 25:434–439, 1992.

[34] J.B. Field, C. Toprakcioglu, L. Dai, G. Hadziioannou, G. Smith, and W. Hamilton. Neutron reflectivity study of end-adsorbed diblock copolymers: Cross-over from mushrooms to brushes. *J. Phys. II (Paris)*, 2:2221–2235, 1992.

[35] G.J. Fleer, M.A. Cohen Stuart, J.M.H.M. Scheutjens, T. Cosgrove, and B. Vincent. *Polym. Int.* Chapman & Hall, London, 1993.

[36] G. Fleischer. Micellization in aqueous solution of a poly(ethylene oxide)/poly(propylene oxide) triblock copolymer investigated with pulsed field gradient nmr. *J. Phys. Chem.*, 97:517–521, 1993.

[37] P.J. Flory. *Statistical Mechanics of Chain Molecules.* John Wiley & Sons. Inc., New York, 1969.

[38] R.W. Fox and A.T. McDonald. *Introduction to Fluid Mechanics.* John Wiley & Sons, Inc, 3rd edition edition, 1985.

[39] A.P. Gast. Structure, interactions, and dynamics in tethered chain systems. *Langmuir*, 12:4060–4067, 1996.

[40] U. Genz, B. D'Aguanno, J. Mewis, and R. Klein. Structure of sterically stabilized colloids. *Langmuir*, 10:2206–2212, 1994.

[41] M.C. Gerstenberg, J.S. Pedersen, and K.N. Clausen. Neutron reflectometry from solid-solid and solid-liquid interfaces at the TAS8 spectrometer at Risø. *Neutron News*, 7:25–31, 1996.

[42] A. Gibaud, G. Vignaud, and S.K. Sinha. The correction of geometrical factors in the analysis of x-ray reflectivity. *Acta Cryst.*, A49:642–648, 1993.

[43] O. Glatter and O. Kratky. *Small angle X-ray scattering.* Academic Press, 1982.

[44] O. Glatter, G. Scherf, K. Schillén, and W. Brown. Characterization of a poly(ethylene oxide)-poly(propylene oxide) triblock copolymer (EO_{27}-PO_{39}-EO_{27}) in aqueous solution. *Macromolecules*, 27:6046, 1994.

[45] R.D. Groot, N.M. Faber, and J.P. Van der Eerden. Hard sphere fluids near a hard wall and a hard cylinder. *Molecular Physics*, 62(4):861–874, 1987.

[46] A. Guinier and G. Fournet. *Small-angle scattering of X-rays.* John Wiley & Sons, 1955.

[47] W.A. Hamilton, P.D. Butler, S.M. Baker, G.S. Smith, J.B. Hayter, L.J. Magid, and R. Pynn. Shear induced hexagonal ordering observed in an ionic viscoelastic fluid past a surface. *Phys. Rev. Lett.*, 72(14):2219–2222, 1994.

[48] W.A. Hamilton, P.D. Butler, J.B. Hayter, L.J. Magid, and P.J. Kreke. "over the horizon" SANS: Measurements on near-surface Poiseuille shear-induced ordering of dilute solutions of threadlike micelles. *Physica B*, 221:309–319, 1996.

[49] I.W. Hamley and J.S. Pedersen. Analysis of neutron and x-ray reflectivity data. I. Theory. *J. Appl. Cryst.*, 27:29–35, 1994.

[50] B. Hammouda. Structure factor for starburst dendrimers. *J. Polym. Sci.: Part B: Polym. Phys.*, 30:1387–1390, 1992.

[51] J.P. Hansen and J.R. McDonald. *Theory of Simple Liquids.* Academic Press, 2nd edition, 1986.

[52] C.A. Helm, P. Tippman-Krayer, H. Möhwald, J. Als-Nielsen, and K. Kjær. Phases of phosphatidyl ethanolamine monolayers studied by synchrotron x-ray scattering. *Biophys. J.*, 60:1457–1476, 1991.

[53] C.R. Helms and E.H. Poindexter. The silicon-silicon-dioxide system: Its microstructure and imperfections. *Rep. Prog. Phys.*, 57:791–852, 1994.

[54] J.R. Henderson and F. Van Swol. On the interface between a fluid and a planar wall. theory and simulations of a hard sphere fluid at a hard wall. *Mol. Phys.*, 51(4):991–1010, 1984.

[55] R.J. Hunter. *Foundations of colloid science*, volume I. Oxford Science Publications, 1993.

[56] R.K. Iler. *The colloid chemistry of silica and silicates.* Cornell University Press, Ithaca, New York, 1955.

[57] R.K. Iler. *The chemistry of silica: Solubility, polymerization, colloid and surface properties, and biochemistry.* John Wiley & Sons, 1979.

[58] B. Jacrot. The study of biological structures by neutron scattering from solution. *Rep. Prog. Phys.*, 39:911–953, 1976.

[59] B. Jérôme. Surface effects and anchoring in liquid crystals. *Rep. Prog. Phys.*, 54:391–451, 1991.

[60] G. Karlström. A new model for upper and lower critical solution temperatures in poly(ethylene oxide) solutions. *J. Phys. Chem.*, 89:4962–4964, 1985.

[61] H. Kasten and G. Strobl. Nematic wetting at the free surface of 4-cyano-4'-*n*-alkyl-biphenyls. *J. Chem. Phys.*, 103(15):6768–6774, 1995.

[62] M.S. Kent, L.T. Lee, B.J. Factor, F. Rondelez, and G.S. Smith. Tethered chains in good solvent conditions: An experimental study involving Langmuir diblock copolymers monolayers. *J. Chem. Phys.*, 103(6):2320–2342, 1995.

[63] E. Killmann, H. Maier, and J.A. Baker. Hydrodynamic layer thicknesses of various absorbed polymers on precipitated silica and polystyrene latex. *Colloids Surf.*, 31:51–71, 1988.

[64] D.J. Kinning and E.L. Thomas. Hard-sphere interactions between spherical domains in diblock copolymers. *Macromolecules*, 17:1712–1718, 1984.

[65] T.L. Kuhl, D.E. Leckband, D.D. Lasic, and J.N. Israelachvili. *Stealth Liposomes*, chapter Modulation and modeling of interaction forces between lipid bilayers exposing terminally grafted polymer chains, pages 73–91. CRC Press, 1995.

[66] P.-Y. Lai and Kurt Binder. Structure and dynamics of grafted polymer layers: A Monte Carlo simulation. *J. Chem. Phys.*, 95(12):9288–9299, 1991.

[67] M.J. Lawrence. Surfactant systems: Their use in drug delivery. *Chem. Soc. Rev.*, pages 417–424, 1994.

[68] D.D. Lee, S.H. Chen, C.F. Majkrzak, and S.K. Satija. Bulk and surface corelations in a microemulsion. *Phys. Rev. E*, 52(1):R29–R32, 1995.

[69] D.D. Lee, B.R. McClain, B.L. Carvalho, S.G.J. Mochrie, J.D. Litster, S.H. Chen, C.F. Majkrzak, and S.K. Satija. Interfacial scattering form surfactant monolayers in microemulsions. *Physica B*, 221:296–300, 1996.

[70] J. Lee, A. Martic, and J.S. Tan. Protein adsorption on polyronic copolymer-coated polystyrene particles. *Journal of Colloid and Interface Science*, 131(1):252–266, 1989.

[71] J. Lekner. *Theory of reflection of electromagnetic and particle waves.* Developments in electromagnetic theory and applications. Martinus Nijhoff Publishers, 1987.

[72] E.K. Lin and A.P. Gast. Self consistent field calculations of interactions between chains tethered to spherical interfaces. *Macromolecules*, 29:390–397, 1996.

[73] P. Linse. Phase behaviour of poly(ethylene oxide)-poly(propylene oxide) block copolymers in aqueous solution. *J. Phys. Chem.*, 97:13896–13902, 1993.

[74] P. Linse. Adsorption and phase behaviour of Pluronic block copolymers in aqueous solution. *Colloids and Surf. A*, 86:137–142, 1994.

[75] P. Linse and M. Malmsten. Temperature-dependent micellization in aqueous block copolymer solutions. *Macromolecules*, 25:5434–5439, 1992.

[76] J.R. Lu, E.M. Lee, and R.K. Thomas. The analysis and interpretation of neutron and x-ray specular reflection. *Acta Cryst.*, A52:11–41, 1996.

[77] J.R. Lu, E.A. Simister, R.K. Thomas, and J. Penfold. Structure of the surface of a surfactant solution above the critical micelle concentration. *J. Chem. Phys.*, 97:13907–13913, 1993.

[78] O.M. Magnussen, B.M. Ocko, M.J. Regan, K. Penanen, P.S. Pershan, and M. Deutsch. X-ray reflectivity measurements of surface layering in liquid mercury. *Phys. Rev. Lett.*, 74(22):4444–4447, 1995.

[79] M. Malmsteen, P. Linse, and T. Cosgrove. Adsorption of PEO-PPO-PEO block copolymers at silica. *Macromolecules*, 25:2474–2481, 1992.

[80] S. Manne and H.E. Gaub. Molecular organization of surfactants at solid-liquid interfaces. *Science*, 270:1480–1482, 1995.

[81] A. Matsuyama and T. Kato. Theory of surface ordering of solutions of rigid rod-like molecules. *Macromolecules*, 28:131–135, 1995.

[82] A. Matsuyama, K. Umemoto, and T. Kato. Adsorption-induced surface ordering on solutions of rigid-rodlike molecules. *J. Chem. Phys.*, 105(4):1594–1600, 1996.

[83] G.A. McConnell, E.K. Lin, A.P. Gast, J.S. Huang, M.Y. Lin, and S.D. Smith. Structure and interactions in tethered-chain systems. *Faraday Discuss.*, 98:121–138, 1994.

[84] G.A. McConnell, M.Y. Lin, and A.P. Gast. Long range order in polymeric micelles under steady shear. *Macromolecules*, 28:6754–6764, 1995.

[85] D.C. McDermott, J.R. Lu, E.M. Lee, and R.K. Thomas. Study of the adsorption from aqeuous solution of hexaethylene glycol monododecyl ether on silica substrates using the technique of neutron reflection. *Langmuir*, 8:1204–1210, 1992.

[86] S.T. Milner, T.A. Witten, and M.E. Cates. Theory of the grafted polymer brush. *Macromolecules*, 21:2610–2629, 1988.

[87] P.J. Missel, N.A. Mazer, G.B. Benedek, C.Y. Young, and M.C. Carey. Thermodynamic analysis of the growth of sodium dodecyl sulfate micelles. *J. Phys. Chem.*, 84:1044, 1980.

[88] K. Mortensen. Phase behaviour of poly(ethylene oxide)-poly(propylene oxide)-poly(ethylene oxide) triblock-copolymer dissolved in water. *Europhys. Lett.*, 19(7):559–604, 1992.

[89] K. Mortensen. Structural studies of aqueous solutions of peo-ppo-peo triblock copolymers, their micellar aggregates and mesophases; a small-angle neutron scattering study. *J. Phys.: Condensed Matter*, 8:A103–A124, 1996.

[90] K. Mortensen, K. Almdal, F.S. Bates, K. Koppi, M. Tirrell, and B. Nordén. Shear devices for in situ structural studies of block-copolymer melts and solutions. *Physica B*, 213& 214:682–684, 1995.

[91] K. Mortensen and W. Brown. Poly(ethylene oxide)-poly(propylene oxide)-poly(ethylene oxide) triblock copolymers in aqueuos solution. the influence of relative block size. *Macromolecules*, 26:4128, 1993.

[92] K. Mortensen, W. Brown, and B. Nordén. Inverse melting transition and evidence of three-dimensional cubatic structure in block-copolymer micellar system. *Phys. Rev. Lett.*, 68:2340, 1992.

[93] K. Mortensen, W. Brown, and E. Jørgensen. Lamellar mesophase of poly(ethylene oxide)-poly(propylene oxide) melts and water-swollen mixtures. *Macromolecules*, 28:1458–1463, 1995.

[94] K. Mortensen and J.S. Pedersen. Structural study of the micelle formation of poly(ethylene oxide)-poly(propylene oxide)-poly(ethylene oxide) triblock copolymer in aqueous solution. *Macromolecules*, 26:805–812, 1993.

[95] K. Mortensen, D. Schwahn, and S. Janssen. Pressure-induced melting of micellar crystal. *Phys. Rev. Lett.*, 71(11):1728–1731, 1993.

[96] M.R. Munch and A.P. Gast. Block copolymers at interfaces. 1. micelle formation. *Macromolecules*, 21:1360–1366, 1988.

[97] M.R. Munch and A.P. Gast. Kinetics of block copolymer adsorption on dielectric surfaces from a selective solvent. *Macromolecules*, 23:2313–2320, 1990.

[98] M. Murat and G.S. Grest. Interaction between grafted polymeric brushes: A molecular-dynamics study. *Phys. Rev. Lett.*, 63(10):1074–1077, 1989.

[99] L. Névot and P. Croce. Charactérisation des surfaces par réflexion rasante de rayons x. Application a l'étude du polissage de quelques verres silicates. *Revue Phys. Appl.*, 15:761–779, 1980.

[100] J. Noolandi, A. Shi, and P. Linse. Theory of phase behaviour of poly(oxyethylene)-poly(oxypropylene)-poly(oxyethylene) triblock copolymers in aqueous solution. *Macromolecules*, 29:5907–5919, 1996.

[101] K. Okano. Anisotropic excluded volume effect and alignment of nematic liquid crystal in a sandwich cell. *Jpn. J. Appl. Phys.*, 22(6):L343–L344, 1983.

[102] L.G. Parratt. Surface studies of solids by total reflection of x-rays. *Phys. Rev.*, 95(2):359–369, 1954.

[103] J.S. Pedersen. Model-independent determination of the surface scattering-length-density profile from specular reflectivity data. *J. Appl. Cryst.*, 25:129–145, 1992.

[104] J.S. Pedersen. Instrumentation for small-angle scattering. In *Modern Aspects of small-angle scattering.* NATO Advanced Study Institute, May 12-22 1993.

[105] J.S. Pedersen and M.C. Gerstenberg. Scattering form factors of block copolymer micelles. *Macromolecules*, 29:1363–1365, 1996.

[106] J.S. Pedersen and I.W. Hamley. Analysis of neutron and x-ray reflectivity data. II. Constrained least-squares methods. *J. Appl. Cryst.*, 27:36–47, 1994.

[107] J.S. Pedersen, D. Posselt, and K. Mortensen. Analytical treatment of the resolution function for small-angle scattering. *J. Appl. Cryst.*, 23:321, 1990.

[108] J. Penfold and R.K. Thomas. The application of the specular reflection of neutrons to the study of surfaces and interfaces. *J. Phys.: Condens. Matter*, 2:1369–1412, 1990.

[109] J.K. Percus and G.J. Yevick. Analysis of classical statistical mechanics by means of collective coordinates. *Phys. Rev.*, 110:1, 1958.

[110] P.S. Pershan, A. Braslau, A.H. Weiss, and J. Als-Nielsen. Smectic layering a the free surface of liquid crystals in the nematic phase: X-ray reflectivity. *Phys. Rev. A*, 35(11):4800–4813, 1987.

[111] P. Pusey and W. van Megen. Phase behaviour of concentrated suspensions of nearly hard colloidal spheres. *Nature*, 320:340, 1986.

[112] K. Kjær, J. Als-Nielsen, C.A. Helm, L.A. Laxhuber, and H. Möhwald. Ordering in lipid monolayers studied by synchrotron x-ray diffraction and floures-cence microscopy. *Phys. Rev. Lett.*, 58(21):2224–2227, 1987.

[113] Lord Rayleigh. Diffraction of light by spheres of small refractive index. *Roy. Soc. London*, A90:219–225, 1914.

[114] M.J. Regan, P.S. Pershan, O.M. Magnussen, B.M. Ocko, M. Deutsch, and L.E. Berman. Capillary-wave roughening of surface-induced layering in liquid gallium. *Phys. Rev. B*, 54(14):9730–9733, 1996.

[115] E.B. Jørgensen, J.H. Jensen, and S. Hvidt. Gelation and micellation of aqueous solutions of a triblock copolymer. *J. Non-Cryst. Solids*, 172(2):972–977, 1994.

[116] R.M. Richardson, M.J. Swann, A.R. Hillman, and S.J. Roser. *In situ* neutron reflectivity studies of electroactive films. *Faraday Discuss.*, 94:295–306, 1992.

[117] W. Richtering, G. Schmidt, and P. Lindner. Small-angle neutron scattering from a hexagonal phase under shear. *Colloid and Polym. Sci.*, 274(1):85–88, 1996.

[118] F.J. Rogers and D.A. Young. New, thermodynamically consistent, integral equation for simple fluids. *Phys. Rev. A*, 30:999, 1984.

[119] D.C. Roux, J.-F. Berret, G. Porte, and E. Peuvrel-Disdier. Shear-induced orientations and textures of nematic wormlike micelles. *Macromolecules*, 28:1681–1687, 1995.

[120] J. Rubio and J.A. Kitchener. The mechanism of adsorption of poly(ethylene oxide) flocculant on silica. *Coll. Inter. Sci.*, 57(1):132–142, 1976.

[121] T.P. Russell. X-ray and neutron reflectivity for the investigation of polymers. *Mat. Sci. Rep.*, 5:171–271, 1990.

[122] K. Schillén, W. Brown, and R.M. Johnsen. Micellar sphere-to-rod transition in an aqueous triblock copolymer system. A dynamic light scattering study of translational and rotational diffusion. *Macromolecules*, 27:4825–4832, 1994.

[123] D.K. Schwartz, A. Braslau, B. Ocko, P.S. Pershan, J. Als-Nielsen, and J.S. Huang. X-ray reflectivity of a microemulsion surface. *Phys. Rev. A*, 38(11):5817–5824, 1988.

[124] N. Singh, M. Tirrell, and F.S. Bates. Applications of Fourier-synthesis methods to the analysis of specular reflectivity. *J. Appl. Cryst.*, 26:650–659, 1993.

[125] D.S. Sivia, W.A. Hamilton, and G.S. Smith. Analysis of neutron reflectivity data: Maximum entropy, Bayesian spectral analysis and speckle holography. *Physica B*, 173:121–138, 1991.

[126] B. Smit, P.A.J. Hilbers, K. Esselink, L.A.M. Rupert, N.M. van Os, and A.G. Schlijper. Computer simulations of a water/oil interface in the presence of micelles. *Nature*, 348:624–625, 1990.

[127] I.K. Snook and D. Henderson. Monte Carlo study of a hard-sphere fluid near a hard wall. *J. Chem. Phys.*, 68(5):2134–2139, 1978.

[128] M. Stamm. Polymer interfaces on a molecular scale: Comparison of techniques and some examples. *Adv. Polym. Sci.*, 100:357–400, 1992.

[129] M.M. Stecker and G.B. Benedek. Theory of multicomponent micelles and microemulsions. *J. Phys. Chem.*, 88:6519, 1984.

[130] D.I. Svergun and J.S. Pedersen. Propagating errors in small-angle scattering treatment. *J. Appl. Cryst.*, 27:241–248, 1994.

[131] I. Szleifer and M.A. Carignano. Tethered polymer layers. *Adv. Chem. Phys.*, 94:165–260, 1996.

[132] C. Tanford. *The hydrophobic effect: Formation of micelles and biological membranes.* John Wiley & Sons, 2nd edition, 1980.

[133] R.K. Thomas. Scattering methods in polymer science. In R.W. Richards, editor, *Neutron reflection from polymer-bearing interfaces.* Ellis Horwood Ltd, 1995.

[134] F. Tiberg and A.-M. Cazabat. Spreading of thin films of ordered nonionic surfactants. Origin of the stepped shape of the spreading precursor. *Langmuir*, 10:2301–2306, 1994.

[135] F. Tiberg, M. Malmsten, P. Linse, and B. Lindman. Kinetic and equilibrium aspects of block copolymer adsorption. *Langmuir*, 7:2723–2730, 1991.

[136] R. Toral and A. Chakrabarti. Monte carlo study of polymer chains endgrafted onto a spherical interface. *Phys. Rev. E*, 47(6):4240–4246, 1993.

[137] G. Vigil, Z. Xu, S. Steinberg, and J. Israelachvili. Interactions of silica surfaces. *Coll. Inter. Sci.*, 165:367–385, 1994.

[138] G.J. Vroege and H.N.W. Lekkerkerker. Phase transitions in lyotropic colloidal and polymer liquid crystals. *Rep. Prog. Phys.*, 55:1241–1309, 1992.

[139] C.M. Wijmans and P. Linse. Surfactant self-assembly at a hydrophilic surface. a Monte Carlo simulation study. *J. Phys. Chem.*, 100:12583–12591, 1996.

[140] R.W.G. Wyckoff. *Crystal Structures*, volume 1. Interscience Publishers, John Wiley & Sons, 2nd edition, 1963.

[141] X.-L. Zhou, L.-T. Lee, S.-H. Chen, and R. Strey. Observation of surface-induced layering in bicontinuous microemulsions. *Phys. Rev. A*, 46(10), 1992.

Bibliographic Data Sheet **Risø–R–986(EN)**

Title and author(s)

A Neutron Scattering Study of Triblock Copolymer Micelles

Michael C. Gerstenberg

ISBN	ISSN
87–550–2306–1	0106–2840

Dept. or group	Date
Department of Condensed Matter Physics and Chemistry	November 1997

Groups own reg. number(s)	Project/contract No.

Pages	Tables	Illustrations	References
120			

Abstract (Max. 2000 char.)

This thesis describes the neutron scattering experiments performed on poly(ethylene oxide)/poly(propylene oxide)/poly(ethylene oxide) triblock copolymer micelles in aqueous solution. The studies concern the non-ionic triblock copolymer P85 which consists of two outer segments of 25 monomers of ethylene oxide attached to a central part of 40 monomers of propylene oxide. The amphiphilic character of P85 leads to formation of various aggregates in aqueous solution e.g. spherical and rod-like micelles.

The present investigations are centered around the micellar structures. In the first part of this thesis a model for the micelle is developed for which an analytical scattering form factor can be calculated. The micelle is modeled as a solid sphere with tethered Gaussian chains. Good agreement was found between small-angle neutron scattering experiments and the form factor of the spherical P85 micelles. The second part focuses on the surface-induced ordering of the various micellar structures of P85. In the spherical micellar phase, neutron reflection measurements indicated a micellar ordering at the hydrophilic surface of quartz. Extensive modeling was performed based on a hard sphere description of the micellar interaction. By convolution of the distribution of hard spheres at a hard wall, obtained from Monte Carlo simulations, and the projected scattering length density of the micelle, a numerical expression was obtained which made it possible to fit the data. The hard-sphere-hard-wall model gave an excellent agreement in the bulk micellar phase. However, free-form analysis hinted towards a precrystallization of the micelles at the surface at higher concentrations (25 wt % P85). For temperatures above 60°C a 5 wt % solution showed a high degree of surface association. The reflectivity experiments indicated that the surface ordering of the triblock copolymers changed from spherical micelles to a lamellar phase with increasing temperature. It was not possible to further increase the surface ordering by applying a shear field to the solution. In the bulk micellar cubic phase, the strong surface induced ordering could not be determined unambiguously.

Descriptors INIS/EDB

Available on request from:
Information Service Department, Risø National Laboratory
(Afdelingen for Informationsservice, Forskningscenter Risø)
P.O. Box 49, DK–4000 Roskilde, Denmark
Phone (+45) 46 77 46 77, ext. 4004/4005 · Fax (+45) 46 77 40 13

RISØ

Objective

Risø National Laboratory carries out research within science and technology, providing Danish society with new opportunities for technological development. The research aims at strengthening Danish industry and reducing the adverse impact on the environment of the industrial, energy and agricultural sectors.
Risø has a special responsibility for the consolidation of the knowledge base for consultancy on nuclear affairs.

Research profile

Risø performs long-term research of relevance to Danish society. This research is part of a range of Danish and international research programmes and similar collaborative ventures. Risø undertakes research, development and consultancy projects for the authorities and industry. The main emphasis is on basic research and participation in strategic collaborative research ventures. Research is carried out within the following programme areas:

Industrial materials
New functional materials
Optics and sensor systems
Plant production and ecology
Systems analysis
Wind energy and atmospheric processes
Nuclear safety

Risø-R-986(EN)
ISBN 87-550-2306-1
ISSN 0106-2840

Copies of this publication
are available from
Risø National Laboratory
Information Service Department
P.O. Box 49
DK-4000 Roskilde
Denmark
Telephone +45 4677 4004
e-mail: risoe@risoe.dk
Fax +45 4677 4013
http://www.risoe.dk

Product, target groups and collaboration

Risø's product is knowledge and technological development generated by high-quality research. The target groups are industry, the authorities and the research community. Risø collaborates with universities, research institutes, institutes of technology and businesses. A strong emphasis is placed on the education of young researchers through Ph.D. and post-doctoral programmes.

Key figures

Risø has 960 employees, including 360 researchers and 100 Ph.D. candidates and post-doctoral personnel. Risø's 1997 budget is DKK 485 m, of which DKK 223 m is income from programme research and contract work. The balance is funded by Government grant.